

Christian-Albrechts-Universität zu Kiel
Institut für Geowissenschaften, Abteilung Geophysik

Processing and interpretation of satellite and ground based gravity data at different lithospheric scales

Dissertation

zur Erlangung des akademischen Grades

Doktor der Naturwissenschaften (Dr. rer. nat.)

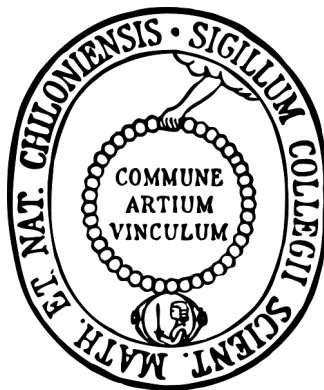
der Mathematisch-Naturwissenschaftlichen Fakultät der

Christian-Albrechts-Universität zu Kiel

vorgelegt von

Nils Holzrichter

Kiel, 2013



Referent: Prof. Dr. Hans-Jürgen Götze

Korreferent: Prof. Dr. Wolfgang Rabbel

Tag der Disputation: 16.08.2013

Zum Druck genehmigt: 16.08.2013

gez. Prof. Dr. Wolfgang J. Duschl, Dekan

Zusammenfassung

Die globale Verfügbarkeit von Schweredaten ermöglicht regionale Untersuchungen (Anomalien >100 km Wellenlänge) der Dichtestruktur der Lithosphäre. In dieser Dissertation werden Satellitenschweremodelle auf verschiedenen Skalen auf ihre Anwendbarkeit für dreidimensionale Dichtemodelle untersucht, sowie ein neues Verfahren zur topographischen Korrektur von Schweredaten präsentiert. Im ersten Teil dieser Arbeit werden die Bougueranomalien von verschiedenen Satellitenmissionen (GRACE und GOCE) in den Anden und Costa Rica mit terrestrischen Daten verglichen. Hierfür werden zuerst aus den globalen Satellitendaten zwei Bougueranomalien auf Basis verschiedener geodätischer Definitionen (die geodätische "klassische" Schwereanomalie und die geodätische Schwerestörung) analysiert und beschrieben. Hierbei zeigen sich große Unterschiede zu terrestrischen Daten in Regionen hoher Topographie. Die Vergleiche mit einem existierenden Dichtemodell in den Anden (zwischen 36°S und 42°S) zeigen, dass Satellitenmodelle geeignet sind um regionale Schwereeffekte an aktiven Kontinentalrands (z.B. abtauchende Platte, der Kruste und des Mantels) zu modellieren. Kleinere Strukturen, wie z.B. der vulkanische Rücken sind nicht sichtbar.

Der zweite Teil beschäftigt sich mit der Prozessierung von Schweredaten und stellt die Entwicklung eines Algorithmus für eine präzise topographische Korrektur mit Hilfe von Polyhedrons dar. Das neue Verfahren berücksichtigt, neben der genauen Repräsentation der topographischen Geometrie durch triangulierte Oberflächen, auch die Krümmung der Erde, berechnet Korrekturen für die Schweregradienten, verarbeitet sehr große topographische Datensätze und dünnt effektiv redundante Informationen in den topographischen Datensätzen aus, um die Rechenzeit zu verkürzen; dabei wird weit entfernte Topographie berücksichtigt. Mit diesen Funktionen erfüllt das Verfahren alle Voraussetzungen, um topographische Korrekturen auch für große regionale Datensätze durchzuführen. Zum Ausdünnen topographischer Informationen wird eine Datenstruktur auf Grundlage eines "Quad-tree" angelegt, der topographische Daten in verschiedenen (immer größer werdenden) Auflösungen enthält. Während der Berechnung des topographischen Schwereeffekts wird eine feine Auflösung automatisch nur dann gewählt, wenn es einen signifikanten Einfluss auf den Schwerewert an der Station hat. Im Unterschied zu bestehenden Methoden zum Vergrößern der topographischen Information bezieht dieser neue Ansatz erstmalig nicht nur den Abstand der topographischen Struktur zur Station in die Berechnung ein, sondern auch deren Geometrie. Dies führt zu einem sehr effektiven Ausdünnen von Höhenpunkten und einer besseren Repräsentation weit entfernter Topographie, ohne jedoch den Einfluss eines Höhenzuges auf den Stationsschwerewert signifikant zu verändern. Das neue Verfahren wird mit synthetischen Stationsdaten in Zentralasien nahe des Himalayas mit bestehenden Algorithmen verglichen. Zudem wird durch Vergleiche der Einfluss verschiedener Auflösungen der Gitternetze auf die Korrekturen abgeschätzt. Die Ergebnisse zeigen, dass Korrekturen mit einer geringeren Auflösung der Topographie (z.B. 1 km) zu einem deutlichen Unterschied zu Berechnungen mit hoher Auflösung (90 m) führen ($\sim 10 * 10^{-5} \frac{m}{s^2}$ Standardabweichung).

II

Vergleiche zwischen topographischen Korrekturen des neuen Algorithmus und bestehender Bougueranomalien in den Anden zeigen leichte Abweichungen. Die topographische Korrektur von Schweregradienten wird erfolgreich in den Anden durchgeführt und zeigt, dass die Korrektur zu einer besseren Abbildung von Untergrundstrukturen durch die gemessenen Gradienten führt. Ein weiterer Test wird am passiven Kontinentalrand Westaustraliens durchgeführt, um den Unterschied topographischer Korrekturen in kleinräumigeren flachen Gebieten zu untersuchen. Im nördlichen Perth-Becken werden existierende Bougueranomalien mit Berechnungen der Bougueranomalie durch das neue topographische Korrekturverfahren verglichen. Hierbei zeigt sich eine bessere Korrelation der Neuberechneten Schwereanomalie mit geologischen Strukturen. Im selben Gebiet wird ein dreidimensionales Schweremodell basierend auf terrestrischen Daten erstellt, um die Entstehung und Tiefe der Sedimentbecken und den isostatischen Zustand zu untersuchen. Diese Ergebnisse werden im Anschluss mit Satellitendaten verglichen, um das verschiedene Auflösungsvermögen der beiden Schwerefelder in dieser Region zu vergleichen. Es kann gezeigt werden, dass die Schwerefelder auch hier nutzbar sind, um die Geometrie der Krusten-Mantel Grenze zu beschreiben. Sedimentbecken sind hier nicht bzw. nur leicht im Satellitenschwerefeld zu sehen. Diese Ergebnisse decken sich mit den Untersuchungen am aktiven Kontinentalrand.

Abstract

Global availability of gravity data allows the regional investigation (<100 km anomaly wavelengths) of the lithosphere. This thesis describes the processing and use of satellite gravity data for modelling at different lithospheric scales. The first part shows comparisons of satellite gravity from different missions (GRACE and GOCE) and ground based data in the Andean mountain range and Costa Rica. First, the terrain corrected Bouguer anomaly were compiled from two geodetic definitions: the geodetic "classical" gravity anomaly and the geodetic gravity disturbance. Large deviations from ground data are observed in areas of high topography. Second, comparisons with an existing density model at the Andes (between 36°S and 42°S) prove, that satellite gravity can be used to model regional gravity effects (e.g. subducting slab, crust and mantle). The volcanic back arc do not show up in the satellite gravity data.

The second part of the thesis presents the development of a new accurate algorithm for topographic correction based on a polyhedral representation by triangulation of topographic surfaces. The new algorithm also considers sphericity of the earth, calculates gravity gradients, deals with large datasets and uses an adaptive approach for resampling topography to save computation time. The resampling algorithm bases on a quad tree representation of the topography grid with different resolutions. High resolutions of the topography grid are only considered if it has a significant influence on the gravity at the station. Thus, this approach links the resampling of topography during the calculation with distance and geometry of topography. This leads to an accurate representation of distant terrain and a massive speed up of computation time. The new algorithm will be tested in an area of central Asia in the Himalayan mountain range and compared to existing algorithms. Furthermore, the impact of grid resolutions on the correction will be discussed. Results show significant differences between corrections for different resolutions (e.g. $10 * 10^{-5} \frac{m}{s^2}$ root mean square error between 1 km and 90 m grid resolution). Recalculations of existing Bouguer anomaly compilations show slight differences. Topographic correction of gradients are calculated in the Andes which leads to an improved representation of lithospheric structures in the measured gradients. Another test is conducted at a passive continental margin to investigate the effect of topographic corrections in another environment. Bouguer anomalies of the North Perth basin are recalculated which improves the fit of anomalies and geological structural elements. A 3D model is set up based on ground data to investigate the sedimentary basins at the isostatic state of the area. The results will be compared to satellite data to estimate the usability of satellite data in such an environment. The comparison shows that satellite data can be used to calculate the Moho interface in this area. However, small structures like sedimentary basins do not show up in the gravity field. The results are in agreement with the investigations in the area of an active continental margin (Central Andes).

Table of Contents

1	Introduction	1
1.1	Methods	3
2	The seismically active Andean and Central American margins: Can satellite gravity map lithospheric structures?.....	4
2.1	Introduction.....	4
2.2	Tectonic setting	6
2.3	Gravity database and geophysical constraints.....	8
2.4	Results and discussions	9
2.4.1	Geophysical and Geodetic Bouguer anomaly	9
2.4.2	Data quality of the EGM2008.....	10
2.4.3	Spatial resolution of different satellite gravity models	16
2.4.4	Asperity mapping and resolution of gravity gradient data.....	17
2.5	Geodynamic model of the Andean margin as constrained by satellite gravity data.....	21
2.6	Conclusions.....	23
3	Topographic correction of gravity (gradient) data	24
3.1	Historical development of topographic correction and state of the art	25
3.1.1	Terrain and Bouguer correction and complete mass correction.....	32
3.1.2	Distant topography and limiting radius	33
3.2	New approach for consistent topographic correction.....	33
3.2.1	Triangulation of data.....	38
3.2.2	Availability of Topography	41
3.2.3	Adaptive resampling of topography	42
3.2.4	TriTop	47
3.3	Test bed "Himalaya": Comparison of Algorithms and DTMs	48
3.3.1	Differences between algorithms.....	49
3.3.2	Benchmark for different resolutions	50
3.4	Test bed Himalaya: Effect of distant topography	54
3.5	Correction of Andean gravity data	57
3.6	Gradient correction of satellite data.....	61

3.7	Final conclusions for topographic correction.....	63
4	Crustal structure of the northern Perth Basin, southwest margin of Australia: insights from three-dimensional density models.....	66
4.1	Introduction.....	68
4.2	Constraining Data	70
4.2.1	Bathymetry and Topography	70
4.2.2	Gravity Data	70
4.2.3	Seismic Interpretation of Sediment Thickness	72
4.2.4	Densities.....	74
4.2.5	Crustal Thickness.....	75
4.3	Modelling strategy	77
4.4	Results	77
4.4.1	Model 1: Moho defined by local isostasy	79
4.4.2	Model 2: MoGGIE Moho	81
4.4.3	Adjusted MoGGIE model.....	83
4.4.4	Inversion for flexural rigidity.....	85
4.5	Discussion	87
4.5.1	Dandaragan Trough	87
4.5.2	Beagle Ridge and Abrolhos Sub-basin	88
4.5.3	Turtle Dove Ridge.....	88
4.5.4	Zeewyck Sub-basin.....	89
4.6	Conclusions and outlook	90
4.7	Applicability of satellite data at a passive continental margin	90
5	Conclusion and Outlook.....	94
5.1	Conclusion	94
5.2	Outlook.....	97
	References	92
	Danksagung	92

1 Introduction

This dissertation was written in the framework of the projects NOGAPSGRAV and IMOSAGA which are associated with the special priority program (SPP) 1257 funded by the German research foundation (DFG). The SPP 1257 is called "mass transport and mass distribution of the earth system". The program consisted of more than twenty projects mainly focusing on the processing of satellite gravity data from GRACE and the analysis of mass transport of water and convection in the upper mantle. The project NOGAPSGRAV dealt with the application of global satellite gravity models (GEM) like EIGEN-5C/S and EGM2008 for modelling of the lithosphere. Chapter 2 of this dissertation is a scientific paper (Köther *et al.*, 2012) originally published in the Journal of Geodynamics¹ which concludes the results of the NOGAPSGRAV project. My work focussed on the calculations and discussion of different definitions of gravity anomalies introduced by geodesists and geophysicists. There, I pointed out that the geodetic gravity disturbance is identical to the geophysical definition of the free air anomaly and should be used for geophysical applications. The second definition of gravity, the geodetic gravity anomaly is defined on the geoid (in most publications) and do not coincide with geophysical datasets. I analysed the data quality of both anomaly types of the EGM 2008 in the Andes by comparing it to the terrestrial database provided by the SFB 267 and datasets of Costa Rica provided by Lücke (2012)². The comparison showed that the disturbance correlates better to the terrestrial data, especially in areas of high topography. The results in the Costa Rican area showed, that the EGM 2008 comprises large errors in mountainous areas and the geodetic gravity anomaly is worse than the geodetic gravity disturbance. Finally, I compared the applicability of satellite models from GRACE, GOCE, EGM2008 and EIGEN for the modelling of the lithosphere in the Andean region. For this purpose, I choose the 3D gravity model set up by Alasonati-Tašárová (2007) and compared the calculated and measured gravity data with the fields provided by the satellite models. It could be concluded that satellite only models are applicable to model the long wavelength (~ 100-150 km) of the Andean subduction zone. Smaller anomalies are not visible in the satellite data, but show up in the combined gravity models. The satellite models provide new insights in inaccessible areas and for global or regional studies. However, the combined models show errors and large deviations in areas of high topography. Therefore, chapter 3 deals with topographic reduction of gravity (gradient) data. First, an overview about existing methods and the historical development of topographic and Bouguer reduction is shown. Old algorithms use pre-assumptions like a fixed correction radius and approximations of geometry like prisms to keep computational costs low.

¹Köther, N., Götze, H.J., Gutknecht, B.D., Jahr, T., Jentsch, G., Lücke, O.H., Mahatsente, R., Sharma, R. & Zeumann, S., 2012. The seismically active Andean and Central American margins: Can satellite gravity map lithospheric structures?, Journal of Geodynamics, 59–60, 207-218.

² Lücke, O.H., 2012. 3D Density Model of the Central American Isthmus from satellite derived gravity data, Ph.D. thesis, Christian-Albrechts-Universität zu Kiel, Kiel.

The availability of global gravity (gradient) data asks for an algorithm, which is able to handle corrections for large datasets in acceptable time, account for sphericity and calculate topographic corrections for gravity gradients. Therefore, a new concept for the correction of the whole topographic mass was developed. It bases on triangulated polyhedral bodies to represent topography. The calculation was realised with the approach published by Götze and Lahmeyer (1988). It is capable to calculate all components of gravity and the gravity gradients, respectively. Furthermore, it was modified to account for sphericity of the earth. In the new concept, the correction area was extended to a global scale which means that topographic correction is calculated up to the entire globe and not for a restricted area (e.g. 167 km; (Ehrismann, 1972) . The new method chooses a certain resolution of topography which depends on the magnitude of gravity on the station. Thus, even large scale studies can be reduced with high resolution topography grids in an acceptable computation time. There is no need for the user to decide which resolution is appropriate; the algorithm takes over the decision. Different scenarios for topographic corrections were conducted by synthetic stations in the Central Asian region (at the Himalayan mountain range and the Tibetan plateau). The new approach were compared with older algorithms. Furthermore, the influence of topographic grid spacing on the amount of corrections were evaluated. These test calculations made clear that mass corrections change significantly if a different grid spacing is used. In particular, stations located in rugged terrain are more affected by the grid spacing than stations in flat terrain. However, it is shown that the choice of an appropriate grid spacing is complicated. Corrections performed with the adaptive resampling are similar to calculations without any resampling but much faster (e.g. by a factor 100-300). Furthermore, a recalculation of topographic correction of the gravity data used for the 3D density model of Alasonati-Tašárová (2007) is shown and compared with old algorithms. Results are quite similar but differences arise from the use of different topographic grids. Finally, corrections on satellite gravity gradients are introduced. They show that topography reveals lithospheric structures in the gradient components.

The first chapters of this thesis deal with large scale modelling and data issues at active continental margins with high topography. Chapter 4 describes investigations at the smaller scale of a passive continental margin (West Australia) with rather flat topography. The results are compared to chapter 2.4.3 to show different needs for gravity modelling and the use of satellite data in different environments. The corresponding publication with me as a first author was submitted to the "Geophysical Journal International"³. It was conducted in collaboration with Geoscience Australia to assess the hydrocarbon potential of sedimentary basins in the North Perth basin. This time, my work concentrated on the collection of all relevant geometric information and parameter data, the 3D density modelling itself and an integrated interpretation and discussion of the results. The main focus of my research was put on the determination of the depths of these sedimentary basins and the isostatic state of the area. It could be shown, that depocentres in this area are not governed by local (Airy-Pratt) isostasy and the depth of the sediments is

³ Holzrichter, N., Hackney, R.I., Johnston, S., 2013. Crustal structure of the northern Perth Basin, southwest margin of Australia: insights from three-dimensional density models, *Geophysical Journal International*, doi: 10.1093/gji/ggt347.

underestimated by seismic imaging methods. Furthermore, not all Sub-basins developed by crustal thinning but also by crustal faulting. The discussion of the isostatic state indentified areas of weak (Zeewyck Sub-basin) crust and rigid (Dandaragan trough) crust which can be explained by different fault geometries in a huge area of this passive continental margin. Finally, a comparison of satellite and terrestrial data became possible on the basis of the final 3D density models. The comparison shows that application of satellite only gravity models helps to model the crust mantle boundary but is not able to image small scale structures, e.g. sedimentary basins. This is in agreement with the findings of chapter 2.4.3 at the active continental margin. A final summary which describes the applicability of satellite and terrestrial gravity data for the purpose of lithospheric modelling and the discussion of the impact of topographic corrections on the final gravity data concludes the thesis.

1.1 Methods

Chapter 2.4.3 and 4 focus on the 3D density modelling of lithospheric structures. For this purpose, the software package IGMAS+ (<http://www.potentialgs.com>) was used (Götze *et al.*, 2007, Schmidt *et al.*, 2007). It bases on the results by Götze (1976) and Götze and Lahmeyer (1988). Besides a fast and effective calculation of gravity polyhedral bodies by a closed formula, it offers 3D visualisation and an interactive modification of parameters like density and geometry. For comparison of data, GMT (Generic Mapping Tools) (Wessel and Smith, 1991, Wessel and Smith, 1998) and bash scripts were used. The processing of data was conducted with self written scripts, ArcGIS (<http://esri.de/products/arcgis>) and Intrepid Software (<http://www.intrepid-geophysics.com>). The code of topographic correction program was written in Java. Other tools are explained in detail in the corresponding chapters.

Remark:

All calculations are performed on a Inter Core i7-2600 (3.4GHz, 8MB) with 16GB of RAM. All algorithms use only one core for calculation. The gravitational constant G is set to $6.67428 \cdot 10^{-11} \frac{m^3}{kg \cdot s^2}$ and the earth radius R is set to 6378137 m.

2 The seismically active Andean and Central American margins: Can satellite gravity map lithospheric structures?

The spatial resolution and quality of geopotential models (EGM2008, EIGEN-5C, ITG-GRACE03s, and GOCO-01s) have been assessed as applied to lithospheric structure of the Andean and Central American subduction zones. For the validation, we compared the geopotential models with existing terrestrial gravity data and density models as constrained by seismic and geological data. The quality and resolution of the downward continued geopotential models in the Andes and Central America decrease with increasing topography and depend on the availability of terrestrial gravity data. High resolution of downward continued gravity data has been obtained over the Southern Andes where elevations are lower than 3000 m and sufficient terrestrial gravity data are available. The resolution decreases with an increase in elevation over the north Chilean Andes and Central America. The low resolution in Central America is mainly attributed to limited surface gravity data coverage of the region.

To determine the minimum spatial dimension of a causative body that could be resolved using gravity gradient data, a synthetic gravity gradient response of a spherical anomalous mass has been computed at GOCE orbit height (254.9 km). It is shown that the minimum diameter of such a structure with density contrast of 240 kg m^{-3} should be at least $\sim 45 \text{ km}$ to generate signal detectable at orbit height. The batholithic structure in Northern Chile, which is assumed to be associated with plate coupling and asperity generation, is about 60-120 km wide and could be traceable in GOCE data. Short wavelength anomalous structures are more pronounced in the components of the gravity gradient tensor and invariants than in the gravity field.

As the ultimate objective of this study is to understand the state of stress along plate interface, the geometry of the density model, as constrained by combined gravity models and seismic data, has been used to develop dynamic model of the Andean margin. The results show that the stress regime in the fore-arc (high and low) tends to follow the trend of the earthquake distributions.

2.1 Introduction

Novel satellite gravity missions aim at a breakthrough in recovering signals associated with mass transport, mass distribution and the underlying dynamic processes on the Earth's surface, the lithosphere and upper mantle. The missions significantly improved the coverage and availability of gravity data. In the year 2000, CHAMP started to measure the global gravity field with a spatial resolution of about 550 km (e.g. Eigen-2, (Reigber *et al.*, 2005)). The following GRACE mission measured gravity with an increased spatial resolution of approximately 140 km (ITG-GRACE03s, (Mayer-Guerr, 2007)). In 2009, the GOCE mission has begun measuring the gradients of the gravity field. Compared to scalar measurements, gradiometry offers better signal to noise ratio, de-emphasises regional trends (Holstein *et al.*, 2007) and provides enhanced sensitivity of geological structures (e.g. (Pedersen and Rasmussen, 1990, Fedi *et al.*, 2005)). Thus, the direct use

of gradients is a new scope for geophysical modelling. However, it has to be determined whether the resolution of downward continued GOCE gradient data is sufficient for direct application to lithospheric studies. One recent high-resolution gravity model of GOCE is GOCO-01s which is a combined model of GRACE solutions for lower degrees and GOCE data for higher degrees (Pail *et al.*, 2010). Higher resolution is provided by combined models of terrestrial and satellite data. The EIGEN-5C (Foerste *et al.*, 2008) and the EGM2008 (Pavlis *et al.*, 2008) provide gravity data with spatial resolution of 56 km and 10 km, respectively.

In this paper, we investigate the resolution and quality of various geopotential models as applied to lithospheric structures and mapping of regions of high seismic moment release (asperities) using the active plate boundaries of Central America and Southern Central Chile as case studies. The origin and role of asperities in earthquake recurrence in these regions are much debated (e.g. Wells *et al.*, 2003). Many source time functions of large earthquakes show distinct onsets of sub-events and episodes of moment release, which signify co-seismic failure of asperities. As causes for these sub-events, varying physical properties such as geometrical and/or material heterogeneities and dynamically generated complexities are suggested (Madariaga and Cochard, 1996, Aochi *et al.*, 2003, Marsan, 2006). Inhomogeneities on the subducting plate (e.g. seamounts, ridges, transform faults) could lead to stronger coupling (Kirby *et al.*, 1996, Cloos, 1992, Barckhausen *et al.*, 1998, DeShon *et al.*, 2003). Deep-sea terraces and sedimentary basins along convergent margins are other proposed indicators of asperities (Song and Simons, 2003, Wells *et al.*, 2003, Fuller *et al.*, 2006).

In regions of high seismic moment release, trench-parallel gravity anomalies positively correlate with topography. Thus, the spatial gravity variations over the fore-arc could serve as proxy for the long-term state of stress on the plate interface (Song and Simons, 2003). Furthermore, (Wells *et al.*, 2003) showed that epicentres of major earthquakes often tend to concentrate on the pronounced gravity gradients from the fore-arc basins towards gravity highs. Recent studies in the South-Central Chile suggest that pressure exerted by batholithic structure and buoyancy force acting on the Nazca plate could be one of the possible mechanisms of asperity generation (Sobiesiak *et al.*, 2007). An analysis of the 1995 Antofagasta earthquake showed that high b-values correlate with isostatic residual gravity anomalies of the region (Sobiesiak *et al.*, 2007). The isostatic residual anomalies are caused by batholithic bodies of the Jurassic to early Cretaceous magmatic arc system and help to lock the interface of the seismogenic zone. This is also indicated in the local tomography as high P-wave velocity (Husen, 1999). Tassara (2010) expanded this hypothesis for the entire Chilean-Pacific margin and suggested that hazardous earthquakes predominantly occur in regions of positive vertical stress anomalies associated with positive density anomalies of the crust in the fore-arc region.

The scope of this work is to test the resolution of satellite-only and combined models as applied to lithospheric structure, tectonic processes and dynamic evolution of convergent plate boundaries. In order to test the resolution and unravel the 3D structure as well as the dynamic evolution of the two convergent plate margins, three steps have been followed: (1) all terrestrial gravity data from the region of interest have been combined into a single database; (2) satellite-derived gravity data have been used to fill in regions lacking terrestrial gravity coverage; and (3) the combined gravity

database has been used to develop 3D lithospheric structures of the two convergent plate margins. Then, the geometry and physical parameters obtained from the well-constrained 3D density models have been used to refine the dynamic models of the Andean margin. The satellite gravity data have been obtained from the ICGEM portal of the GFZ Potsdam (<http://icgem.gfz-potsdam.de/ICGEM/>).

2.2 Tectonic setting

The Andes mountain belt is the result of subduction of the Nazca beneath South America plate. The dynamics of subduction are mainly controlled by the convergence rate and age of the subducting plate. Several studies indicate the differences in tectonic style between the Central and Southern Andes (e.g. (Allmendinger *et al.*, 1997, Ramos and Aleman, 2000). The Central Andes can be divided from west to east into the fore-arc, magmatic arc and backarc (Reutter and Götze, 1994). The fore-arc comprises the Coastal Cordillera, the Longitudinal Valley, the Precordillera and the Preandean depression (Figure 2-1). Since the Jurassic, the magmatic arc front has migrated more than 200 km to the east (e.g. (Scheuber *et al.*, 1994), with the Jurassic arc now present along the Coastal Cordillera and on the slope of the fore-arc (about 50 to 150 km east of the trench). Repeated micro-gravity and GPS measurements reveal the on-going deformation and relaxation processes after the 1960 Valdivia earthquake (Klotz *et al.*, 2001). The main causes for these tectonic differences are changes in slab dip, age and convergence obliquity (e.g. (Gutscher *et al.*, 2000). Young and buoyant slabs produce shallow dips and strong seismic coupling. Convergence was always oblique, with obliquity changing with time and latitude. Convergence velocity also fluctuated considerably and has been decreasing throughout the Neogene (Norabuena *et al.*, 1999). However, it was always amongst the faster convergence rates observed on Earth.

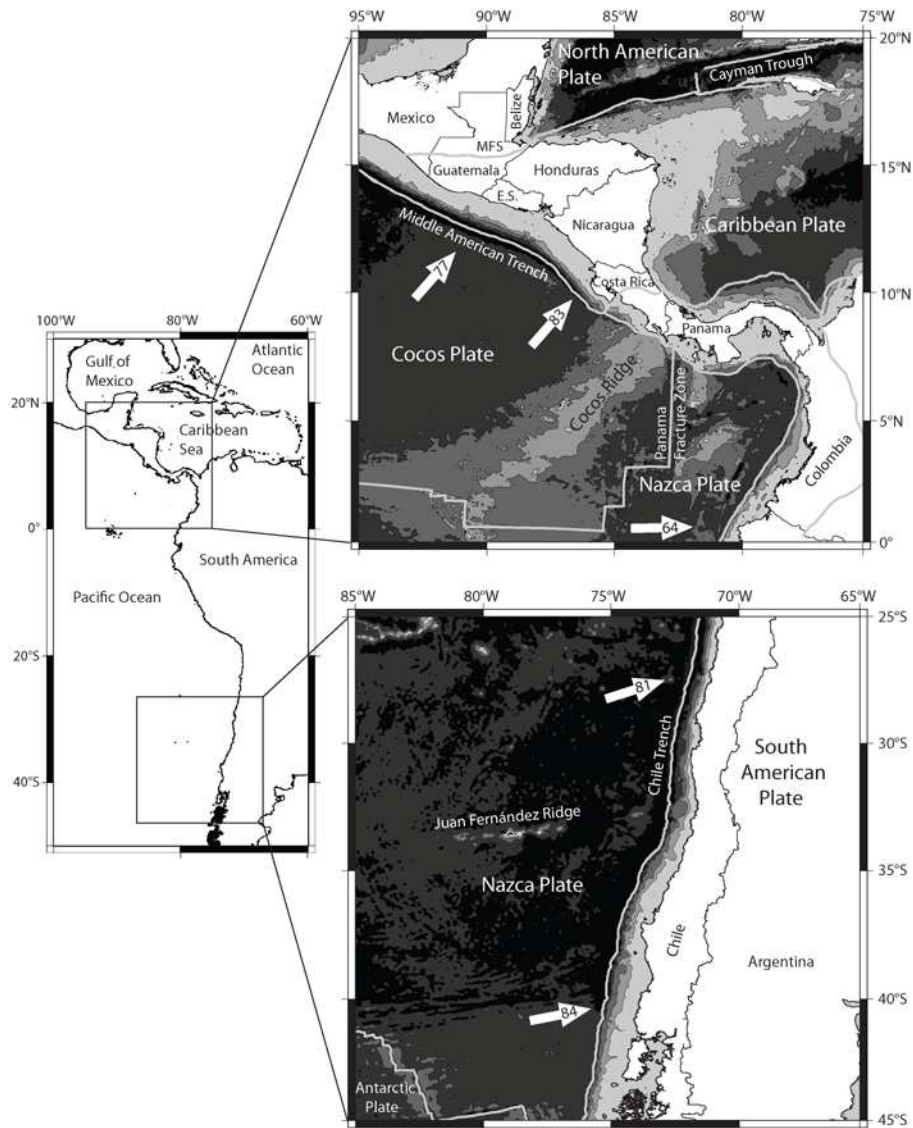


Figure 2-1: Geologic setting of Central (top) and South (bottom) America. The white arrows show the plate movement per year in mm (DeMets *et al.*, 1994). Grey lines offshore indicate plate boundaries. Dark colours indicate deep, light colours shallow seafloor.

In this paper, we will focus on the structures and processes affecting the fore-arc region. For comparison, we will use the gravity field and results of the density modelling from Central America. Therefore, we provide a brief introduction to the geology of the region. For more detail, refer to Lücke *et al.* (2010). The outstanding tectonic feature is the subduction of the oceanic Cocos plate beneath the Caribbean plate along the Middle American Trench. Throughout Central America, the volcanic front is segmented along the isthmus presenting gaps in Quaternary volcanism as well as changes in distance from the Middle American Trench. Such changes have been attributed to both the state of stress in the overriding plate and the disposition of the subduction zone leading to changes in depth to the slab (Bolge *et al.*, 2009). The heterogeneity of the structure of the oceanic Cocos plate due to the influence of the Galapagos hot-spot (Sallarès *et*

al., 2003) leads to inconsistencies upon the arrival of bathymetric features to the subduction zone and may cause seismogenic asperities and uplift (Barckhausen *et al.*, 1998, Meschede *et al.*, 1998). Furthermore, the subduction of seamounts on the oceanic Cocos plate acts as an agent of upper plate erosion (Ranero and von Huene, 2000). At the western end of the Middle American Trench, the plate boundary between the Cocos and Nazca plates is marked by the seismically active Panama Fracture Zone. Subduction of the Nazca plate along the southern Panama segment is now considered to be inactive showing instead evidence of left lateral shearing between the Nazca and Caribbean plates (Lonsdale, 2005).

2.3 Gravity database and geophysical constraints

Onshore gravity data collected under the framework of the Collaborative Research Centre 267 (Oncken *et al.*, 2006) have been homogenized to compile Bouguer anomaly map of the Central Andes. The database comprises data acquired over the past 30 years in Argentina, Chile and Bolivia (20° S to 29° S and 74° W to 64° W). Approximately 2000 gravity stations covering the region in Argentina between the Andes and the Atlantic coast were measured along the southern traverse in 2000 (36° S and 42° S and 71° W and 62° W) and along the northern traverse between 1982 and 1990 (Götze *et al.*, 1994, Hackney *et al.*, 2006, Schmidt and Götze, 2006, Alasonati-Tašárová, 2007). Additional data have been obtained from industry (ENAP; Chile and Repsol-YPF; Argentina), the Universidad de Chile and the United States National Imagery and Mapping Agency. All measurements are tied to the IGSN71 gravity datum. Bouguer anomalies were computed using the normal gravity equation of 1967 and a spherical Bouguer cap correction (cap radius 167 km, density 2670 kg m⁻³). Terrain corrections on land were computed using triangular facets to approximate topography up to a distance of 167 km from stations. The corrections were applied using the 1×1 km GLOBE (onshore) and ETOPO5 (offshore) digital elevation models. Offshore gravity and seismic data are obtained from shipborne measurements of the SPOC (Subduction Processes Off Chile) project (e.g. (Reichert and Schreckenberger, 2002). The former are merged with the KMS-2001 global free-air gravity anomaly database (Andersen and Knudsen, 1998). The Bouguer anomaly in the Central Andes has a resolution of 3 – 5 x 10⁻⁵ m s⁻².

A series of 3-dimensional density models showing mass distributions at different scales in the western continental margin of South America have previously been developed (Kirchner *et al.*, 1996, Tassara *et al.*, 2006, Alasonati-Tašárová, 2007, Prezzi *et al.*, 2009). Tassara *et al.* (2006) presented a sub-global density model (410 km depth) encompassing the Pacific Ocean (85° W) and the Andean margin between the northern Peru (5° S) and Patagonia (45° S). At a regional scale, 3D density models of the Central (between 36°S – 43°S) and South Central Andes have been developed by Kirchner *et al.* (1996), Alasonati-Tašárová (2007) and (Prezzi *et al.*, 2009). All models traverse the Andes and provide complete picture of lithospheric density distributions. Modelling was done using the 3D gravity modelling package IGMAS (Götze and Lahmeyer, 1988, Schmidt *et al.*, 2010). Model constraints were taken from active and passive seismic campaigns conducted under the framework of the Collaborative Research Centres 267 (Giese *et al.*, 1999, Oncken *et al.*, 2006, Sick, 2006) and 574 (Ranero *et al.*, 2003, Brasse *et al.*, 2009). Moreover, results of the previous seismic experiments from PISCO (Proyecto de Investigación Sismológica de la Cordillera

Occidental; (Lessel, 1997, Schmitz *et al.*, 1999), ANCORP (Andean Continental Research Program; ANCORP (Group, 2003, Buske *et al.*, 2002) and ISSA (Integrated Seismological experiment in the Southern Andes;(Bohm *et al.*, 2002, Lüth *et al.*, 2003) have been used to constrain major structures such as Moho, upper slab surface, lithosphere-asthenosphere boundary and intra-crustal inhomogeneities.

For Central America, a similar database was compiled and homogenised. Offshore databases consisting of ship borne gravity and seismic data acquired within the activities of the Collaborative Research Centre 574 have been used to cover mainly the area along the Middle American trench and the Pacific continental shelf. Seismic reflection, refraction and tomography data sets provided constraints for the modelling (Sallarès *et al.*, 2001, Sallarès *et al.*, 2003, Husen *et al.*, 2003, Arroyo *et al.*, 2009). The onshore gravity database was also compiled by SFB574 members and consists of data from various government and academic institutions. Bouguer and terrain corrections were carried out following similar processing procedures as for the Andean gravity dataset.

2.4 Results and discussions

2.4.1 Geophysical and Geodetic Bouguer anomaly

The definition of Bouguer anomalies is different in Geophysics and Geodesy. In order to avoid confusion, the differences between “gravity anomalies” and “gravity disturbances” will be explained. Detailed discussions about this issue can be found in the work of Li and Götze (2001) and Hackney and Featherstone (2003). In general, for geophysical interpretation and modelling, “geophysical Bouguer anomalies” will be used. Here, the measured gravity is corrected for the normal gravity equation at station elevation as well as for the Bouguer slab and the topographic variations. The measured gravity value is still interpreted at its original height (Figure 2-2). In terms of geodesy, gravity values that are corrected for the normal gravity but still defined at station elevation are called disturbances. The Bouguer anomaly provided by the ICGEM is defined as the gravity calculated at the geoid and corrected for both the normal gravity at the ellipsoid and a plain Bouguer slab (called “classic anomaly” according to ICGEM terms; Figure 2-2;(Barthelmes, 2009)). In the discussions to follow, we will continue to call this the “geodetic Bouguer anomaly”. Downward continuation of the geodetic Bouguer anomaly to the geoid is only valid when it is assumed that all singularities of the gravity field lie below the geoid. This is not the case in regions of high topography. Furthermore, density anomalies located between the geoid and the top of the topography are of interest for geophysical interpretation. Hence, differences between geophysical and geodetic Bouguer anomalies can be high. Moreover, the use of disturbances (geophysical anomalies) is consistent with reduction techniques of existing geophysical terrestrial datasets. Thus, the geophysical Bouguer anomaly should be used in regions of high topography.

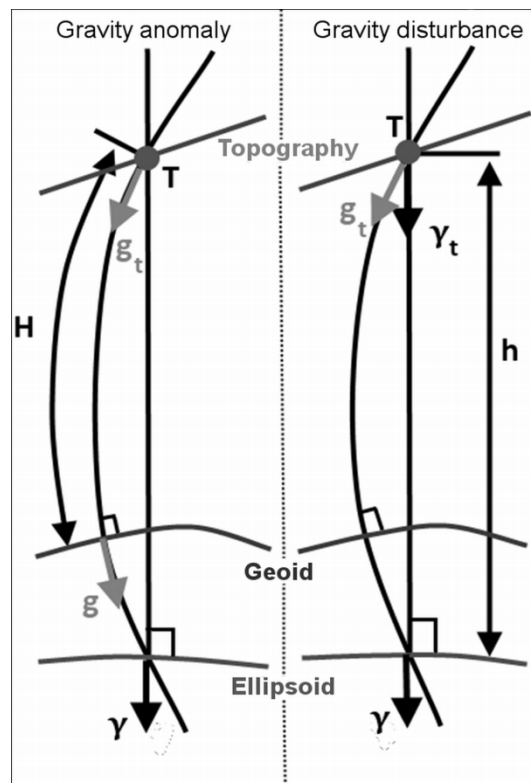


Figure 2-2: Gravity anomaly and gravity disturbance. The gravity anomaly (left) is downward continued from the observation point T to the geoid (g_t to g) and then reduced by the normal gravity from the ellipsoid (γ). Downward continuation is an unstable procedure over mountainous regions. Gravity disturbance (right) can be determined at any level (g_t) and is reduced by the upward continued normal gravity value (γ_t). This procedure is stable.

2.4.2 Data quality of the EGM2008

The EGM2008 consists of GRACE satellite data up to a spatial resolution of approximately 140 km. Data from 140 km spatial resolution up to 10 km are derived from other sources such as terrestrial, satellite altimetry and "fill-in" data (Pavlis *et al.*, 2008). Regarding the additional onshore data, several inconsistencies appear because its availability and distribution is not homogeneous. Moreover, in areas void of any terrestrial gravity data, "fill-in" data were used. These datasets were synthesized from GRACE data and augmented with data from the EGM96 and gravity derived from topography by means of residual terrain model (RTM) (Pavlis *et al.*, 2007). At locations, where confidential terrestrial gravity datasets are available, the data were used up to the maximum resolution permitted by the restrictions and then augmented with RTM anomalies. This approximated gravity solution lacks high frequency anomalies ($>$ degree 1650 (Pavlis *et al.*, 2007)). For the present study, we used terrestrial datasets collected by Schmidt and Götze (2006). It is expected that these data are included in the EGM2008. Thus, the EGM2008 should correlate well with the surface data at its maximum spatial resolution. If the data do not coincide, errors or inconsistencies in the EGM2008 may be assumed.

In the Andes, two onshore areas with different topography were investigated: The North Chilean part is located between 74° W – 67° W/19° S – 30° S. Elevation in this region reaches up to 5800 m above sea level. The southern part (between 73° W – 60° W and 36° S- 43° S) has elevations up to 3000 m. In Central America, the study area is located between 86.5° W – 82° W/8° N – 11.5° N with elevations up to 3800 m. The number of onshore gravity stations used for the Northern Chile, Southern Chile and Central America are 8373, 14210 and 13387, respectively.

Table 1 shows the correlation between the EGM2008 anomalies (geodetic and geophysical) and terrestrial gravity data for the Andes and Central America. In general, the EGM2008 shows high correlation (> 95%) in the Andes. However, low correlation has been obtained over the regions with rough topography, where deviations of about 40 % are observed (e.g. $128 \times 10^{-5} \text{ m s}^{-2}$). The data correlation in Central America is even lower (about 68 % deviations for the geodetic anomaly and ~ 86 % for the geophysical anomaly). This is mainly attributed to sparse terrestrial gravity data coverage.

	North Andes (19° S-30° S) onshore		South Andes (36° S-43° S) onshore		Central America onshore	
	Geophysical BA	Geodetic BA	Geophysical BA	Geodetic BA	Geophysical BA	Geodetic BA
Correlation between EGM2008 and terrestrial data (%)	99.48 (98.29)	98.91 (95.63)	96.51 (93.26)	97.48 (94.32)	85.8 (49.37)	68.2 (40.66)
Min. Deviation ($\times 10^{-5} \text{ m s}^{-2}$)	-50	-128	-66	-77	-55	-203
Max. deviation ($\times 10^{-5} \text{ m s}^{-2}$)	80	87	58	48	112	169

Table 2-1: Correlation of the EGM2008 with terrestrial data. The maximum deviations of each model are shown. The correlation values in brackets are for the Andes west of 69°W. Thus, only stations located around mountainous areas and the coastal line are considered. In Costa Rica, the brackets show the correlation of stations located above 1000 m of altitude.

Figure 2-3 shows the gravity maps of Central America and the Southern Andes in which the geodetic and geophysical Bouguer anomalies are compared with terrestrial data. The histograms in Figure 2-4 show the deviation of the geodetic (dotted) and geophysical (hatched) anomaly compared to the terrestrial data in the Andes. The deviation of the geodetic anomaly compared to the geophysical anomaly is larger ($\sim 0.6\%$) in the northern part where topography is higher. In the southern part, the geodetic anomaly is slightly better ($\sim 1\%$) than the geophysical anomaly. However, both datasets show significant deviations from the terrestrial data with values higher than $20 * 10^{-5} \frac{m}{s^2}$.

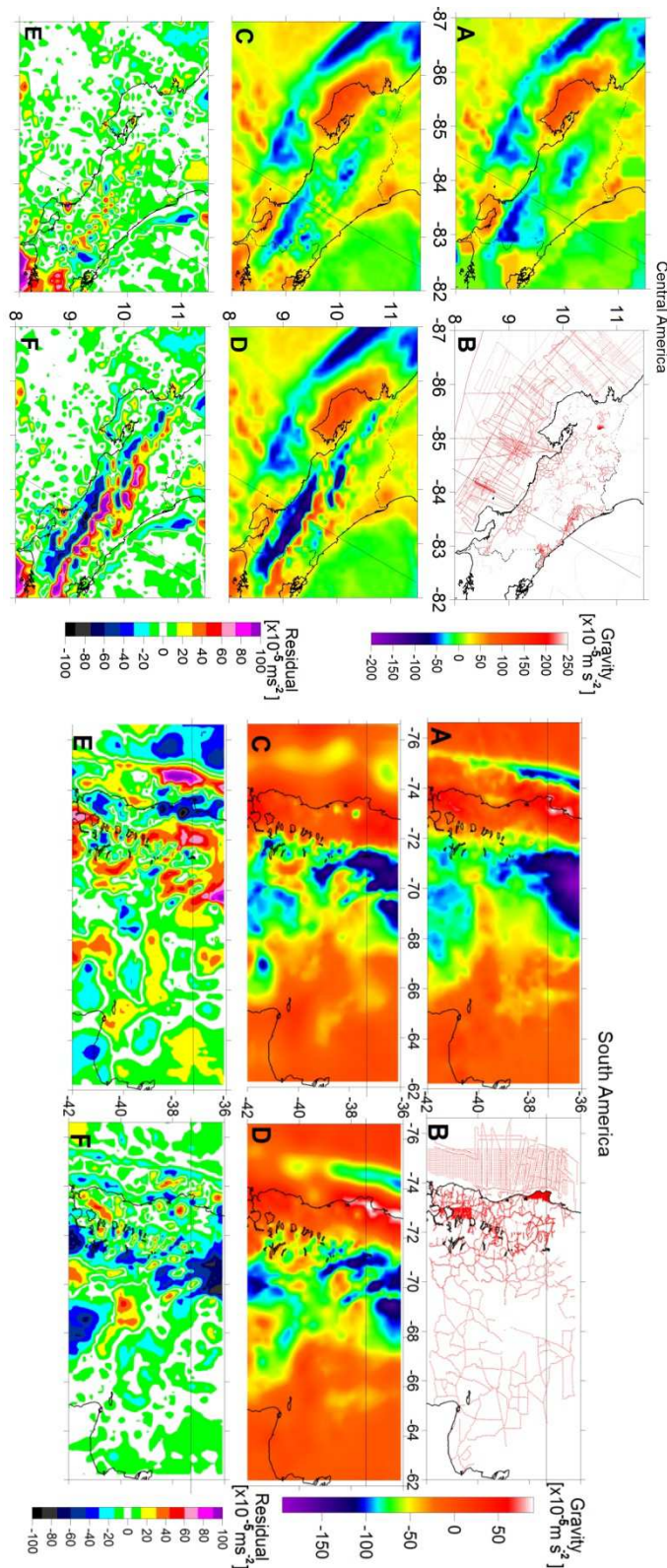


Figure 2-3: Comparison of the EGM2008 with surface gravity data from Costa Rica (top) and Chile (bottom). (a) Data from surface stations with Bouguer gravity anomaly on-shore and free-air gravity anomaly off-shore; (b) Location of surface stations; (c) Geophysical Bouguer anomaly (from EGM 2008); (d) Geodetic Bouguer anomaly (from EGM2008); (e) Residual map obtained by subtracting (a) from (c); (f) Residual map obtained by subtracting (a) from (d). Bold black lines show the coastline and borders. Straight line shows location of cross-section of the 3D density model shown in Figure 2-5 and Figure 2-6.

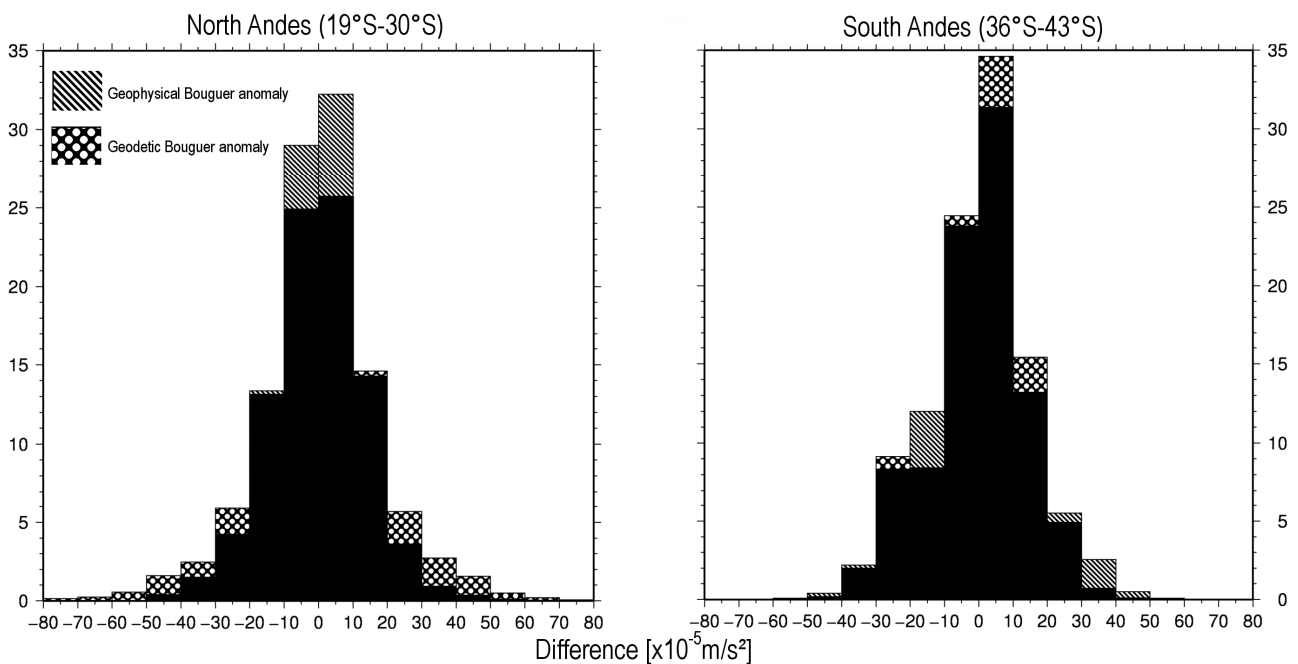


Figure 2-4: The deviation of the geodetic Bouguer anomaly (dotted) and geophysical Bouguer anomaly (hatched) from terrestrial data. The area, marked in black, indicate the overlapping of both datasets. In the northern Andes, the fit of the geophysical Bouguer anomaly is better. Most values are in the range of $\pm 10 \times 10^{-5} \frac{m}{s^2}$. In the southern part, the geodetic Bouguer anomaly fits much better to the terrestrial data. Thus, the resolution of the geophysical anomaly is better in areas of large topography. However, large deviations from original datasets make the EGM2008 less reliable in these regions.

For Central America, a three dimensional density model is being developed within the framework of the SPP1257. The density model is based on gravity data from the EGM2008 geopotential model. The results have shown that the resolution of this model is appropriate for the modelling of regional lithospheric mass distribution and major tectonic structures such as the Middle American subduction zone, the continental and oceanic Moho as well as first order crustal discontinuities represented by the heterogeneities in the crustal basement and the upper crust (see Figure 2-5).

Figure 2-5 shows a cross-section of the 3D density model through central Costa Rica in which different datasets are compared and put into the context of the modelled structures. In the offshore areas, a good correlation has been obtained between the EGM2008 satellite gravity model and surface data. The geophysical Bouguer anomaly (offshore) is located on the geoid (on the ocean surface). Thus, it coincides with the geodetic Bouguer anomaly. Onshore, the geophysical Bouguer anomaly shows better correlation to the surface data than the geodetic Bouguer anomaly. In the mountainous areas of Costa Rica, the geodetic Bouguer anomaly (dashed line) differs significantly from the surface data (dotted line) as well as from the geophysical Bouguer anomaly (black).

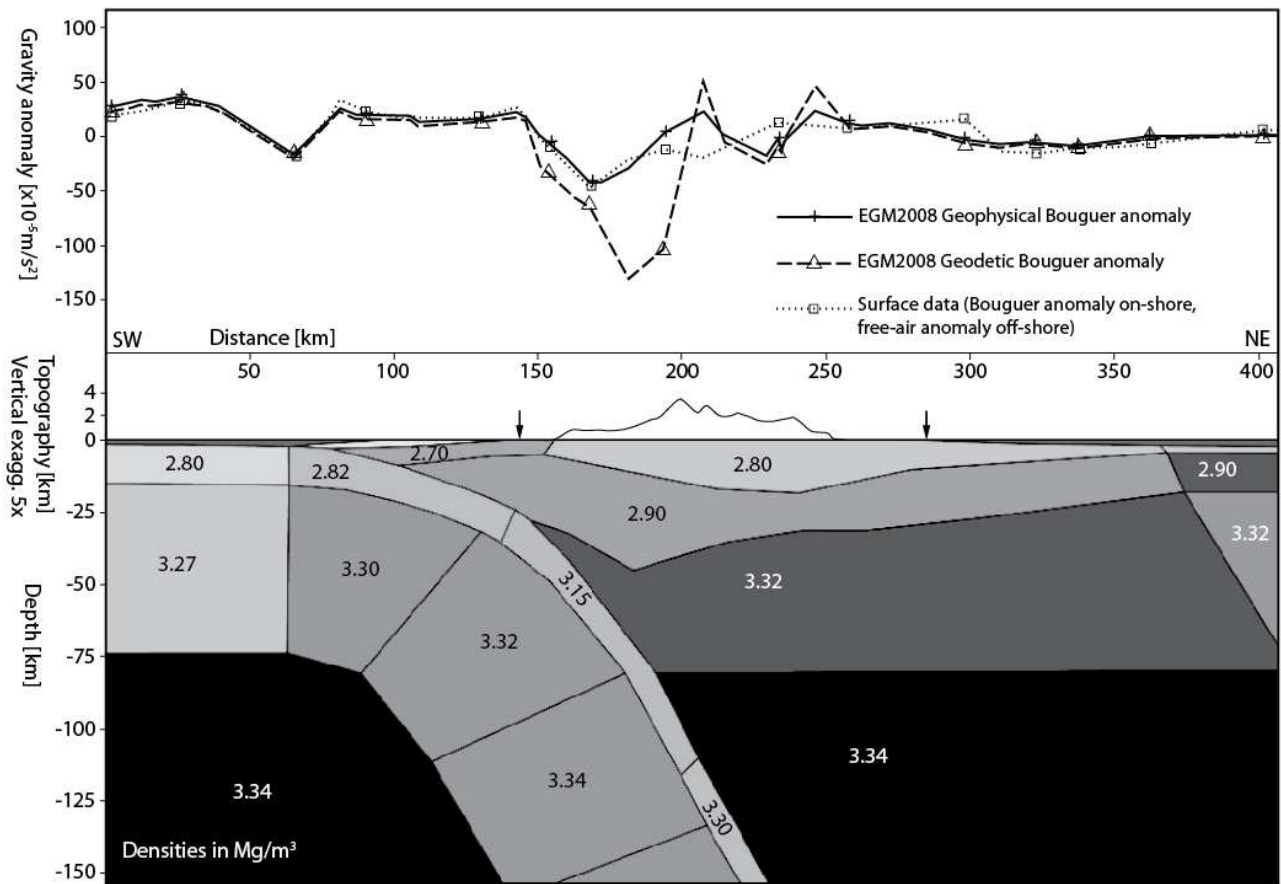


Figure 2-5: Vertical cross-section of a 3D density model from Central America. Different gravity anomalies are shown in the upper panel. The dotted line (with boxes) is derived from surface gravity data and shows the geophysical Bouguer anomaly on-shore and free-air anomaly off-shore (shoreline indicated by arrows). The dashed line (with triangles) shows the geodetic Bouguer anomaly on- and off-shore calculated from the classical gravity anomaly using EGM2008 model (off-shore without Bouguer reduction). The black line (with crosses) shows the geophysical Bouguer anomaly. Offshore, all datasets correlate. Onshore, however, there is still correlation with surface data, but the geodetic Bouguer anomaly shows errors of about $80 \times 10^{-5} \frac{m}{s^2}$ for this cross section. In this region, elevation reaches up to 3700 m. The errors emphasize the uncertainty of the combined gravity models and instability of the downward continuation method.

The analysis of the present study shows that rugged topography downgrades the spatial resolution of the EGM2008 featuring large outliers in the Andes and Central America. Results in Central America show that high and unexpected deviations can be present in areas void of any terrestrial gravity data. Thus, the quoted spatial resolution of 10 km is not valid for all regions. Our case studies in these regions show that in areas of rugged topography, the geophysical anomaly often provides better results (up to 9% in mountainous regions; Table 1). Moreover, the use of geophysical anomalies in the calculation is consistent with the existing reduction techniques of terrestrial geophysical datasets.

2.4.3 Spatial resolution of different satellite gravity models

The main geophysical objective of using satellite-derived gravity data is the interpretation of lithospheric structures. We have used a well-constrained 3D density model of the South-Central Chile (Alasonati-Tašárová, 2007) to assess the spatial resolution of different satellite gravity models. The comparison emphasizes the areas of the models in which problems may occur when using different satellite gravity models (EGM2008, EIGEN-5C, ITG-GRACE03s, and GOCO-01s).

Figure 2-6 shows a section of the 3D density model from the Central Chile at 37.4° S. Also shown on the top panel are gravity fields derived from different satellite models, measured surface gravity data, and the calculated gravity field from the density model. The dashed black line illustrates the calculated gravity from the density model and the red line shows the measured surface data. The EGM2008 (black) and the EIGEN-5C (yellow) show overall good correlation with the calculated gravity field. In the area of high topography (e.g. at 100 km of the x-axis), the EGM2008 exhibits significant deviations. The EIGEN-5C is smoother and correlates better with the predicted field. However, a deviation of about $15 * 10^{-5} \frac{m}{s^2}$ is observed between 350 and 400 km. The same misfit is visible in the GRACE solution (dark blue). The GRACE-GOCE satellite model (light blue) provides a better fit to the calculated gravity. Here again, deviations at 200 and 420 km are observed. However, the gravity low below the Andes at 300 km is better resolved by the GRACE-GOCE model. The gravity low of the deep-sea trench is well fitted by the combined models but the GRACE model does not comprise a distinct gravity low. Compared to other models, the deep-sea trench and the root of the Andes are more visible in the GRACE-GOCE model. The Coastal Cordillera is also shown as gravity high, but not well fitted in amplitude. The new GRACE-GOCE satellite model shows the best fit. The EIGEN-5C provides a good fit over the entire section. The deviation of the EGM2008 in regions of high topography is clearly visible in areas where no surface data is available. The higher degree models such as the EGM2008 and EIGEN-5C cannot provide a high spatial resolution.

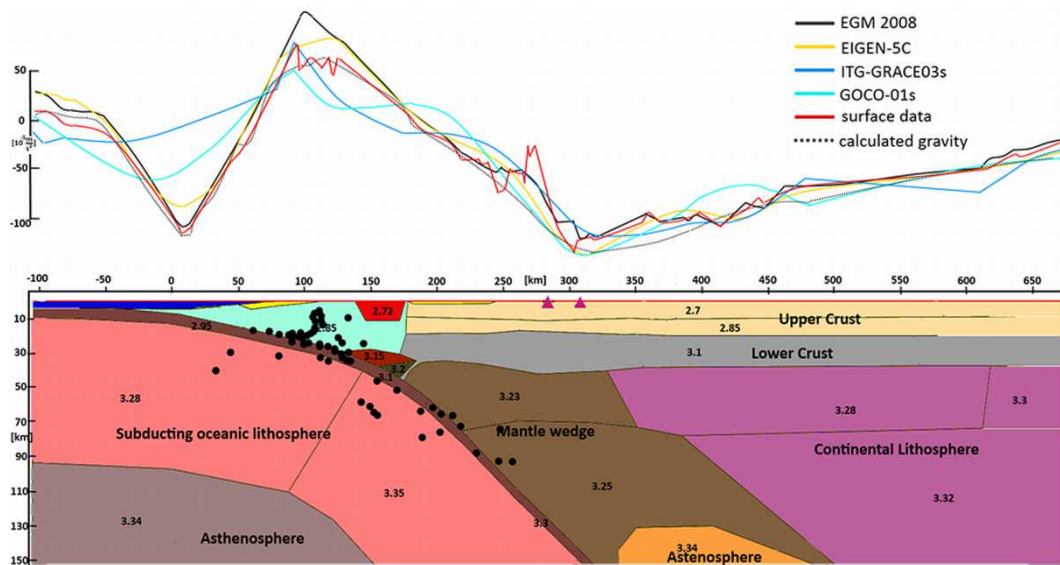


Figure 2-6: Vertical cross-section of a 3D density model from Central Chile at 37.4°S (Alasonati-Tašárová, 2007). The model is constrained in part by geological and seismological information (e.g. hypocentres are shown as black circles). The dashed line shows the calculated gravity from the model matched to the surface gravity data (red curve). The combined EIGEN and EGM2008 models fit well to the data. The EIGEN-5C (yellow) correlates well with the predicted gravity values, but it also shows some deviations. The ITG-GRACE03s model does not adequately show the gravity lows of the deep sea trench (at 10 km) and crustal root (at 300 km). The GOCO-01s (light blue) model shows the best correlation of all satellite only models.

Overall, the GRACE-GOCE model shows an increased spatial resolution relative to the GRACE derived field. Since large-scale density models do not resolve local features, the calculated gravity field is smooth and comparable with wavelengths obtained from satellite-only gravity models. Combined models with new GOCE data could be sufficient for compiling density models of regional scale in frontier regions. Although combined gravity models can be used for density modelling of relatively smaller features such as shallower crustal structures, satellite-only models are not appropriate for this purpose due to the low spatial resolution.

2.4.4 Asperity mapping and resolution of gravity gradient data

Delineation of potentially hazardous provinces using gradiometry is one of our objectives. In order to examine the applicability of GOCE gradients for asperity detection in a simple way, the minimum dimension of a spherical anomalous mass below the geoid producing gravity and gravity gradient amplitudes of the order of GOCE’s accuracy at orbit height (254.9 km) has been calculated. The curves in Figure 2-7 show the minimum diameter of such a mass of given density contrast required to produce signal differences of $1 * 10^{-5} \frac{m}{s^2}$ and $12 * 10^{-12} s^{-2}$ at orbit height. These values are close to the expected accuracies of the gravity and vertical gravity gradient of GOCE global data, respectively (Pail 2011, pers. comm.). As shown in Figure 2-7, an anomalous structure with density contrast of 240 kg m^{-3} could be detected in a gravity data at orbit height, if its diameter is at least $\sim 45 \text{ km}$. However, if the diameter of an anomalous structure increases by up to 100 %, its density contrast should not be less than $33 \frac{kg}{m^3}$ to be detected. If gradients are

considered, even bodies of about half of that size could produce signal in the range of GOCE's gradient data sensitivity. The dimension of Jurassic arc batholiths in Northern Chile is about 60-120 km (Götze *et al.*, 1994, Husen, 1999, Götze and Krause, 2002, Sobiesiak *et al.*, 2007). This supports the idea that batholithic structures, which are assumed to be related to asperity generation, can be detected using GOCE data.

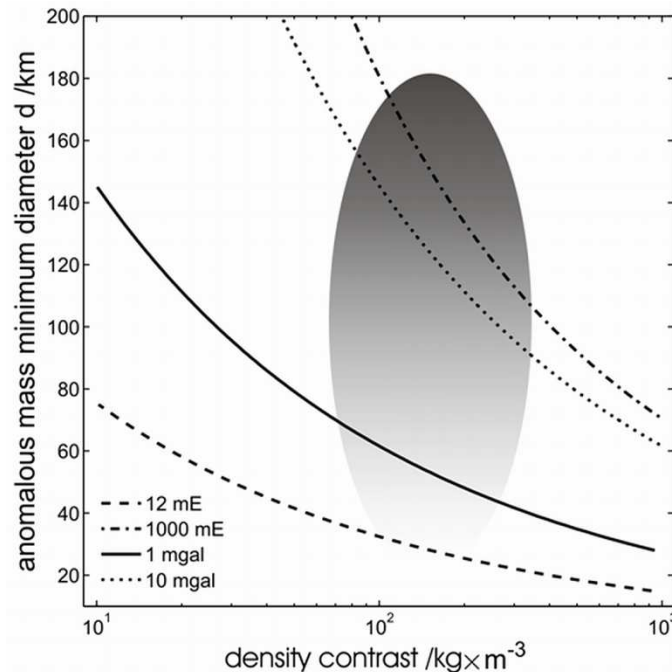


Figure 2-7: Differential gravity and gradient signal caused by a minimum diameter of an anomalous spherical mass of given density contrast below geoid at an orbit height of 254.9 km. The signal is in the range of GOCE's resolution. The thick solid and dotted lines represent differential gravity signals of 1 and $10 \times 10^{-5} \text{ m s}^{-2}$ at an altitude of 254.9 km, respectively. The thin dashed and dash-dotted lines represent gradients of 12 and 1000 mE, respectively. The grey shaded area shows the possible combination of parameters of an asperity generating batholithic structure near subduction zones.

Furthermore, we set up a synthetic model of an arbitrary subduction zone for 3D-density forward modelling. The geometry and density parameters have been adapted from the models developed by Sobiesiak *et al.* (2007) and Alasonati-Tašárová (2007). In order to test the signal response of asperity generating structure at different station heights using forward modelling, a three dimensional anomalous structure (115 x 200 x 45 km) with physical properties resembling the Chilean batholiths has been included in the modelling. A density of $3 \times 10^3 \text{ kg m}^{-3}$ (density contrast of 0 to 300 kg m^{-3}) has been chosen for the batholith body in the model. At the height of 254.9 km, the magnitude of the gravity gradient anomaly ranges from few to some hundred mE (1 mE = $1 \times 10^{-12} \text{ s}^{-2}$). Being the second spatial derivatives of the gravity potential, gradients provide 'sharper' images of anomalies and can be combined into coordinate independent *invariants* (e.g. (Pedersen and Rasmussen, 1990). Invariants sharpen density contrasts and help to emphasise structural boundaries. Figure 2-8 shows how well anomalous underground structures of interest can be detected using gravity gradients at orbit height. Different tensor components give valuable

information for geo-scientific interpretation. The above analysis shows that gradient maps from GOCE data may help to delineate major geological structures like fault zones, rims of sedimentary basins and intrusions.

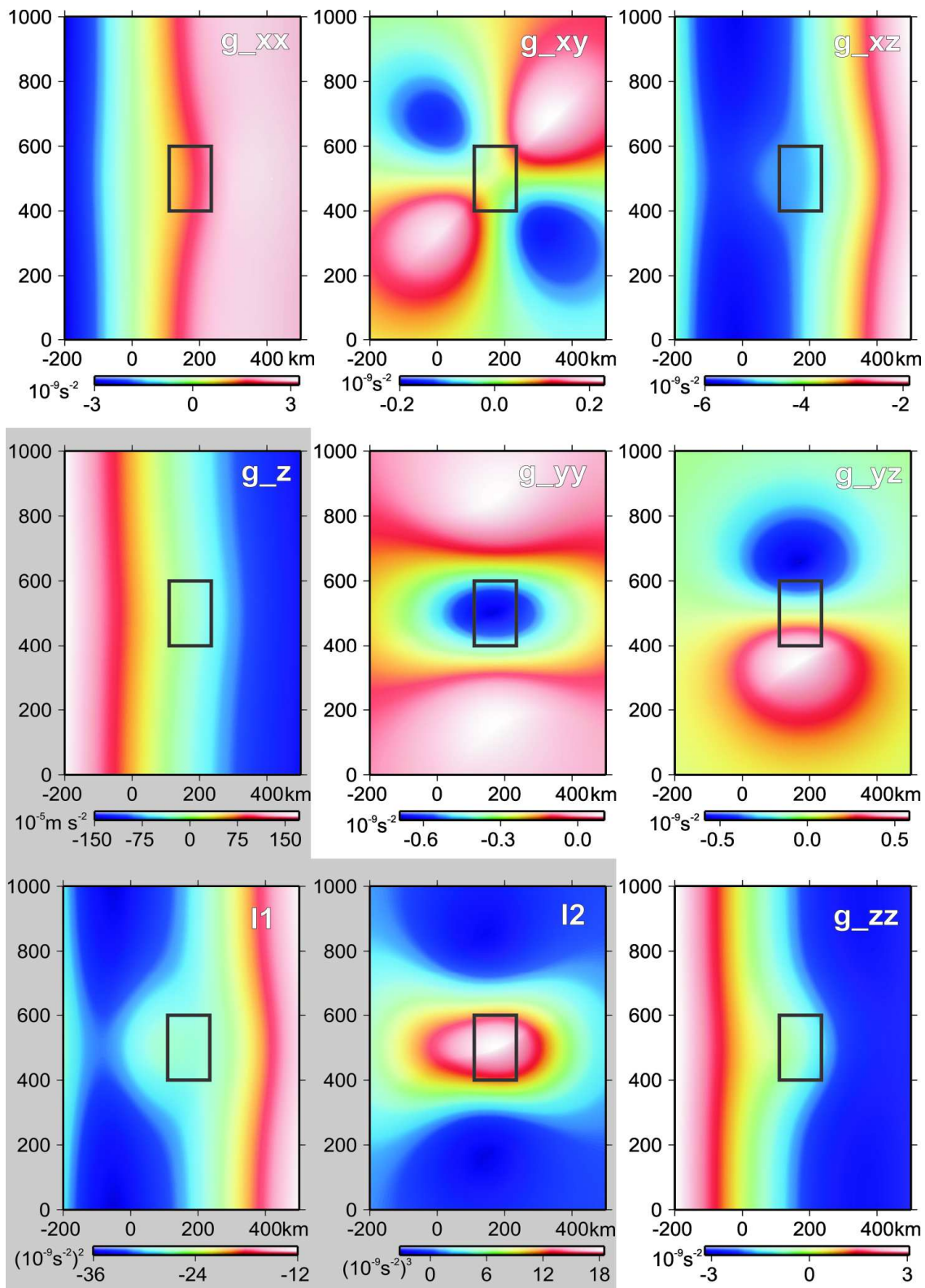


Figure 2-8: 3D-Modelling of synthetic gravity (g_z), gravity gradient tensor and invariants ($I1$ and $I2$) of a subduction zone using vertical gravity field as measured at 250 km height. A batholitic structure (black box) has been included on top of the down-going slab to test the resolution of gravity gradient signal. The gradient maps emphasize the location of the batholitic structure and the general geological strike of the subduction zone.

2.5 Geodynamic model of the Andean margin as constrained by satellite gravity data

The present mass distribution is the result of long and complex geodynamic processes. Therefore, dynamic modelling is necessary to include the effects of time factor to the static density models. The dynamic evolution of the Andean margin has been extensively studied using numerical modelling. This includes studies of the dynamics of the plateau foreland (Babeyko and Trumbull, 2006), the factors controlling the intensity of tectonic shortening (Sobolev *et al.*, 2006) and the influence of curvature of the convergent plate margin on the stress distributions (Boutelier and Oncken, 2010). These existing models are constrained by geophysical and geological data, but are based on generalized geometries. One of the objectives of this study is to develop a dynamic model of the Andean margin using realistic geometries from a well-constrained density model. In the present study, the geometries of the 3D dynamic model have been imported from the regional 3D density model of the Andean margin (Tassara *et al.*, 2006). The model has 16 tectonic units including the lithosphere and the upper mantle down to a depth of 410 km.

Figure 2-9 shows the visco-elastic 3D dynamic model of the Andean margin. The size of the model is 1730 km x 725 km (area between 16-22°S and 78-63°W). The densities of the units have been adopted from the density model of Tassara *et al.* (2006). Young's moduli have been calculated using the v_p velocities from the ANCORP profile (ANCORP Working Group, 2003) and the P-S wave velocity relation $v_p = 3^{1/2} v_s$. The corresponding Poisson ratio for all units is 0.25. The parameters of the geological units are shown in Figure 2-9. The asthenosphere has been modelled as a viscous-elastic medium. The lithosphere is pure elastic. In the modelling, it is assumed that the South American plate is fixed and the Nazca plate moves by 7.8 cm/year for 200,000 years (Somoza, 1998). It is assumed that friction occurs only in the uppermost part of the contact up to approximately 40 km depth with a frictional coefficient of 0.1.

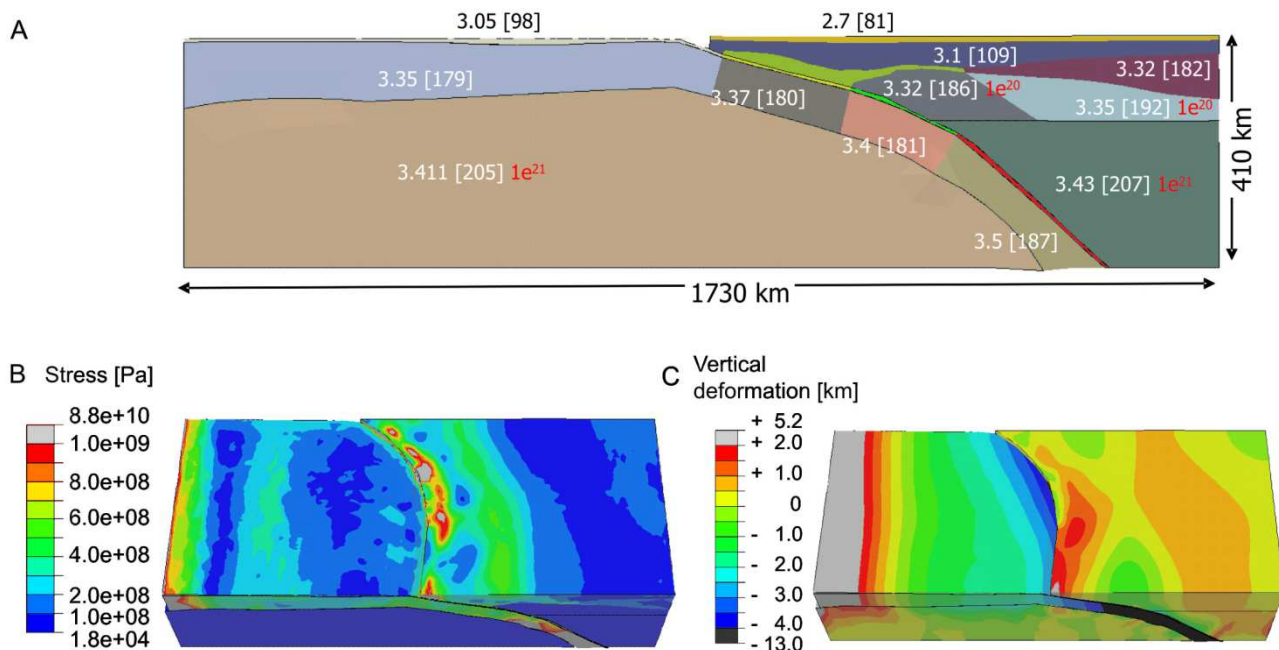


Figure 2-9: Used parameters for the viscous-elastic model (A). Densities [$\times 10^3 \text{ kg/m}^3$], Young's moduli [GPa] in brackets, viscosity in red. Oceanic crust: 3.2 [113] yellow, 3.3 [116] green, 3.55 [125] red, mantle wedge 3.23 [160] olive. Vertical deformations (B) and stress distribution (C).

Beside density, however, Young's modulus, width of coupling zone, frictional coefficient and obliquity of the subducting Nazca plate could influence the dynamics of plate interfaces (Heuret and Lallemand, 2005). In order to study the effects of these controlling parameters, rheologies (e.g. plasticity, viscoelasticity and visco-elasto-plasticity) and temperature on the dynamics of the thrust zone area, more generalized and realistic 3D models have been developed.

Figure 2-9b shows the resulting vertical deformations. The calculated uplift is ~ 1.5 km and this corresponds to 7.5 mm/year. The expected surface uplift is smaller than 2 mm/year (Jordan *et al.*, 1997, Klotz *et al.*, 2006). Though our model neglects erosion, the estimated uplift from the numerical modelling is in the right order of magnitude. Figure 2-9c shows the stress distributions. The stress (high and low) tends to follow the trend of the earthquake distributions in the region. The green belt indicates where the slab is at depth of 100 km.

The present study shows that well constrained geometries are crucial for dynamic modelling. The availability of satellite-derived gravity data has significantly improved the density models of the Andean region lacking terrestrial data. This in turn refined the geometries and densities of the geodynamic models. In particular, the long wavelength satellite-derived gravity anomaly is suitable to constrain the deep structures of the models. The resulting stress fields and new petrologic models can help to improve the density structure of the static models. Thus, a direct link between the static and dynamic models could be established.

2.6 Conclusions

Thorough understanding and interpretation of dynamic processes associated with hazardous regions is one of the major research interests in geosciences. Combined gravity models can provide valuable information for density modelling and geological interpretation where terrestrial gravity data of high resolution are available. In this study, it is shown that gravity prediction and downward continuation in some areas, e.g. the mountain ranges over Costa Rica and Central Andes, could lead to large errors and reduce the reliability of gravity data. Gravity prediction based on topography may not be appropriate for those regions. This calls the need to improve reduction techniques such as Bouguer calculation, topographic correction as well as downward continuation. The satellite only models have low spatial resolution compared to terrestrial data. However, the resolution is sufficient for interpretation of large-scale structures. Especially, in frontier regions such as parts of the Andes or Central America, where terrestrial gravity data coverage is limited, these models are valuable.

3D modelling of synthetic gradients and invariants of subduction zones, using the Andean as case study, proved the applicability of gradient measurements for detection of the edge of geological structures. Therefore, gradients from GOCE mission can resolve structural information and improve interpretation of asperities.

The long term and complex geodynamic processes of subduction could only be fully understood if model predictions are constrained with surface observables such as satellite gravity data. In the present study, a geodynamic model of the Andean margin has been developed with a realistic geometry based on density model constrained by gravity data and other relevant prior information. The stress distributions in the fore-arc, as determined from the dynamic modelling, mostly coincide with the locations of the earthquake of the region.

Finally, mapping and interpretation of hazardous regions require good gravity database (among others) to constrain lithospheric and dynamic processes. Satellite gravity data provide globally best information about frontier regions. Therefore, it is possible to interpret structures globally without limitations and combine regional interpretation of different regions into a one big picture.

3 Topographic correction of gravity (gradient) data

Topographic correction is always the subtraction of a model which represents "known" mass sources of the investigation area. For lithospheric investigations, the attraction of topography is not of interest. Therefore, the corrections should remove all caused by topography in a form that only subsurface features remain. For this purpose, an accurate representation of the topographic masses is mandatory. This implies a very good representation of the topographic geometry. This is a complex and complicated task in areas of rugged topography.

Chapter 2.4.2 showed large differences between different Bouguer gravity datasets, in particular satellite data, which are observed in areas of high topography. Therefore, a reliable and consistent mass correction is necessary before the gravity data can be used for modelling and interpretation.

Today, the availability of high resolutions satellite data and global gravity models makes it possible to investigate large and regional areas (Satellite data resolves wavelength of 100 - 200 km) without acquiring any new data. Therefore, it is even more important to correct for topography in a consistent way for large areas. Numerous approaches exist to correct for this effect. Most algorithms approximate the topography by simple bodies like prisms, cylinders or mass lines. The topographic correction also includes some pre-assumptions like the correction radius of 167 km (Mikuška *et al.*, 2006). Geometry approximations (e.g. prisms, mass lines) might cause deviations from the real surface and user defined parameters (correction radius) are questionable and seem arbitrary. Since long, these assumptions and their influence on the results will be discussed (e.g. Talwani (1998) and (LaFehr, 1998)). In the past, topographic and gravity data was not available in such high resolution at such large scales. Several algorithms and their design fitted needs for small investigation areas (e.g. (Talwani, 1998)). Today, the variety of different datasets (local surveys to satellite data), the size of possible investigation areas and the availability of high resolution digital terrain models (DTMs) ask for new approaches of topographic correction. These should be robust for large DTMs, consider sphericity of the earth and should represent the geometry of topography as best as possible. In addition, the most recent GOCE mission provides measured gravity gradients of the gravity field. Therefore, a new algorithm has to be correct for gravity gradients caused by topographic masses. This section will include a historical overview about the development of topographic correction, an overview about existing methods and a new consistent, fast and reliable approach to correct for topography which includes all requirements for satellite data correction. Several test beds will be discussed which show the differences between the results of selected algorithms for several input data. The conclusion gives recommendations for a reliable topographic mass correction.

The next chapter will introduce some standard correction procedures and give an overview about the historical development of topographic correction.

3.1 Historical development of topographic correction and state of the art

The vertical gravity component is used for interpretation and modelling of the subsurface. Gravity measured at an arbitrary point P consists beside of the anomaly signal many other effects (Meurers, 2009) :

$$g(P) = \gamma(P_E) + \underbrace{\int_0^H \frac{\partial \gamma}{\partial z} dz + \int_H^{N+H} \frac{\partial \gamma}{\partial z} dz}_{\int_0^h \frac{\partial \gamma}{\partial z} dz} + \underbrace{\delta g_{T,0 \rightarrow N}(P) + \delta g_{T,N \rightarrow N+H}(P)}_{\delta g_{T,0 \rightarrow h}(P)} + g_s(P) \quad (1)$$

where P_E is the projection of P down to the ellipsoid,

h and H are the heights of P above ellipsoid and geoid respectively ,

N is the geoid height,

γ is the normal gravity,

$\int_0^h \frac{\partial \gamma}{\partial z} dz$ is the normal gravity at the observation point,

$\delta g_{T,0 \rightarrow h}$ is the topographic effect of all masses between ellipsoid and topography,

and $g_s(P)$ is the gravity effect of all density inhomogeneties.

The normal gravity gradient and the effect of all masses are split up in two integrals. One running in an interval from the ellipsoid to the geoid and one from the geoid to the height of the station. This accounts for the geophysical indirect effect (Figure 3-1, (Li and Götze, 2001)). The geophysical indirect effect appears, when corrections of gravity are made with orthometric instead of ellipsoidal heights. The normal gravity calculation (equation 4) relates to an ellipsoid which approximates the mass of the earth. If orthometric heights are used for correction, the calculation does not correct the masses between ellipsoid and geoid. However, orthometric heights were used in the past, because ellipsoidal heights could not be measured directly (Figure 3-1). Today, ellipsoidal heights are available by GPS measurements. The indirect effect is described in many publications (e.g. Li and Götze (2001), Hackney and Featherstone (2003)). It is related to the shape of the geoid which is a long wavelength feature. Therefore, most authors conclude that the indirect effect can be neglected if the surface of the geoid is not changing too much within the surrounding of the observation point.

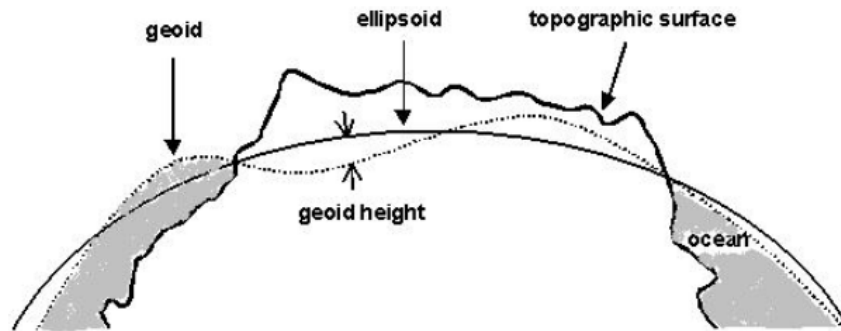


Figure 3-1: From Li and Götze (2001). "Cartoon showing the ellipsoid, geoid and topographic surface"

In this case, the effect only causes an (almost) constant shift for all stations. However, for large investigations (e.g. continent scale) one should test how the indirect effect affects the investigation area. If the effect is large, ellipsoidal heights should be used for correction. If the indirect effect is ignored, the Bouguer anomaly is calculated by the following equation:

$$\begin{aligned}
 g_{BA} &= g(P) - \gamma(P_E) - \int_0^H \frac{\partial \gamma}{\partial z} dz - \delta g_{T,N \rightarrow N+H}(P) \\
 &= g_s(P) + \underbrace{\int_H^{N+H} \frac{\partial \gamma}{\partial z} dz}_{\substack{\text{Gravity} \\ \text{height} \\ \text{gradient}}} + \underbrace{\delta g_{T,0 \rightarrow N}(P)}_{\substack{\text{gravity effect of geoid}}}
 \end{aligned} \tag{2}$$

In this thesis, the indirect effect will not be discussed. All tests and comparisons with other data relate to geoidal heights. In particular, this eases the comparison with already processed data. If gravity differences calculated by different methods are discussed, the calculations bases on the same DTMs, thus the indirect effect equals in all results.

Therefore, we ease the reduction equation to:

$$g_{BA} = g(P) - \gamma(P_E) - \int_0^H \frac{\partial \gamma}{\partial z} dz - \delta g_{T,0 \rightarrow H}(P) = g_s(P) \tag{3}$$

$\gamma(p_E)$ can be calculated with the 1980 International Gravity equation (Moritz, 1980):

$$\gamma_{1980}(P_E) = 978032.7(1 + 0.053024 * \sin^2 \phi - 0.0000058 * \sin^2 \phi) \tag{4}$$

where ϕ is the latitude.

The height gradient $\int \frac{\partial \gamma}{\partial z} dz$ for the modern GRS 80 ellipsoid can be calculated in this manner:

$$\int \frac{\partial \gamma}{\partial z} dz = -(0.30877 - 0.00045 \sin^2 \phi) * h + 0.000072 * h^2 \quad (5)$$

The remaining part of the Bouguer gravity equation is $-\delta g_{T,0 \rightarrow H}(P)$. This is the effect of all topographic masses bounded by the surfaces of geoid and station. The effect of topography cannot be estimated in an analytic equation. It has to be approximated and calculated for each specific area. Pierre Bouguer discovered already in the 19th century that the Andean mountain range was influencing his gravity measurements. He stated, that the measured data has to be corrected for the effect of topographic masses to interpret structures in the subsurface. The so called plain (or flat) Bouguer plate is an infinite plate (in horizontal dimension) with the height of a station. The effect is calculated with the gravity response of a cylinder with infinite radius (Bäschlin, 1948):

$$\Delta g_{BPL} = -2\pi\rho G * \lim_{R \rightarrow \infty} \left(R^2 \sqrt{1 + \left(\frac{z}{R}\right)^2} - R^2 \sqrt{1 + \left(\frac{z+H}{R}\right)^2} + H \right) = -2\pi\rho G * H \quad (6)$$

where ρ is the density, G is the gravitational constant,

R is the radius of the cylinder,

z is the distance to the station

and H is the height of the cylinder.

This correction is quite rough because it does not account for sphericity of the earth undulation of topography. Bäschlin (1948) showed an analytical solution for a spherical Bouguer slab (or cap):

$$\begin{aligned} \Delta g = 4\pi G \rho R \left[\frac{1}{6} * (3 - 14x^2 + 12x^4 + (3 - 2x^2)y + y^2)p' \right. \\ \left. - \left(\frac{\sqrt{4x^2}}{6}\right) (3 - 14x^2 + 12x^2) - \frac{1}{6} (3y + 3y^2 + y^3) \right. \\ \left. - 2x^2(1 - x^2)(1 - 2x^2) * \ln \left(\frac{2x^2 + y + p}{2x^2 + \sqrt{4x^2}} \right) \right] \quad (7) \end{aligned}$$

where G is the gravitational constant, ρ is the density

$$x = \sin\left(\frac{\theta}{2}\right), y = \frac{h}{R}$$

h is slab thickness,

R radius of the sphere,

θ angle in degree (e.g. $1.5^\circ \approx 167$ km)

and $p' = \sqrt{4x^2 + 4x^2y + y^2}$.

This equation made it possible to account for sphericity of the earth. Now, it was still necessary to correct the measurements for deviations of topography from the Bouguer slab. Until today, many approaches for topographic reductions were developed. The most representative publications will be referenced next: First, Helmert (1884) introduced a method to account for topography close to a station with cylinder ring compartments. Hayford and Bowie (1912) described the need of correcting the Bouguer plate for topographic undulations for 22 km around the station. They developed a chart showing different zones with increasing extend around each station. In each zone the height were averaged and used for the correction with cylinder ring compartments. Figure 3-2b shows a hammer chart as used by Hayford and Bowie (1912). These first approaches were "station dependent". For each station, a transparent hammer chart was put on a map and for each compartment an average height was calculated. This resulted in redundant calculations for the mean height values. Especially for nearby stations almost same areas were averaged many times. Therefore, the station dependent algorithms were very time consuming. Furthermore, the cylinder ring compartments had a fixed extension. Areas with rugged topography were represented by a mean height of a fixed size compartment. This could lead to improper averaging of rough terrain areas. A new development were the **station independent** topographic correction. Here, topography in different resolutions was prepared before correction. For each station, dependent on the distance to the station, a different grid resolution were chosen. This reduced the number of calculations significantly. Furthermore, cubes/vertical prisms for representation of topography were introduced to approximate these topographic masses. In general, the vertical gravity component of a prism can be calculated by evaluating this integral (Nagy, 1973):

$$\Delta g = G\rho \int_{z_1}^{z_2} \int_{y_1}^{y_2} \int_{x_1}^{x_2} \frac{z \, dx \, dy \, dz}{(x^2 + y^2 + z^2)^{\frac{3}{2}}} = G\rho \iiint f(x, y, z) \, dv \quad (8)$$

where G is the gravitational constant

ρ is the density,

x, y, z are the prism coordinates related to the origin (station located in the origin)

and $x_1, x_2, y_1, y_2, z_1, z_2$ are the limits of the prism.

The analytical integration is complex. Mader (1951) published the analytically closed solutions for this integral. The equation made it possible to describe the terrain by prisms. This made the use of height grids much easier and avoided the Hammer chart representation of terrain by mean heights. In addition, the analytical solution made it possible to calculate the effect of masses very close to the station (e.g. compared to mass point approximations). Nagy (1966) described the use of this equation for terrain correction and presented the gravity calculation. Nagy (1973) improved the equation for more efficient numerical calculation to:

$$g_z = G\rho \left[\left| x * \ln \left(\frac{y + r_0}{y + r} \right) + y * \ln \left(\frac{x + r_0}{x + r} \right) - z * \tan^{-1} \frac{xy}{zr} \right|_{x_1, y_1, z_1}^{x_2, y_2, z_2} \right] \quad (9)$$

where G again is the gravitational constant, ρ is the density and $r_0 = \sqrt{x^2 + y^2}$.

Equation 9 shows that the calculation of a prism is quite complex. The calculation for one prism includes 12 evaluations of the natural logarithm and 6 evaluations of the inverse tangent (for each side of the prism).

The terrain correction conducted by Nagy subdivides an area into prisms with a fixed size (100 m x 100 m). The prisms are located on a UTM grid. The base of all prisms is at sea level, the top is the topographic height derived from the DTM grid. For each station the gravity effect is calculated over all grid nodes of the DTM. This method does not include any change of the prism size. However, sources close to the station have a larger gravity effect than distant sources. The gravity effect of a mass decreases with distance by $\frac{1}{r^2}$ (where r is the distance to the station). This relation implies that the approximation of topography has to be more accurate close to the station than in distance to the station.

Ehrismann and Lettau (1971) developed algorithms (GR1, GR2, GR3; GR stand for gravity reduction) accounting for the decreasing gravity influence by increasing the grid size by distance. Grids with different cell sizes were created station independent for the whole area (Figure 3-2A). Redundant height averaging was avoided which made the approach very efficient. Figure 3-2A shows the calculation scheme of GR3.

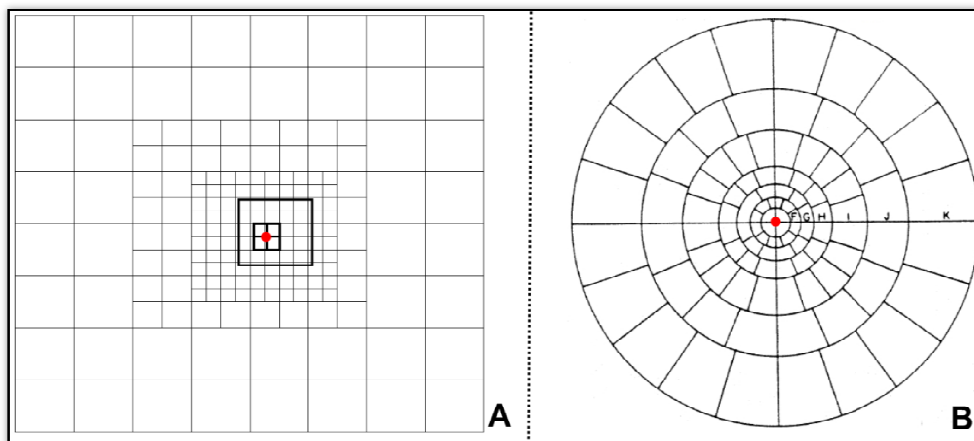


Figure 3-2: (A) shows a calculation scheme of GR3 (after Ehrismann and Lettau, 1971). (B) shows a Hammer chart, as used by Hayford and Bowie (1912). The red point represents a station.

For large survey areas, algorithms should account for sphericity. Therefore GR3 assumed sphericity in its calculation as shown in Figure 3-3. The rotation of the prisms to consider sphericity leads to overlapping areas at the base of the prisms and to gaps at the top. Ehrismann (1972) postulated that this can be ignored if the prisms are small enough.

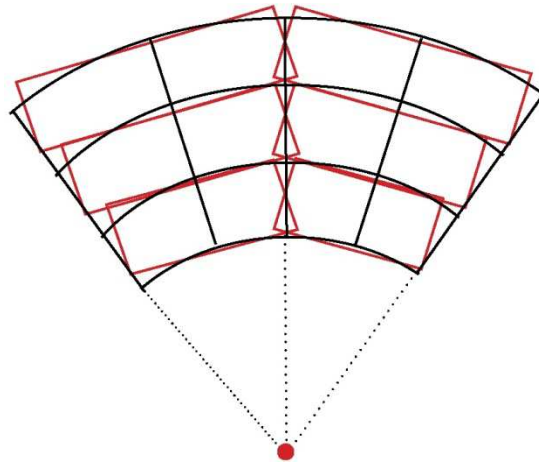


Figure 3-3: (after (Ehrismann, 1972)). The spherical shaped elementary bodies of the Bouguer plate are approximated by prisms (red). They overlap due to the rotation of blocks and leads to gaps on top and overlaps at the bottom of the prisms.

Sideris (1984), Parker (1995), Parker (1996) developed methods for rapid correction of topography with FFT methods. Goltz (1989) showed that the FFT gravity calculation equals the gravity effect of a mass line:

$$\Delta g_{\text{masline}} = \frac{1}{2} G \rho \Delta x \Delta y * \frac{\Delta h^2}{r^3} \quad (10)$$

where G is the gravitational constant, ρ is the density,

$\Delta x, \Delta y$ is the extent of the prism which is approximated by the mass line

Δh is the height difference between the station and the mean height of topography

and r is the distance to the station.

Stations and topography have to be on a regular Cartesian grid for FFT calculation. In general, stations are irregular distributed in geophysical surveys, especially in rugged terrain. The FFT calculations are performed at a plane, accounting for sphericity is not implemented. Finally, Goltz (1989) showed that the mass line approach can cause large errors if the lines are close to the station.

In recent years, developments were published to calculate tesseroids by numerical integration. These bodies represent a cube in a spherical coordinate system. This avoids overlaps and gaps of prisms as shown in Figure 3-3. Several authors introduced tesseroids for correction and modelling of gravity and gradient fields (Heck and Seitz, 2007, Grombein *et al.*, 2010, Uieda, 2010, Szwillus *et al.*, 2012). The gravity of a tesseroid can be calculated by solving the integral of the attraction of a cube in spherical coordinates Grombein *et al.* (2010):

$$g(r, \theta, \phi) = G \rho \int_{\phi_1}^{\phi_2} \int_{\theta_1}^{\theta_2} \int_{r_1}^{r_2} \frac{\Delta x \Delta y \Delta z}{l^3} \kappa dr' d\theta' d\phi' \quad (11)$$

where G is the gravitational constant, ρ is the density,

$$\Delta_x = r' * K_\theta$$

$$\Delta_y = r' \cos(\theta') \sin(\phi' - \phi)$$

$$\Delta_z = r' \cos\psi - r$$

$$l = \sqrt{r'^2 + r^2 - 2r'r\cos\psi}$$

$$\cos(\psi) = \sin\theta * \sin\theta' + \cos\theta * \cos\theta' * \cos(\phi' - \phi)$$

$$K_\theta = \cos\theta * \sin\theta' - \sin\theta * \cos\theta' * \cos(\phi' - \phi)$$

$$\kappa = r'^2 * \cos\theta'$$

θ is latitude, ϕ is longitude and r is radius.

This integral can only be solved by numerical integration (e.g. Gauss-Legendre Quadrature rule, (Asgharzadeh *et al.*, 2007)). Uieda (2010) showed that the solution of the integral is not stable if the computation point is close to the body. He claims, the distance between computation point and tesseroid has to be larger than the distance between tesseroids nodes. Therefore, calculations located very close (e.g. centimetre to meter distance) to the surface is very time consuming undertaken due to a very small grid spacing.

This brings me to end of this brief overview of the most common methods for topographic corrections. Today, there is no need to use station dependent methods like Hammer charts because calculations with prisms or tesseroids are easy to conduct with present day computers. However, any prism calculation has high computational costs which can be problematic for large scale surveys and large datasets. Furthermore, the prism approximation causes overlaps and gaps when considering sphericity due to rotation of the bodies. Recently, consideration of sphericity became important due to large investigation areas related to global coverage and availability of geophysical data. Tesseroids seem to be a good advancement of prism representations. But, numerical problems take place for calculations close to the topography. The new approach presented in this thesis will base on a calculation with polyhedrons. Modifications make it possible to consider sphericity of the earth. The algorithm is even stable close to the surface and calculates gravity gradients. The algorithm is explained in detail in chapter 3.2, together with the new correction method.

3.1.1 Terrain and Bouguer correction and complete mass correction

Traditionally, the procedure of calculating a full Bouguer correction (Bouguer plate + terrain correction) is split up in two steps. First, the terrain correction is calculated and applied to the data. Second, the gravity effect of a Bouguer slab is subtracted (Mikuška *et al.*, 2006). The terrain corrections are used to consider the deviations of topography from the Bouguer slab. Some requirements are important to consider a consistent correction:

- If a distinct correction area is defined, slab and terrain correction have to be calculated within the same area.
- If a spherical Bouguer slab is subtracted, the terrain correction has to be considered spherically.
- If a DTM is used, stations should be located on the surface of the DTM to avoid errors.

If an algorithm accounts for sphericity of terrain correction and is combined with a flat Bouguer slab, the result includes a systematic error. The masses of topography overlap with the Bouguer slab. If topographic corrections accounts for sphericity, a spherical Bouguer slab should always be used. Equation 7 shows, that the extent of such a Bouguer slab can be defined during calculation. If it equals to the extent of the topographic correction, the calculation is called consistent.

Finally, the station heights have to be located at the surface of the DTM. Global DTMs provide mean station heights over at least 90 m, so it is likely that station heights from terrestrial data do not fit to the surface of these DTMs (especially when measurements are located in narrow valleys surrounded by high topography). If a station is located above the DTM and a Bouguer slab is subtracted with a thickness from sea level up to the station height (in the two step approach), the mass is overestimated (the plate becomes thicker because the station lies above topography). The value of overestimation is approximately $0.1 * 10^{-5} \frac{m}{s^2} * \frac{1}{m}$ (with a rock density of 2670 kg/m³).

In all calculations of chapter 3, the corrections are conducted as a "complete mass correction". The algorithms calculate the whole volume of topography from sea level up to the surface. Therefore, all corrections are not affected by any of the previous described inconsistencies.

If stations are corrected with an external DTM, it has to be verified if station heights and DTM fit together. If this is not the case, different scenarios are possible to overcome this problem:

1.) If station height is expected to be correct, it should be included in the calculation. Müller (1999) suggested to include station heights in topographic correction and define a plateau with the station height 200 m around the station if it is located below the DTM. This was done to avoid large correction values due to steep topography flanks close to the station. But, if stations are systematically below the DTM surface, stations are located in artificial "valleys" which lead to incorrect topographic correction. Therefore, if station heights are included in the DTM, the

differences to the DTM have to be analysed carefully. If station heights have to be used, it is better to include a self derived DTM to avoid artificial structures.

2.) If the station height is not reliable, a new height value should be extracted from the DTM. This ensures that the effect of topography is estimated correctly.

In general, if no self derived DTM is available and stations have a large misfit from the DTM it is recommended to extract a new station height from the DTM. The DTM represents the best known representation of the topographic surface. If the DTM is modified by synthetic values to include measured station heights, artificial structures can distort the results.

For all calculations in chapter 3, station heights were analysed and corrected with DTM heights if necessary.

3.1.2 Distant topography and limiting radius

Bouguer correction with topographic correction is often limited to a distance of 166.67 km to the station. This distance coincides with the Hayford O2 zone, defined by Hayford and Bowie (1912). This radius is not chosen completely arbitrary. Talwani (1998) showed that the difference of a spherical and plain Bouguer plate is smallest, if a limiting radius of 166.67 km is chosen. Thus, it is still a standard correction radius. The choice of a correct radius is discussed by several authors (LaFehr, 1991, Talwani, 1998, Mikuška *et al.*, 2006). Mikuška *et al.* (2006) investigated the distant topographic effect (beyond 166,67 km, corresponding to an angle of aperture of 1.5°). They concluded that in reasonable flat areas and local surveys the limit of the radius is appropriate. This is also concluded by Talwani (1998) and LaFehr (1998). For global scale surveys and for local surveys in areas of rugged topography, a calculation of the distant topographic effect can be useful (cf. (LaFehr, 1991). The conclusions about the distant topographic effect from different publications are rather contradictory. The global coverage of height data, larger investigation areas (due to satellite missions) and faster computers make it possible to account for distant topography. But, there is no rule how accurate distant topography has to be taken into account. In an active margin environment (like the Andes) deep sea trenches has to be regarded as "rugged terrain", too. Thus, apart from rugged onshore terrain, corrections in coastal areas can be complicated. An automatic approach to decide which resolution should be taken in a distinct environment would avoid any pre-assumptions (by choosing a correction radius or a specific DTM resolution) from the user, but still save computation time in flat areas where only a coarse resolution is necessary. In chapter 3.2.3 a new method is explained which is capable to conduct an automatic analysis of gravity terrain effects.

3.2 New approach for consistent topographic correction

The scope of this part of the thesis is to develop a new reduction algorithm which reduces geometrical approximations and pre-assumptions significantly. Several features have to be included:

- Use of polyhedrons to represent topography,
- consideration of Earth's sphericity,
- use of geographical coordinates,
- automatic choice of DTM resolution,
- handling of large datasets,
- correction of gravity gradients.

Polyhedrons and triangulated surfaces of topography are the best representation of geometry. Prisms, tesseroids etc. have a fixed size for each compartment, which can lead to insufficient approximations (cf. Figure 3-5). The triangulation of topography preserves the point wise observation of the DTMs. In addition, global DTMs are always provided in geographical coordinates. The direct use of these datasets avoid any projection (like UTM) which can lead to distortion of DTMs.

The automatic choice of resolution introduces a new idea, how to deal with distant topography and redundant data information. The new approach does not change DTM resolution depended on the distance to the station but depended on the gravity influence on the station. This is explained in detail in chapter 3.2.3. Topography is globally available with a 30' (900 m) resolution (onshore even 3''(90 m) to 1'' (30 m)). The calculation of topographic corrections with full resolution over a large area could involve very long calculation times. Thus, the efficient handling of large datasets is very important.

Since a couple of years, ESA's new satellite GOCE provides directly measured global gradients for the first time. A couple of authors already showed that the availability of such data increases the use of gravity gradients for investigation of the lithosphere. However, there is a strong need for a careful topographic correction of gravity gradients to interpret lithospheric structures. The new method is also capable to calculate the gravity gradients of topography.

The calculation of the gravity and gradients of topography is adopted from the algorithm described in Götze and Lahmeyer (1988). The volume integral which has to be solved for gravity calculation can be transformed into a surface integral by applying the Gauss's theorem (Götze, 1976):

$$g_i = G\rho \iint_S \cos(\vec{n}_s, \vec{e}_i) \frac{1}{R} dS \quad (12)$$

where G is the gravitational constant, ρ is the density,

S is the surface of the polyhedron,

R is the distance of dS to the observation point

$$i = 1, 2, 3 = x, y, z$$

and $\cos(\vec{n}_s, \vec{e}_i)$ is one component (x,y,z component) of the normal vector of S.

If a polyhedron is triangulated the integral can be calculated like this:

$$g_i = G\rho \sum_{k=1}^m [\cos(\vec{n}_k, \vec{e}_i) \iint_{S_k} \frac{1}{R} dS_k] \quad (13)$$

By applying the Gauss theorem for surfaces the surface integral can be transformed into a line integral. This results into a equation which sums up the calculations over each edge of a triangle:

$$g_i = \rho G \sum_{j=1}^m \cos(n_j, e_j) \left[\sum_{k=1}^3 \text{sign}(d_{jk}) d_{jk} LN_{jk} + D_j \sum_{k=1}^3 \text{sign}(d_{jk}) ARC_{jk} \right] \quad (14)$$

where (see Figure 3-4 for further description)

$\text{sign}(d_{jk})$ is positive or negative whether the normal vector
of the triangle points to P or not

$$LN_{jk} = \ln\left(\frac{a_{jk} + R_{jka}}{b_{jk} + R_{jkb}}\right)$$

d_{jk} is the distance between P_j^* and P_{jk}^{**}

$$ARC_{jk} = \tan^{-1}\left(\frac{r_{jka}^2 + a_{jk} * R_{jka}}{d_{js} * D_j}\right) - \tan^{-1}\left(\frac{r_{jkb}^2 + b_{jk} * R_{jkb}}{d_{jk} * D_j}\right) = \tan^{-1}\left(\frac{A - B}{1 + AB}\right) + \delta_2\pi$$

$$R_{jka} = \sqrt{D_j^2 + d_{jk}^2 + a_{jk}^2},$$

$$R_{jkb} = \sqrt{D_j^2 + d_{jk}^2 + b_{jk}^2},$$

$$r_{jka}^2 = a_{jk}^2 + d_{jk}^2,$$

$$r_{jkb}^2 = b_{jk}^2 + d_{jk}^2,$$

$$\delta_2 = \begin{pmatrix} 0 \\ \pm 1 \end{pmatrix} \text{ if } \begin{pmatrix} AB > -1 \\ AB < -1 \text{ and } B \leq 0 \end{pmatrix}$$

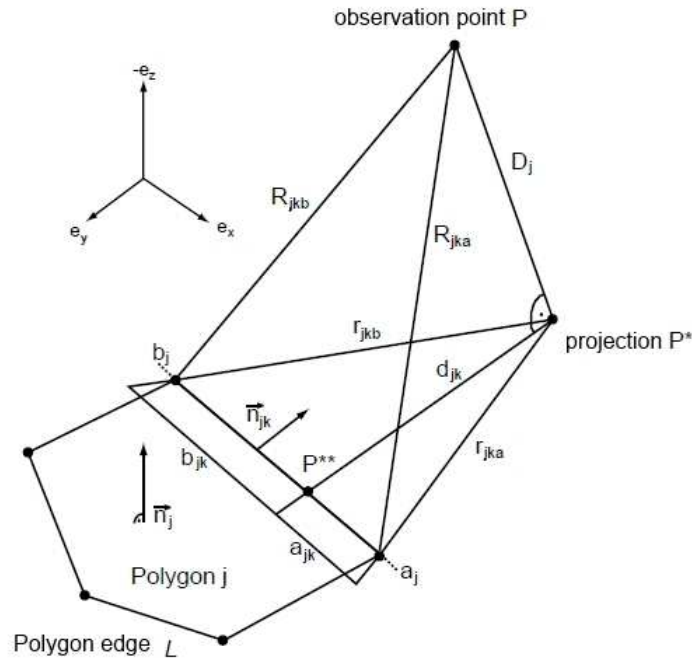


Figure 3-4: Original Figure from Götze (1976). It gives an overview over the variables used in equation 14.

The calculation of the gravity effect, the potential and the 5 independent gradients for one triangle includes the evaluation of the natural logarithm and the inverse tangent three times. An example is necessary to compare the computational costs of prisms and polyhedrons. If we assume a correction with the standard correction radius of 167 km for a small survey we need a DTM grid of about 200 x 200 km. A DTM grid of 1 km resolution comprises 40000 grid nodes. For the triangulation of such a grid, 318400 triangles are constructed (see explanation of triangulation in chapter 3.2.1). This results in 955200 evaluations of the natural logarithm and the inverse tangent. A calculation with prisms involves 40000 evaluations of equation 9. This results in 488000 evaluations of the natural logarithm and 240000 evaluations of the inverse tangent. Therefore, if the DTM is only a regular grid, the computational cost is higher for the triangulation than for a prism representation (if only g_z has to be calculated). However, the polyhedron calculation provides some advantages:

- The topography can be represented by one triangulated body which avoids overlapping and gaps of bodies. This results in a better representation of geometry.
- Complex structures can be represented by a polyhedron with irregular data points. For the same representation with prisms, the geometry has to be discretised which can end up in redundant data and even more calculations.
- Gradients and all other components of the gravity vector can be calculated easily.

The polyhedron algorithm (Equation 14) needs cartesian coordinates as input because the triangles have to be plain. The geographical coordinates can be transformed into a earth centred coordinate system to fit that needs. The new coordinate system is three-dimensional and right-angled with coordinates x, y, z .

The conversion from geographical to Cartesian coordinates has to be conducted before calculation. The transformation avoids distortion of the topography. The transformation is calculated for each triangle point and each computational point:

$$\begin{aligned}x &= r * \cos \theta * \cos \phi \\y &= r * \cos \theta * \sin \phi \\z &= r * \sin \theta\end{aligned}\tag{15}$$

where r is the earth radius, θ and ϕ are the latitude and longitude.

The resulting surface accounts for sphericity and is consistent. In general, the local coordinate system of the station do not coincide with the global coordinate system because it points radially to the earth's mass centre. Therefore, the resulting calculations have to be rotated in the local coordinate system of the station. This has only been done once for each station, if all calculations are finished. The rotation can be conducted by calculating these equations:

$$\begin{aligned}g_x &= \vec{g}_{global} \cdot \begin{pmatrix} -\sin(\theta) * \cos(\phi) \\ -\sin(\theta) * \sin(\phi) \\ \cos(\theta) \end{pmatrix} \\g_y &= \vec{g}_{global} \cdot \begin{pmatrix} -\sin(\phi) \\ \cos(\phi) \\ 0 \end{pmatrix} \\g_z &= \vec{g}_{global} \cdot \begin{pmatrix} \cos(\theta) * \cos(\phi) \\ \cos(\theta) * \sin(\phi) \\ \sin(\theta) \end{pmatrix}\end{aligned}\tag{16}$$

where ϕ, θ are the longitude and latitude of the station,

and \vec{g}_{global} is the full gravity vector in the global coordinate system

For gradients the whole gradient tensor has to be rotated in the local coordinate system of the station:

$$G_{local} = R * G_{global} * R^{-1}\tag{17}$$

where R is the rotation matrix which contains the spherical uni vectors of the station (see equation 16) and G is the gradient tensor.

The transformation into the earth centred coordinate system and the rotation makes it possible to calculate the gravity effect of a polyhedron on a sphere with direct use of geographical coordinates.

3.2.1 Triangulation of data

Correct gravity calculation with the polyhedron algorithm asks for a closed and consistent triangulation of the polyhedron surface. Delaunay triangulation is a well known procedure for this purpose (Delaunay, 1934). In general, topography is available as a regular grid. Here, triangulation is trivial and faster than Delaunay triangulation because it just involves database queries without any further calculations. Thus, a very efficient triangulation of large grids can be conducted in a minimum of time and memory consumption. This triangulation of DTMs was implemented in the framework of this study.

The triangulation is done on the fly and not saved in memory. It is conducted serial (and not iteratively), so computational cost of this method increases only linear with the number of points. This makes it possible to handle large datasets (e.g. billion of grid nodes). The algorithm loads 4 adjacent points (2 in x- and 2 in y-direction). A 5th point in the middle will be inserted with mean elevation of the edge points. Those 5 points will be triangulated by four triangles (see Figure 3-5A and B). The fifth point avoids a predominant strike direction of the triangles. Mundry (1970) showed that a constant strike direction of the triangles can cause artificial geometries.. For example, the shape of a triangulated surface changes if the predominant strike direction is parallel or perpendicular to an elongated structure in the DTM.

Coastal areas and additional data points from other sources (e.g. station heights) have to be handled separately because the triangulation of irregular points is not trivial. At coastal areas the water body and the landmass have to be separated and triangulated consistently. The polyhedron algorithm has to distinguish between both because of different densities of the bodies.

At the coast the DTM heights change from positive to negative values. Triangles connecting positive and negative heights intersect with zero level (sea level). This has to be avoided to separate the water and landmass body. Therefore, additional points at zero level, which represent the coastline, will be calculated (Figure 3-5C). Then, grid points and intersection points are triangulated by Delaunay triangulation. This can also be used to include irregular station heights in the triangulation (Figure 3-5C).

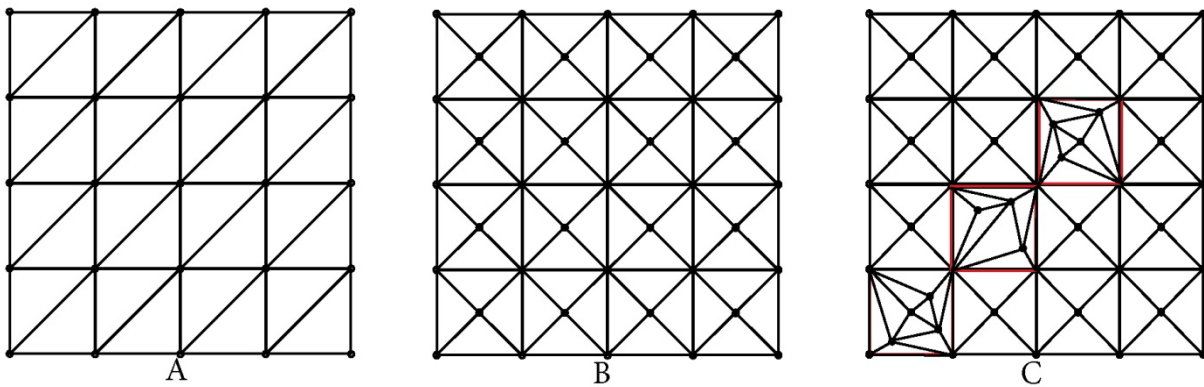


Figure 3-5: This Figure shows different triangulation schemes. (A) shows an primitive manual triangulation of a grid which uses the nodes only. The strike direction of the triangles can cause artificial structures. (B) shows a manual triangulation with an additional point in the middle to avoid artificial structures. (C) shows a combination of a Delaunay triangulation of irregular points combined with the simple grid triangulation of (B).

Representing topography by triangulated polyhedrons rather than simple bodies (e.g. prisms) has advantages in coastal areas. In these areas, the coastline defines a border between two bodies (water and rock) with different correction densities. Figure 3-6 shows a DTM represented by prisms and by a triangulated surface. The fixed size of prisms causes overlaps at the coastline which are not present in the triangulation. Stations close to the coastline can be affected because the border is not approximated correctly.

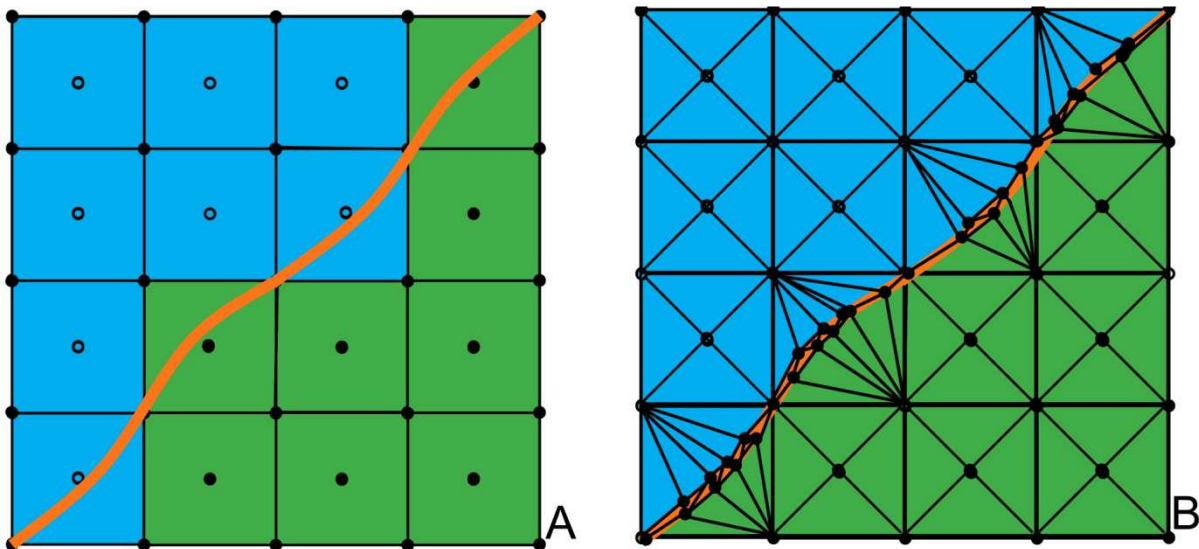


Figure 3-6: Grid at a coastal area represented by prisms (A) and triangles (B). The coastline is orange. Blue colour represents bodies where correction is calculated with water density, green colour represents rock density. In (A) the centre point of the prism is used to decide what density is represented by the prism. The triangulation allows a fine representation of the coastline.

Figure 3-7 shows the result of a synthetic example located at the Andean coastline. First, stations ($n = 1200$) were defined which are shifted by 1 km to the East of the coastline. Then, topographic correction were calculated with GR3 (prism representation) and the polyhedron algorithm (presented in detail in chapter 3.2.4). Figure 3-7a exhibits only stations with deviations higher than $5 * 10^{-5} \frac{m}{s^2}$. The colour describes the differences between the results of the two algorithms. Most differences are observed where the coastline features sudden changes. In particular, in at $\sim 42^\circ S$ at a narrow valley, the deviations are largest. Figure 3-7b shows the resulting histogram of the differences from both calculations. Almost 85 % of the calculated points deviate less than $4 * 10^{-5} \frac{m}{s^2}$. Approximately 15% of the stations feature higher deviations with a maximum of $23 * 10^{-5} \frac{m}{s^2}$. This test bed demonstrates that large differences can occur along coastline. It is mandatory to represent the border between two bodies with different densities as accurate as possible. The results imply a more accurate representation of geometry by polyhedrons than by prisms.

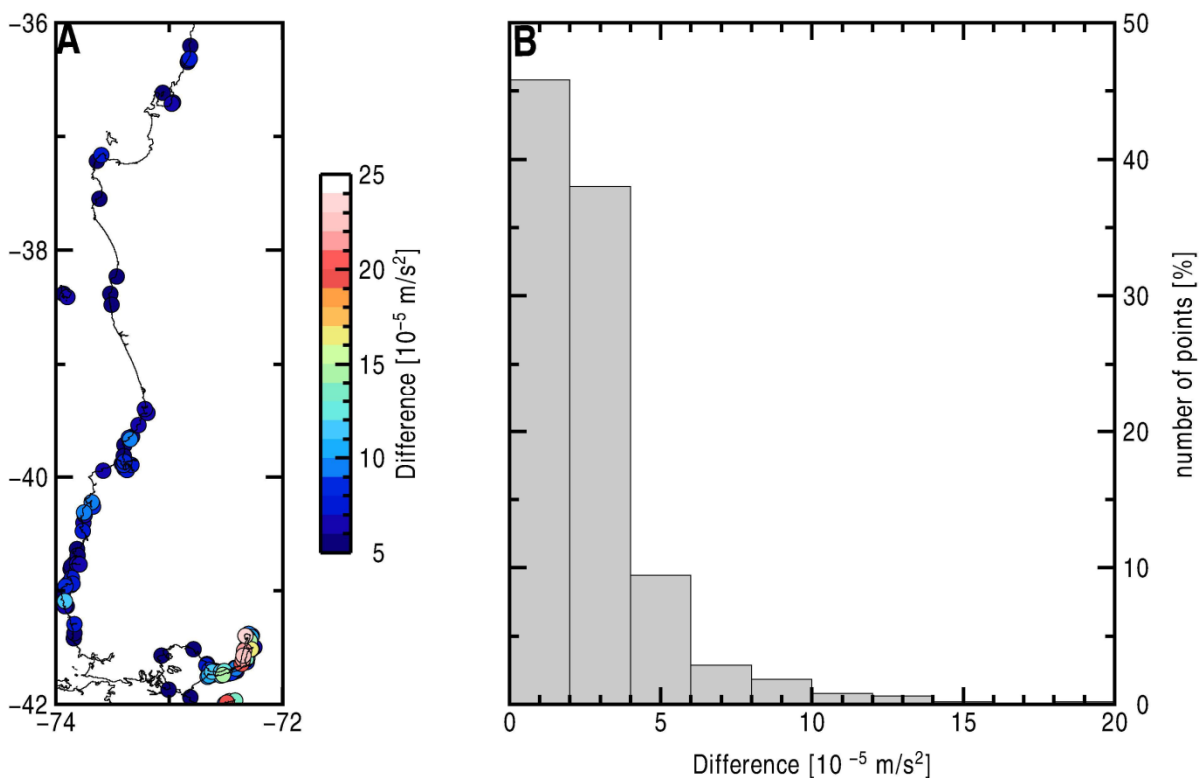


Figure 3-7: Differences of topographic mass correction calculated at the Chilean coastline. The differences are between the algorithms using prisms and polyhedrons. (A) portrays stations with deviations larger than $5 * 10^{-5} \frac{m}{s^2}$. (B) histogram over all stations. Corrections were calculated of 1200 stations which are parallel to the coastline and shifted by 1 km to the East..

3.2.2 Availability of Topography

Old publications (before the 90s) describe an urgent of digitising contour maps to derive mean heights for a desired area. In 2000, the shuttle radar topography mission (SRTM) was started to measure the global topography from the space. The data were processed and build a global topography grid (Farr *et al.*, 2007). Onshore, resolutions of 1" (30 m) to 3" (90 m) are available. 1" is only available in particular areas (e.g. North America). The SRTM mission was designed to measure topography with high precision, so no offshore data were available. The original SRTM is not consistent over the whole globe. The missions covered the area between latitudes 60° N and 58° S. The poles are not covered by the satellites. Furthermore, the original data comprises voids. These are caused by steep slopes (e.g. at mountains) which faces away from the radar and by smooth areas like lakes, where no energy was scattered back to the radar (Hall *et al.*, 2005). The voids were filled by interpolating and filling with external data (Grohman *et al.*, 2006, Hoffmann and Walter, 2006). SRTM does not always map the real surface. Dense vegetation or buildings are considered as ground surface. The global accuracy of the SRTM dataset is ± 16 m. However, regional studies comparing SRTM with ground truth showed, that large differences (hundreds of meters) to ground data can occur in some regions (Smith and Sandwell, 2003, Denker, 2004). Therefore, the original SRTM data cannot be used directly for topographic correction. Several projects provide processed SRTM data where voids are filled up with other sources to provide a consistent global elevation model (e.g. (Becker *et al.*, 2009, Berry *et al.*, 2008, Jarvis *et al.*, 2008). For this thesis ACE2 (Berry *et al.*, 2008) was chosen as data input. This data product includes reprocessed SRTM heights, filled up and corrected with altimeter data from multiple satellite altimeters. It provides full coverage of data onshore with 3", coastal areas are covered with a 9" grid and the global resolution (including oceans) is 30". The accuracy of data varies and depends on available additional data. The range of accuracy is between ± 16 m to ± 1 m. All data is carried out with a data source and a quality matrix, which makes it easy to assess the data quality in the chosen area. The height data is corrected for vegetation and clouds. Data is available in 15° x 15° tiles saved in a binary format and compressed to an archive. The data is easy to handle, the compressed binary format makes it easy to download and read. ACE2 provides consistent processed data in different resolutions which can be used directly for topographic corrections.

3.2.3 Adaptive resampling of topography

Ehrismann and Lettau (1971) developed a station independent resampling of topography for the calculation of the topographic correction. The station independent system avoids redundant averaging of DTM heights. Grids of different resolutions are only calculated once and not separately for each station. This keeps computational costs low. The decision, which grid was used to calculate the gravity effect, depends on the distance to the station. However, gravity at an observation point is not only dependent on the distance to a mass but also on its volume. Therefore, resampling should also consider the geometry of topography.

If only distance to the station is considered, flat and smooth topography close to the station would be represented with a high grid resolution which can cause redundant calculations. On the other hand distant rugged terrain would be represented with coarse resolution which does not represent the geometry correctly. The test in chapter 3.4 shows that distant terrain can have an influence on the relative gravity differences between stations in an area (up to $6 * 10^{-5} \frac{m}{s^2}$). Therefore, in the framework of this thesis, a new method of DTM resampling was developed. In principle, the algorithm changes the grid resolution as a function of the gravity influence on the station. In this case geometry and distance are calculated correctly. In a first step, a new data structure is constructed based on the DTM. This structure follows the concept of a quad tree. The quad tree structure is shown in Figure 3-8. The lowest level of the tree corresponds to the size of original DTM. The next level is resampled to a grid with only a quarter of nodes. This is conducted until a level only contains one point. This point is the mean elevation over the whole area.

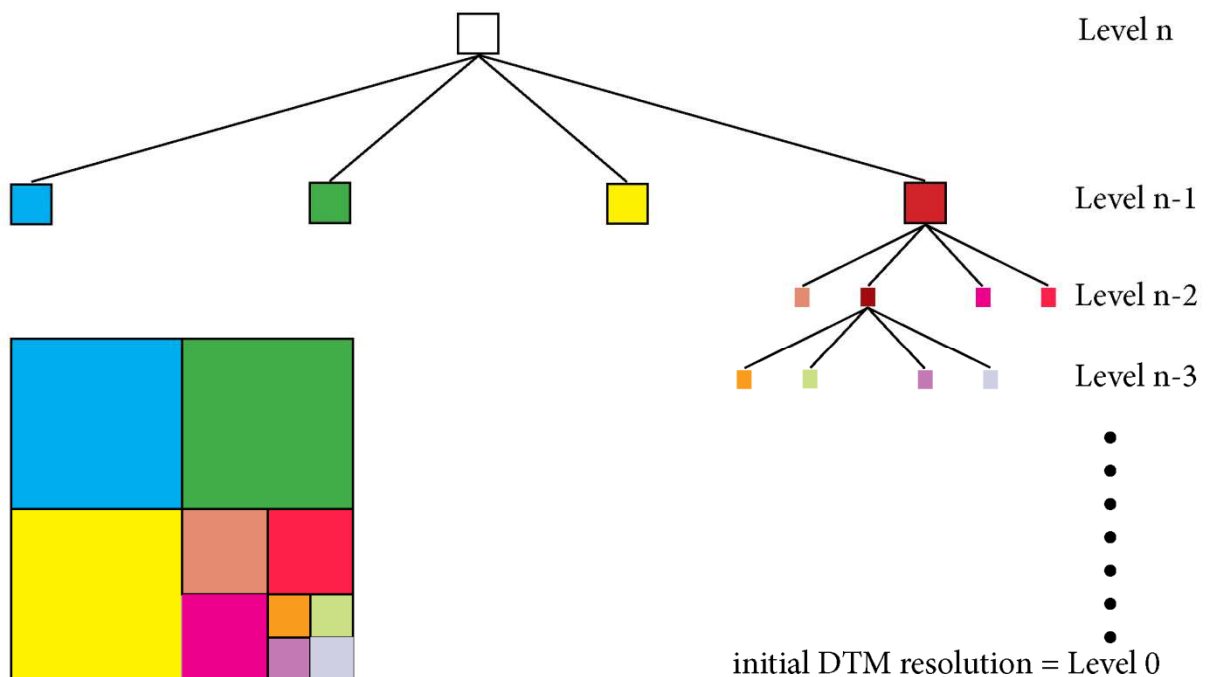


Figure 3-8: The principle quad tree representation. On top the tree representation is shown. Each node has 4 child (colours indicate height information) in the next level until the resolution from the initial DTM is reached. Bottom left shows the map representation of a quad tree. The quad tree can be used easily to represent a map with different resolutions.

The setup of a quad tree has to be done once before the calculation of the topographic corrections. It is necessary to calculate new mean values for each level. The memory consumption increases 33 % compared to the initial size of the DTM.

Figure 3-9 shows the flow chart of the iterative adaptive calculation. First, for each station the gravity response of level n and $n-1$ will be calculated. If the difference between both calculations is less than a user defined threshold, the calculation stops and the result of the $n-1$ level will be taken for correction. If the difference is higher, the correction of the next level will be calculated and compared to the result of the previous lower resolution. This is done, until the difference is smaller than a user given threshold. It is the only value, the user has to define. A good choice for this value is the given accuracy of the measured gravity data.

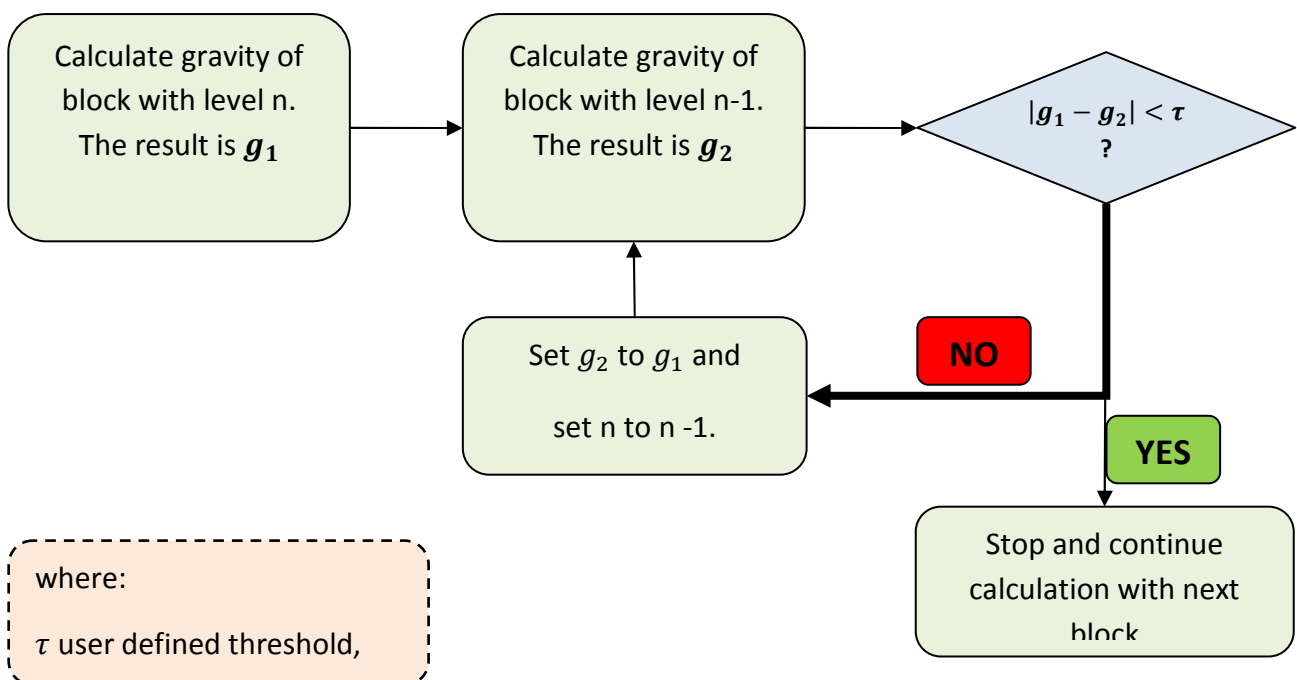


Figure 3-9: The flow chart of adaptive gravity calculation. First, the gravity response of a block is calculated with the lowest resolution and the next higher resolution. If the difference of the results is smaller than a given tolerance, the algorithm stops and calculate the next area (cf. Figure 3-11). If the difference is higher, the next higher resolution will be considered for calculation and compared to the previous result.

The polyhedron approach bases on plain triangles representing the spherical shaped topographic surface. Thus, the topography has to be discretised with points and a specific spacing to represent a spherical surface. If the spacing is too large, secants occur when points are connected.(e.g. (Kirchner *et al.*, 1996) compared the analytical calculated gravity of a homogenous spherical earth ($g_{analytical} = 9.8198738 \frac{m}{s^2}$) and compared it to a discretised calculation with polyhedrons. He calculated a deviation of 0.03 % ($g_{calc} = 9.81648 \frac{m}{s^2}$) with a grid spacing of 0.5° and concluded

that smaller grid spacing minimise the misfit. The topographic corrections in this thesis do not extend over the whole earth, but only calculate a cut-out. Tests of the adaptive approach showed, that the automatic resampling does not work satisfying with the polyhedron algorithm if the grid resolution is too low. Therefore, for all calculation the lowest grid resolution was fixed to 0.16° (18.52 km). This limit provided the best results of the adaptive calculation. Figure 3-10 shows a topographic correction performed with tesseroids (Szwilius, pers. comm. and (Szwilius *et al.*, 2012)). Tesseroids are spherically shaped to the size of the compartments is not limited to avoid secants. The black thin lines show the size of the tesseroids needed to correct the gravity at the station (at 85°E and 34°N). It can be seen, that topography West to the station is approximated roughly, but high mountains in the North and South are resolved with fine resolution.

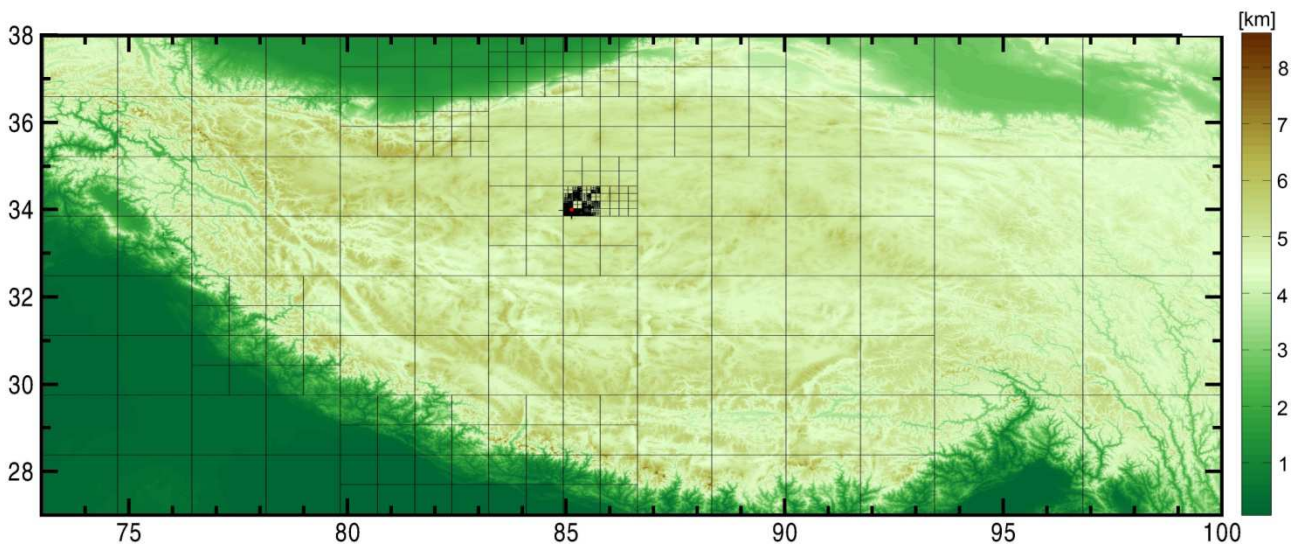


Figure 3-10: Adaptive approach implemented with tesseroids (Szwilius, pers. comm.). The spherical shaped tesseroids allow large compartment size. The Tibetan plateau is approximated with large compartments; the Himalayan mountain range features smaller grid sizes.

The window starts at the lower left corner of the grid and comprises 4 points of the lowest grid. The gravitational attraction of this block is calculated as shown in Figure 3-11. If the calculation is finished for the first block, the window moves upwards and the calculation is done for the adjacent block. This is performed until the window covered the whole grid and over all stations. Figure 3-11 shows the principle of the calculation with the moving window.

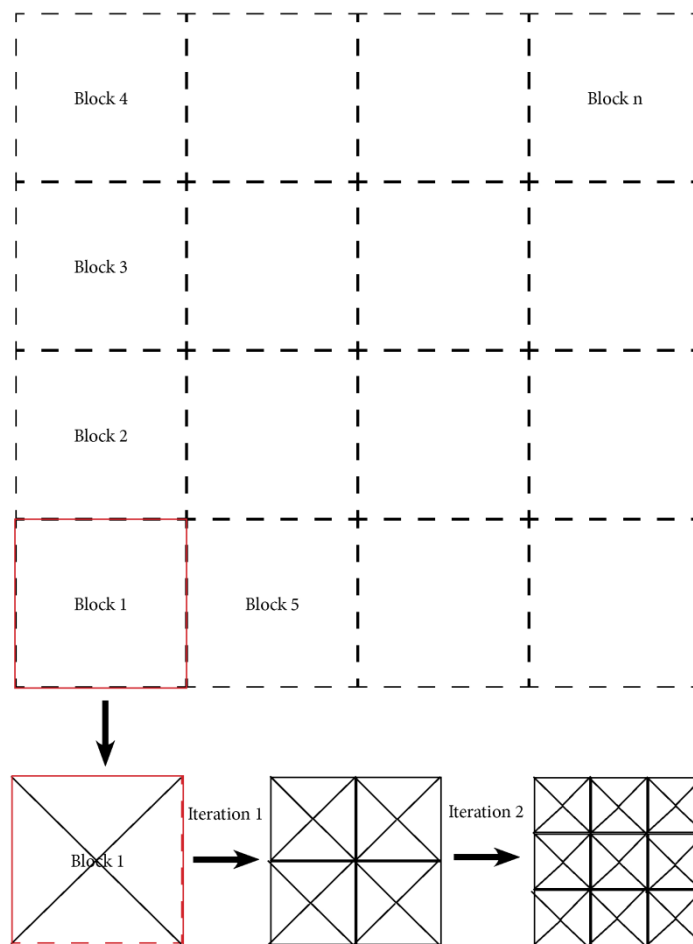


Figure 3-11: Here, the adaptive calculation with polyhedrons is demonstrated. A moving window calculates each block separately. The extent of an initial block is defined by the lowest grid resolution (which is predefined). The block will be refined completely by a deeper quad tree level (Iteration 1) and is compared to the first calculation. If the difference is too high, next iteration will be done until the difference is small enough.

The adaptive calculation leads to a massive speed up. Tests show, that the results are very close to calculations with a high resolution grid (see Table 3-1). Furthermore, the pre-assumptions the user has to define are simple and understandable. In addition, this approach is also very robust for large scale or even global DTM grids. It is possible to include a high resolution global grid for a topographic correction. The algorithm itself reduces the grid resolution for distant areas automatically if the influence is small. This is very useful if satellite or airborne gravity data is used. First, such data is often used for regional scale studies. Second, if the stations are in flight or orbit height, the influence of topography decreases $\frac{1}{r^2}$. This is also regarded by the algorithm which eases and speeds up the correction of such data.

The new method is built up of a station dependent and independent algorithm. The resampling and triangulation of topography has to be estimated for each station. However, the averaging of DTM heights is performed once, so no redundant calculations are performed. Table 3-1 shows a comparison between the adaptive and normal polyhedron correction. The deviations are small and in desired and acceptable range (about 1 per mill of the correction value). The calculation time for the 90 m DTM is shortened by a factor 250 and the same for 360 m resolution. For a 900 m

spaced DTM, the time still shortened by factor 50. The adaptive algorithm always has to calculate at least the lowest (level n) and the next higher resolution (n-1). So, the predefined resolution limit of 18.52 km (0.1666°) for level n of the quad tree leads to a lowest resolution for topographic correction of 9.3 km (level n-1). The savings in calculation time compared to the calculation with the full resolution grid are best, if the initial grid has a high resolution. If a correction is conducted with a grid spacing of 18.52 km (highest resolution), the algorithm cannot resample the DTM anymore. In this case, the computation time of the adaptive approach would be even longer than the sole correction. The results are satisfying and confirm that the quad tree is a promising new method for reducing geometry information of the polyhedron surface. It eases the topographic correction for the user, because only a desired accuracy has to be defined. Furthermore, it is robust for large or even global scale calculations (see chapter 3.4 and 3.5 and Table 3-1).

Longitude	Latitude	height [m]	Difference to polyhedron correction with full grid [$10^{-5} \frac{m}{s^2}$]		
			90 m	360 m	900 m
87	32	6305	0.58	0.58	0.73
94	30	5730	0.59	0.59	0.55
85	32	6120	0.56	0.55	0.71
87	29	6080	0.41	0.42	0.50
96	33	5140	0.97	0.97	1.16
85	34	5040	0.67	0.66	0.87
95	32	5335	0.81	0.81	0.97
77	33	6464	0.41	0.40	0.55
78	35	5699	0.61	0.62	0.80
Runtime (full grid) [min]			603	85	9.8
Runtime adaptive grid [min]			2.4	0.4	0.2

Table 3-1: Comparison between the full grid correction (without resampling) and the adaptive approach. The columns show calculation for different resolutions (for the adaptive approach this means the highest resolution). The deviations to the full grid calculation are below $1 * 10^{-5} \frac{m}{s^2}$ (except for one value). This shows that the adaptive calculation is as accurate as the normal calculation with a massive speed up. The mean correction value is $\sim 565 * 10^{-5} \frac{m}{s^2}$, so deviations are less than 1 per mill).

3.2.4 TriTop

TriTop is a Java based software package which was developed in the course of this thesis to provide the described new features to other researchers. The JAVA implementation provides a software platform independent of operating systems. The program has a graphical user interface (GUI, Figure 3-12) which eases the use.

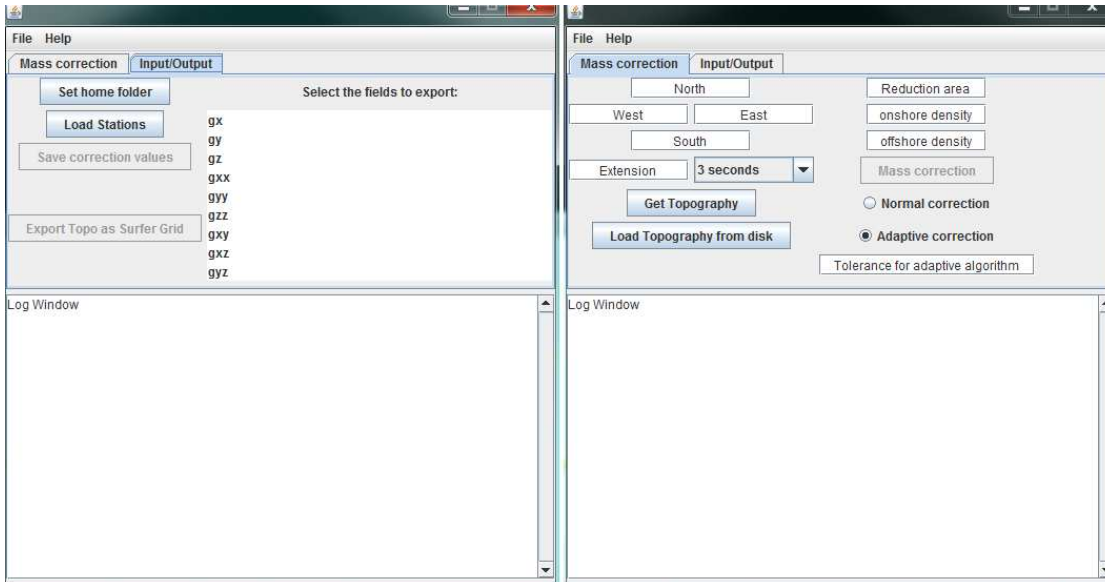


Figure 3-12: Screenshot of TriTop. It provides a simple GUI which makes it possible to download topography grids automatically and calculate gravity (gradient) correction of the topographic mass.

The program needs two input files. Station coordinates (longitude, latitude, height) and a topography grid in geographical coordinates. The software is capable to download the necessary topography grid for a desired area automatically. It downloads data from the ACE2 server (<http://tethys.eaprs.cse.dmu.ac.uk/ACE2/shared/webdownload>) and crops the tiles down to the given limits. The user can choose between 3 grid resolutions as provided by the ACE2 consortium: 3", 9" and 5'. If the highest resolution is not available everywhere in the chosen area, the program downloads also a coarser grid and merges both datasets. So, coastal areas can be downloaded as one consistent grid with a resolution of 3" onshore and 30" offshore, respectively. The final topography file does not include any dummy values. It is also possible to import a self-derived topography grid. If all input data is available, the mass correction can be started. If the normal correction method is chosen a limiting bounding box (reduction area) around each station can be defined. If the adaptive correction is selected, only a tolerance can be defined (see Figure 3-12).

During mass correction, the progress and all messages to the user are shown in the log window. If the calculation of mass corrections is finished all desired values can be exported. Before export, the user has to define the onshore and offshore density. The correction values of the selected fields are exported as a simple text format file. If the topography grid was downloaded it is automatically saved as an Esri grid (ARC/INFO ASCII GRID). It can also be exported as an ASCII Golden Software Surfer grid. Finally, the software provides a complete and easy to use toolbox for topographic correction.

3.3 Test bed "Himalaya": Comparison of Algorithms and DTMs

For a first test, the area around the Himalayan mountain range, including the Tibetan plateau, the Kunlun mountain range, parts of the Taklamakan desert and the north of India including alluvial planes South of the Himalaya. Here, heights are in the range of 0 to about 8900 m. In an early phase of the algorithm development, it was impossible to include offshore areas in the calculation process. Thus, it was also necessary to define an area *without oceans*. In addition, this test bed was ideal to investigate distant terrain effects because high mountains extend over a large area. Very steep height gradients as well as the Tibetan Plateau (see Figure 3-13) are located here which makes it possible to compare different station environments in the same area.

Selected algorithms for topographic correction were tested and compared against the TriTop results. The tests should answer the following questions:

- Are the results of the different algorithms similar?
- What is the effect on the results if different DTM resolutions are used?
- What resolution of DTM should be chosen?
- What is the difference in terms of runtime?

The "test DTM" spans an area from 73° E to 100° E and 27° N to 38° N. Different grid spacing were chosen to investigate the effect of resolution on the results: 3" (90 m, highest resolution), 12" (360 m, high resolution, available in coastal areas), 30" (1 km, global availability) and 5' (10 km, equals the grid spacing of global gravity model EGM2008). The following algorithms were tested:

- GR3 (prisms, (Ehrismann and Lettau, 1971),
- FFT (Sideris, 1984),
- tesseroids (Szwilius *et al.*, 2012),
- polyhedron representation.

9 stations were selected which are located in different topographic environments (refer to Figure 3-13). The stations were selected to perform calculations in different topographic environments. Station 1 and 3 in the South of Tibet are located close to a valley. Common station locations in mountainous areas are along valleys where roads exist. Station 4 and 8 are located in the Himalayan mountain range, to discuss stations close to high topography. Station 6 is located in the Tibetan plateau to discuss a station in a reasonable flat terrain but surrounded by rugged terrain. Station 9 is also located on a plateau but closer to high mountains. Stations 2,5 and 7 are located in an area of complex terrain due to alluvial planes in this area. The height of nearby mountains is less than for the stations 4 and 8. The stations were selected to cover those different preconditions and discuss the differences.

The shape of topography changes for each DTM resolution. Therefore, the surface height of a certain point changes with the grid resolution. The test stations are defined above all DTMs to make sure that the stations are never below topography. The station height is constant for all calculations. First, all calculations are conducted with the full topography grid without any limiting radius around the station or an adaptive approach. The correction density was set to 2670 kg/m^3 .

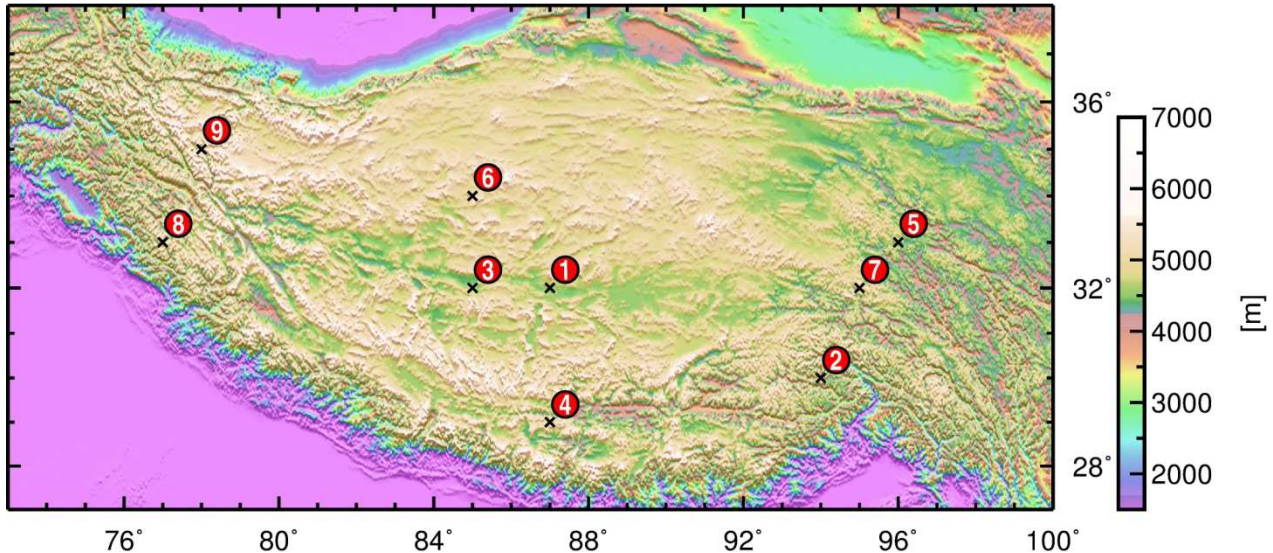


Figure 3-13: Area of the test bed, including the central Asian mountain ranges, Tibet and lowlands in the north of India. 9 selected stations in different topographic environments are numbered (red circles). Those stations were used for several test calculations of topographic correction algorithms.

3.3.1 Differences between algorithms

Figure 3-14 gives an overview about the results for the first benchmark. It shows the difference between the TriTop calculation and the other algorithms for different grid resolutions. For each grid resolution the results from the TriTop correction were subtracted from the results of other algorithms. Except for FFT, all algorithms perform quite similar independent from the chosen grid resolution. FFT features large deviations. This is caused by the mass line approximation of the prisms which can cause large errors close to the station. Corrections with prisms (GR3) and tesseroids deviate slightly for higher grid resolutions. The coarser grid cause larger element bodies which leads to a worse approximation of the surface (compare to gaps in Figure 3-3). However, for all grid resolutions, the algorithms calculate similar correction values. The small deviations between the polyhedron and prism representation for high grid resolutions prove the statement of Ehrismann (1972) that the prism approximation is appropriate if the elements are small.

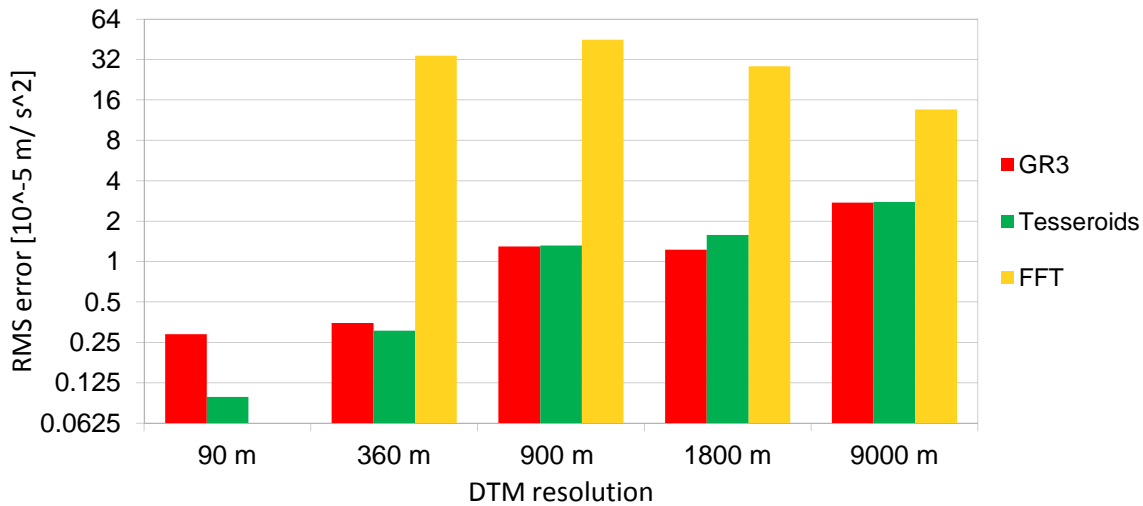


Figure 3-14: RMS error of selected algorithms to the polyhedron calculations. Each grid resolution is regarded separately. GR3 and Tesseroids feature only small differences over all grid resolutions. The differences increase from ~ 0 to $2.5 \cdot 10^{-5} \frac{m}{s^2}$. Increasing grid resolution causes large element bodies which causes coarser approximation. Therefore, the RMS increases for higher grid resolution. FFT always provides large deviations.

3.3.2 Benchmark for different resolutions

In a second step, the polyhedral mass correction with a 90 m DTM were chosen as a reference. Table 3-2 shows the difference between the calculations (different algorithms and grid resolutions) from the reference. This comparison makes it possible to interpret the deviations caused by the choice of a specific initial grid resolution. Figure 3-15 shows a bar plot of the RMS error. The RMS error almost equals for the algorithms GR3, TriTop and tesseroids for the different calculations. The increasing RMS error is caused by a coarse grid used for the correction. This shows that the choice of the grid resolution influences the correction results (up to $42 \cdot 10^{-5} \frac{m}{s^2}$ RMS error).

Resolution	Algorithm	90 m	360 m	900 m	1.8 km	9.3 km
Mean deviation [$10^{-5} \frac{m}{s^2}$]	polyhedron	/	2.63	-0.68	-10.93	-13.98
	GR3	-0.27	2.55	-0.33	-11.20	-13.64
	Tesseroids	0.15	1.71	1.14	-8.30	-7.49
	FFT	n/a	-30.59	-14.53	-16.77	22.39
RMS [$10^{-5} \frac{m}{s^2}$]	polyhedron	/	6.91	10.69	27.57	42.72
	GR3	0.29	6.98	10.57	28.54	42.19
	Tesseroids	0.098	7.05	10.56	28.40	42.17
	FFT	n/a	35.02	48.94	32.05	48.34
Minimum deviation [$10^{-5} \frac{m}{s^2}$]	polyhedron	/	-2.32	-25.30	-73.97	-72.19
	GR3	-0.46	-1.79	-24.34	-76.61	-73.96
	Tesseroids	-0.56	-5.15	-14.75	-68.24	-66.25
	FFT	n/a	-52.56	-79.04	-49.57	-26.65
Maximum deviation [$10^{-5} \frac{m}{s^2}$]	polyhedron	/	19.57	14.89	26.30	45.06
	GR3	-0.10	19.96	13.35	27.48	47.95
	Tesseroids	2.99	17.79	19.81	28.05	48.39
	FFT	n/a	-1.27	75.21	52.05	91.35

Table 3-2: Results of the first benchmark. It was not possible to calculate the topographic correction with FFT for the 90 m grid because the program was not capable to handle such a large DTM.

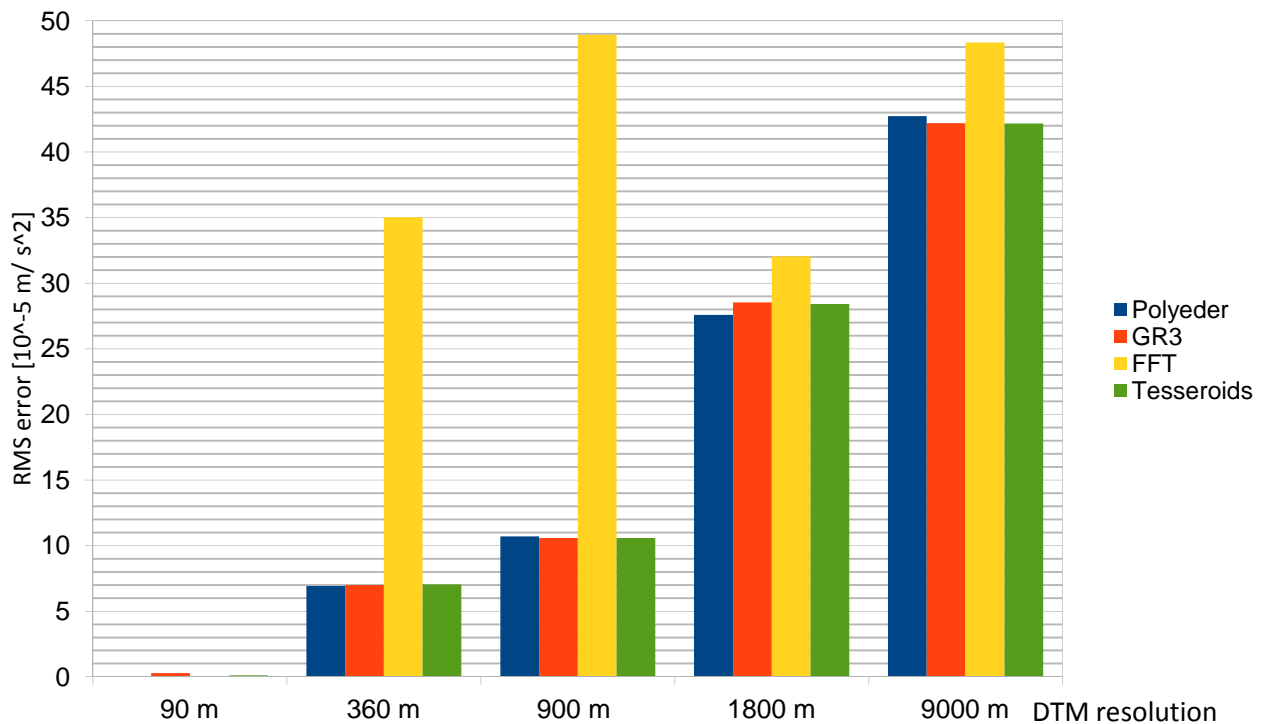


Figure 3-15: RMS error of results with different grid size compared to the 90 m DTM polyhedron correction. GR3, TriTop and tesseroids always provide almost the same deviation. The deviations become large for coarser grid resolutions. Note that it was not possible to calculate a FFT correction for a 90 m DTM.

Figure 3-16 shows the deviations from the 90 m reference calculation for each station summed up over all tested grid resolutions. Therefore, it can be interpreted how deviations correlate with the topographic environment. The coloured circle marks the mean deviation from the reference averaged over all grid resolutions. The error bar shows the minimum and maximum deviation. The largest deviations for all algorithms are observed at station 1,2,4 and 9. Station 2 and 9 are located in very rough terrain, so it is expected that a change in grid resolution affects the results. Station 1 is located at a valley, thus the correction is affected significantly by a coarser grid resolution. The valley is surrounded by steep topographic gradients. It is likely, that the averaging of topographic heights for the coarser grids causes large deviations from the geometry mapped in the 90 m DTM. FFT has large deviations for all stations compared to all other algorithms. GR3 and TriTop have almost the same deviations for each station. Tesseroids features less deviations than the other algorithms for station 5,7 and 8. Station 3,5,6 and 7 have the smallest variation in this test. Those stations are in flat or intermediate areas with less high mountains in proximity. In general, stations in "flat terrain" are not much affected by the change of grid resolution. Surprisingly, some stations in "flat areas" are significantly affected by coarser DTMs. These results show that it is complicated to decide if a station is located in a rugged or flat topographic environment. The choice of one specific grid resolution for correction already affects the results and can cause unexpected results.

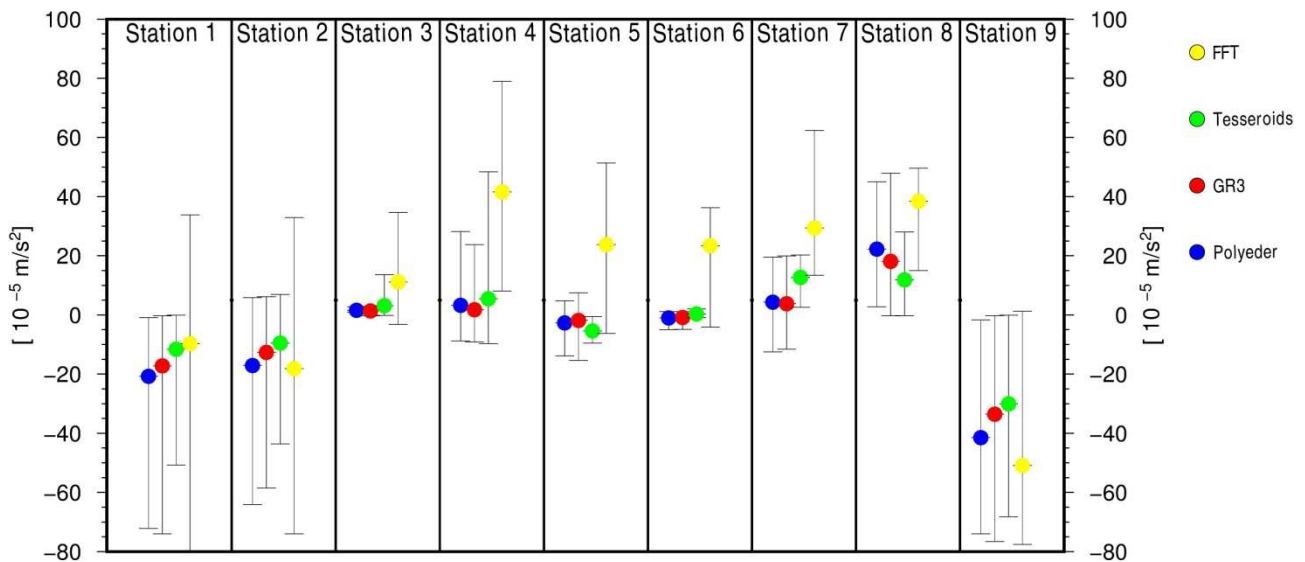


Figure 3-16: Deviations for each station over all different grid resolutions. The coloured dot shows the mean deviation. The error bar shows the minimum and maximum deviation. Stations in flat and intermediate terrain are less affected by grid resolution than stations in rough terrain.

What did we learnt from this test?

The test showed that in the area moderate differences between the methods are observed. The comparison for different resolutions showed that the differences increase with grid spacing of the DTM. Some of the initial questions can be answered.

- Are the results of the different algorithms similar?
 - Yes, the differences of the methods are very small except for the FFT algorithm. This clarifies, that FFT should not be used for corrections over the whole area.
- What is the effect on the results if different DTM resolutions are used?
 - There is a significant effect of choosing a different DTM resolution. If we assume that the calculation with a 90 m DTM is the most accurate correction, a choice of a coarser resolution can cause quite large deviations. The correction for stations in rugged terrain differs significantly. Corrections for stations in flat terrain are almost identical between high and low resolution. **Therefore, a correction with a coarse grid does not only cause a constant shift on all stations but even change the relative values to the stations.**
- What resolution of DTM should be chosen in general?
 - It is recommended to use the highest available DTM resolution. If coarser resolutions are chosen, errors can occur. However, in flat areas the differences are quite small. Therefore, in such areas a coarse DTM is probably appropriate for correction. However, it is not easy to decide if an area is "flat enough". Therefore a high resolution DTM with an automatic resampling technique should be chosen.

The remaining questions cover distant topography. In the next chapter an example in the same test bed will be shown.

3.4 Test bed Himalaya: Effect of distant topography

This chapter tries to answer questions about distant topography. Two open questions will be answered:

- What is the effect of distant topography?
- Is distant topography completely negligible?

The effect of distant topography is difficult to estimate before a calculation. The "distant topography" is defined to be beyond the "standard radius" of 1.5° (167 km) around a station. Investigations from other authors (Mikuška *et al.*, 2006, Talwani, 1998) conclude that distant topography have an impact on the corrections, especially in areas of rough terrain. Therefore, another test about the effect of distant topography in the Himalayan region were conducted. Here, the new TriTop algorithm was used. A correction limit around each station was defined. The test started with an area of 0.1° ($\approx 11 \text{ km}$) around each station and were increased by 0.1° until the correction equalled the correction for the full grid. Figure 3-17 shows the relation between correction values and distances to station. At 1.5° the correction of limited area is already $\approx 96\%$ of the full grid correction. The absolute correction values centered around $545 * 10^{-5} \frac{m}{s^2}$. Therefore, the remaining 4 % are approximately $22 * 10^{-5} \frac{m}{s^2}$. Table 3-3 shows the differences for each station compared to the full correction. The missing 4 % of the correction are not a constant shift over all stations, but differ from station to station. This causes correction artefacts in the final Bouguer gravity. The differences for an area limit of 2.5° are still in the same order. First, for an area limit of 14° the highest relative differences between the stations are around $1.5 * 10^{-5} \frac{m}{s^2}$. Station 2,5 and 7 have already very small differences compared to the full grid for a reduction area of 2.5° . The location of all those stations is in an area of intermediate to rough terrain. The largest effects of topographic corrections are caused by topography close to the station. Topography to the West of these stations is a plateau which causes only slight changes in the correction. Station 1, 3 and 6 have much more difference (about $10 * 10^{-5} \frac{m}{s^2}$ more) compared to the full grid at a reduction area of 2.5° . The stations are located on a plateau with only slight changes. If the reduction area is limited to 2.5° , the strong gradients which surround the Tibetan plateau are not included in the correction.

Station no.	Longitude[°]	Latitude[°]	Height[m]	Differences to full grid correction		
				1.5° area limit [$10^{-5} \frac{m}{s^2}$]	2.5 ° area limit [$10^{-5} \frac{m}{s^2}$]	14 ° area limit
1	87	32	6305	-24.34	-14.00	0.00
2	94	30	5730	-19.09	-9.05	-1.28
3	85	32	6120	-24.23	-15.03	-0.49
4	87	29	6080	-19.08	-14.69	0.00
5	96	33	5140	-16.42	-2.44	-0.29
6	85	34	5040	-21.67	-11.66	-0.49
7	95	32	5335	-17.86	-4.78	-0.89
8	77	33	6464	-24.70	-18.02	-2.82
9	78	35	5699	-22.92	-15.67	-2.75

Table 3-3: Correction values for a limited reduction area compared to the full grid correction. For some stations (e.g. 6) distant topography has a significant influence (some $10 * 10^{-5} \frac{m}{s^2}$). Stations located in flat terrain with rough terrain far away (>167 km) are affected by truncating the correction area. If stations are located in rough terrain flat distant topography is less affected.

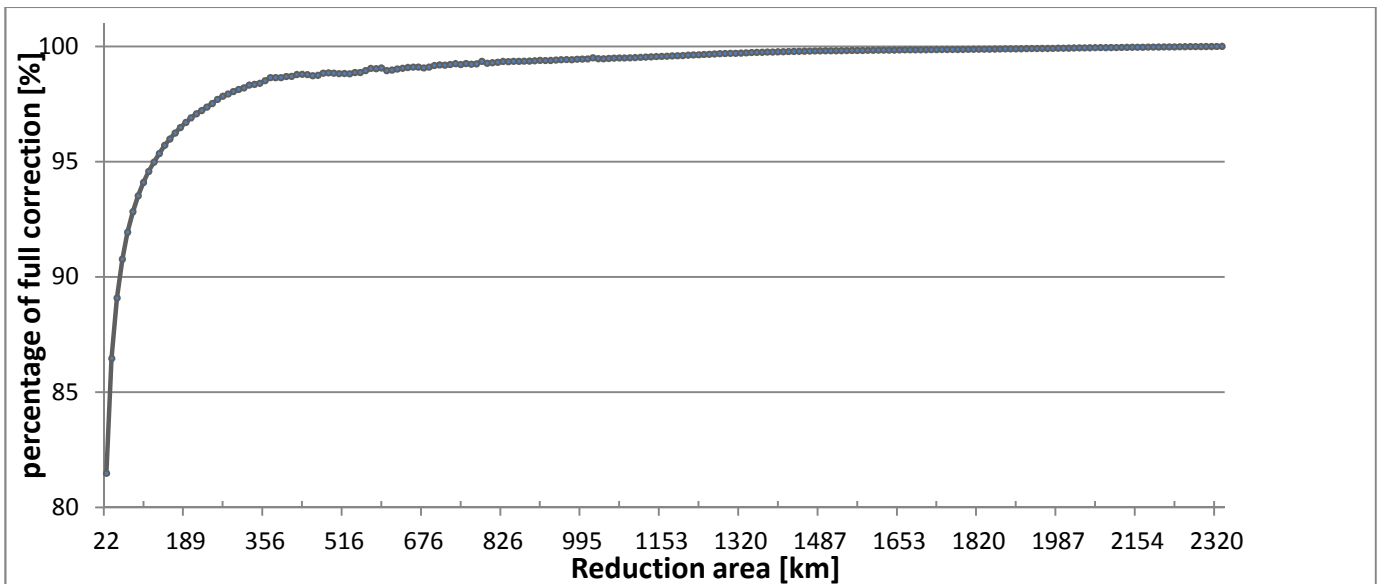


Figure 3-17: This Figure shows how the correction is affected by a reduction radius. At the standard radius of 167 km, already 95 % of the full signal is corrected.

What did be learnt from this test?

In this test case, the effect of distant topography has an influence on the stations. The correction values differ for all stations. Therefore, a limited correction can change the relative differences between stations which has an impact on the interpretation and modelling of the measured field. At a reduction area of 1.5° almost 96% of the topographic mass is corrected. Stations which are surrounded by rough terrain in proximity and flat distant terrain have already small differences to a full grid correction. However, stations which are surrounded by flat terrain and distant rough terrain have larger differences when the limited and full grid corrections are compared. Therefore, it can be necessary to represent distant topography with high resolution, at least for rugged terrain.

The outcome of this test makes it possible to answer the remaining two questions:

- What is the effect of distant topography?

First, distant topography causes a large constant shift to the correction values. The difference between the calculation with a large full grid and a limited area of 1.5° account for some $25 * 10^{-5} \frac{m}{s^2}$. Most of the effect is a constant shift which affects all stations. The relative values between the stations also changes up to $6 * 10^{-5} \frac{m}{s^2}$.

- Is distant topography negligible?

For interpretation and modelling Bouguer anomalies are often regarded as a relative quantity. Therefore, a constant shift can be neglected. The test showed that not only a constant shift affects the stations, but the misfits differed between the stations. The effect cause correction artefacts.

Stations with flat terrain in proximity and rough terrain as distant terrain showed more misfit than stations located in rough terrain. For the latter stations the largest effects of terrain are caused by masses close to the station, therefore they are more affected by nearby terrain and less by distant terrain. This observation makes it difficult to decide if a station is corrected sufficiently with a limiting radius. The user has to check the terrain close to the station but also the shape of distant terrain.

Finally, distant topography cannot be neglected without any further analysis of the terrain. Even stations on flat terrain can be influenced significantly which makes decisions difficult for users. Therefore, an automatic, adaptive algorithm should be used which decide the resolution of topography on the basis of the gravity effect (which includes geometry and distance). This algorithm was already presented in chapter 3.2.3.

3.5 Correction of Andean gravity data

In chapter 2.4.3 the gravity field of a subset of the Andes were discussed and compared to satellite gravity and global gravity models. It was concluded that in areas of rough terrain, measurements feature more deviations than other areas. Therefore, as a test, the mass correction will be recalculated with TriTop. The results will be analysed and compared to the primarily used GR3 results. For better comparison the initial GR3 result from Alasonati-Tašárová (2007) and recalculated GR3 results with a new topography grid were considered for comparison. For the new topographic correction a topography grid from -78W to -58W and -46 to -32 with a grid spacing of 30" and 3" was chosen from the ACE2 topography datasets. The grid contains 40 320 000 000 (3") and 4 032 000 (30") grid nodes and is approximately 4° larger in each direction than the bounding box of the stations.

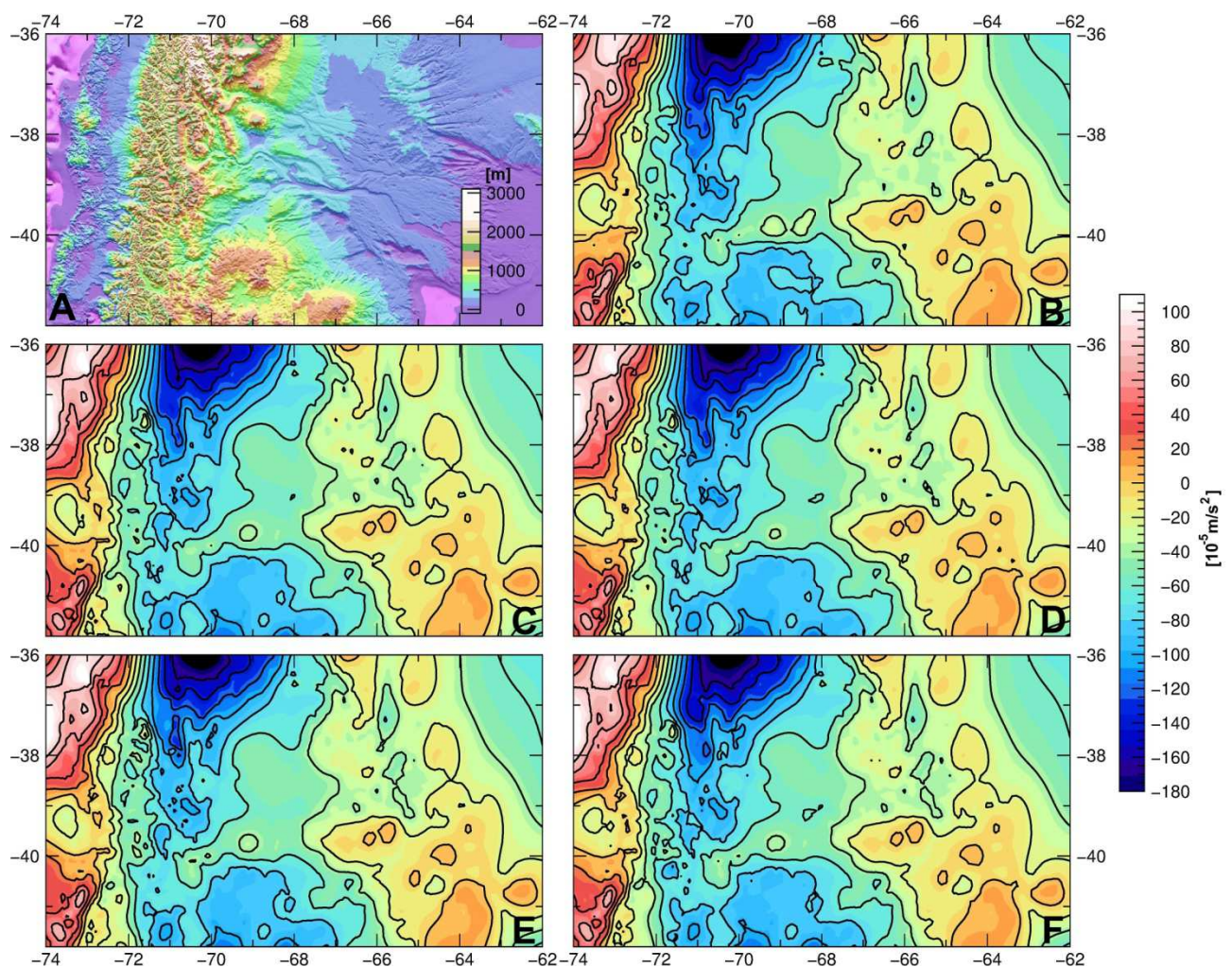


Figure 3-18: Maps of terrain corrected Bouguer gravity in the Andes with different parameters, data and algorithms (cf. Figure 3-19 for difference plots). (A) consists of the topography. (B) shows the initial terrain corrected Bouguer anomaly calculated by Alasonati-Tašárová (2007). In (C) the corrected anomaly (by GR3 and a 30" grid and a limiting radius of 222 km) is shown. The correction of (D) was calculated with TriTop with a limiting radius of 2°. (E) was corrected by adaptive TriTop correction with a 30" grid. (F) shows the same correction with a 3" grid. At a first glance, all maps are similar, in particular (A)-(D). In (F) a few high frequent anomalies show up in the coastal cordillera due to higher resolution of the DTM.

The calculations were performed with a limiting radius of 2° and adaptive resampling of topography (which always includes the full grid). The runtimes for the different calculations are shown in Table 3-4. Figure 3-18 contains Bouguer maps which result from the different calculations. Overall, the maps look quite similar with only small deviations. The adaptive approach ((E) and (F)) do not differ much from the calculations with a limiting radius ((C)-(D)). Therefore, distant terrain in this area which is included in the DTM does not have much influence on the results. Slight differences are along the coastal cordillera (between -73° to 70°) where topography is highest. For better comparison, a difference map was calculated (Figure 3-19). In this figure, the differences were plotted as points along the stations to avoid interpretation of interpolation effects. (A)-(C) were always compared to the GR3 calculation with a $30''$ grid and a limiting radius of 222 km ($\sim 2^\circ$). In (A) we have corrections calculated by TriTop with a $30''$ grid and a limiting radius of 2° . Almost no differences show up. Only a slight shift in the East of less than $3 * 10^{-5} \frac{m}{s^2}$. In this area both algorithms perform very similar if the same parameters and input data are used. (B) TriTop calculation with the same grid but an adaptive resampling of the full grid. Here, differences at the coastal cordillera (in the high topography area) are observed. The TriTop corrected Bouguer anomaly is $3 * 10^{-5} \frac{m}{s^2}$ higher than the anomaly corrected by GR3. The limiting radius was deactivated and the differences are caused by distant terrain effects. The Eastern part of the area does not show any differences. Thus, here distant terrain is not a constant shift over all stations and changes the relative quantity between the stations. (C) is the TriTop correction with $3''$ and a adaptive approach. The results show also positive differences compared to GR3. However, at -72° negative differences are calculated.

The difference between the TriTop $3''$ adaptive topography correction and the initial calculation used by Alasonati-Tašárová (2007) (D). The differences are larger than before and spread over the whole Western part of the investigation area. Alasonati-Tašárová (2007) For the map (D) a different DTM was used which causes the increased differences to the TriTop correction. The Bouguer anomaly is more positive at -72° and more negative between -70° and -68° . The positive anomalies are located at the longitudinal valley and the fore-arc sedimentary basins. The negative difference between -70° and -68° is located in the South of the Neuquén basin (cf. Figure 3-20). The positive Bouguer anomaly is interpreted as the border between the Neuquén basin and the North Patagonian massif (Alasonati-Tašárová, 2007). The new Bouguer anomaly implies a more negative anomaly, therefore less mass in this area.

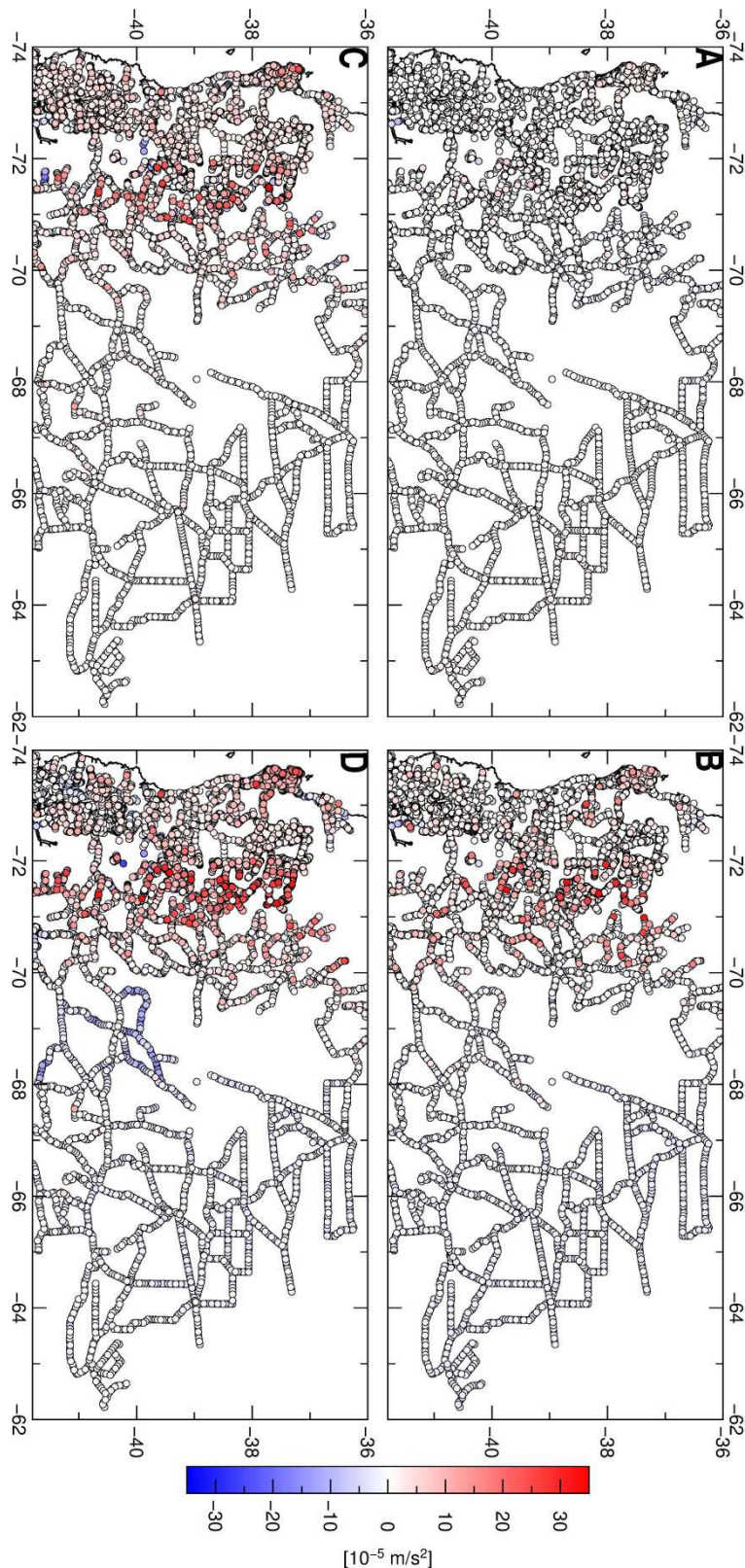


Figure 3-19: Differences between different correction calculations. The maps depict only differences at the stations. This avoids interpreting interpolation effects. In the maps (A)-(C) always the GR3 correction with a 30'' grid and a limiting radius of 222 km was subtracted. (A) portrays TriTop calculation with a 30'' grid and a limiting radius of approximately 222 km. For (B) TriTop calculated with the adaptive approach and a 30'' grid. (C) is the TriTop calculation with a 3'' grid and the adaptive approach (D) represents the difference between the initial Bouguer anomaly from Alasonati-Tašárová (2007) and the TriTop calculation with the adaptive approach and a 3'' grid.

Finally, the recalculation shows some differences to the previous calculated Bouguer anomaly. The consideration of distant terrain causes more positive anomalies along the longitudinal valley and the fore-arc sedimentary basins. However, a few stations in this area are more negative which is caused by a higher DTM resolution. Interestingly, the correction with the new topography causes also differences in the South of the Neuquén basin at the Border to the North Patagonian massif.

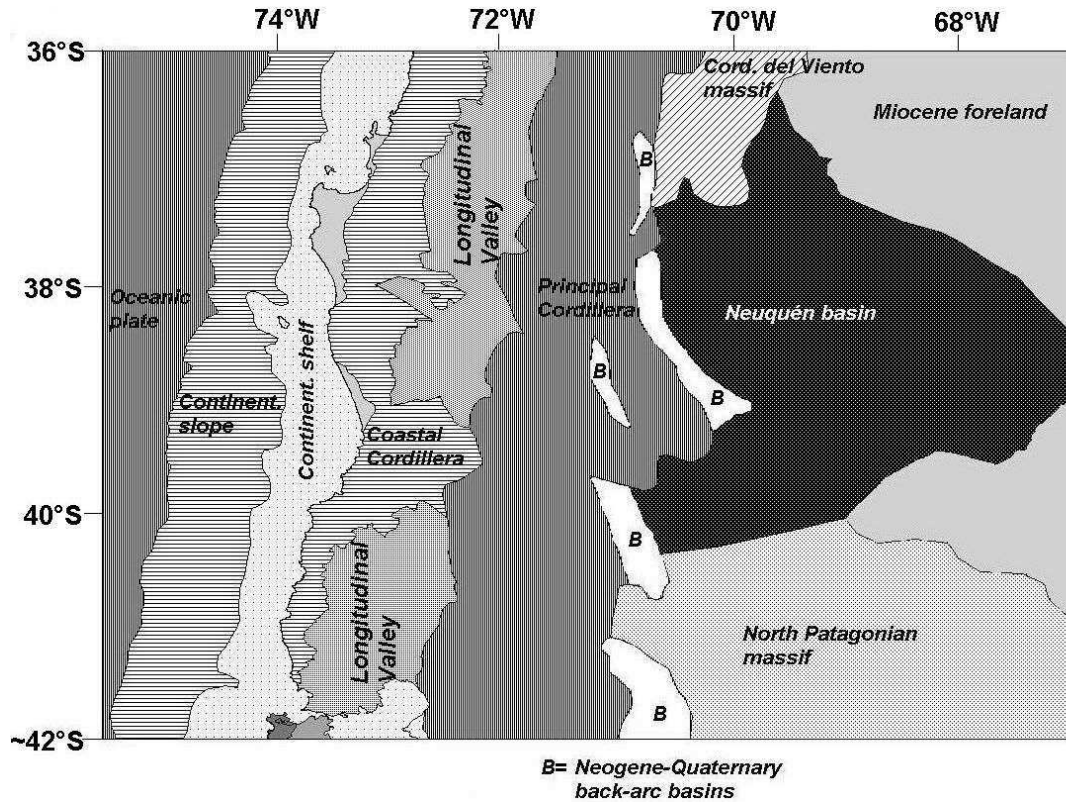


Figure 3-20: From Tašárová (2004) modified after Melnick(2003, pers. comm.). The map shows the morphological structures in this area. Some features are visible in the gravity field, e.g. the adjoining North Patagonian massif and the Neuquén basin.

Algorithm	Grid resolution	Limiting radius (°)	Runtime (min) for 14210 stations
GR3	30 "	2	93
polyhedron normal	30"	2	480
polyhedron adaptive	30"	Full grid (adaptive)	280
polyhedron adaptive	3"	Full grid (adaptive)	350

Table 3-4: Calculation time of different algorithms for the discussed area in chapter 3.5. In this case, the adaptive approach saves 40 % of computation time compared to the normal correction with a limiting radius of 2°. The runtime is longer than GR3 but accounts for more distant terrain effects.

3.6 Gradient correction of satellite data

GOCE is the first satellite which measures gravity gradients directly. The use of gravity gradients for interpretation is an ongoing study. Gradients offer a better signal to noise ratio and emphasize geological structures (cf. chapter 2.1). Gradients are the second derivative from the gravitational potential, the gradient signal decreases with $\frac{1}{r^3}$. Thus, gradients are more sensitive to topography than gravity. For investigation of the lithosphere, gravity gradients have to be topographically corrected, too. The correction of gradients is not implemented in previous algorithms (e.g. GR3).

TriTop is able to correct the gravity gradients for the topographic effect. Figure 3-21 shows the gravity gradients derived from GOCO02-S (Pail *et al.*, 2010) in 254km height over ellipsoid. The signal varies between -3 to 2.5 Eötvös. Most signal can be seen in the components g_{xz} , g_{yz} , g_{zz} . The gradients show anomalies in the area of high topography at the coastal cordillera. Figure 3-22 shows the gravity gradients caused by topography calculated by TriTop. The magnitude of the values is in the same range than the measured signal. The strong anomalies west of the coastline are caused by the Andes. The g_{zz} component is also influenced by the deep sea trench east of the coastline which causes the elongated positive anomaly. The final gravity gradients are shown in Figure 3-23. The gradients g_{xz} , g_{yz} , g_{zz} reflect effects caused by the crustal root of the mountain range, e.g. a negative anomaly between -72° to -68° W and -32 to -42° S in the g_{xz} component. The signal of g_{yz} is close to zero, but at -40° S the border between the Neuquén basin and the North Patagonian massif is visible. g_{zz} correlates with better with the longitudinal valley and the coastal cordillera (cf. Figure 3-20). The measured signal is in the same range than the topographic corrections, even in a flight height of 254 km. Therefore, gradients have to be corrected for topography. Features like the border between the Neuquén basin and the North Patagonian massif became visible after the correction of the g_{yz} and g_{zz} components. Therefore, the new algorithm is a valuable tool for processing gravity gradients for modelling and interpretation of the lithosphere.

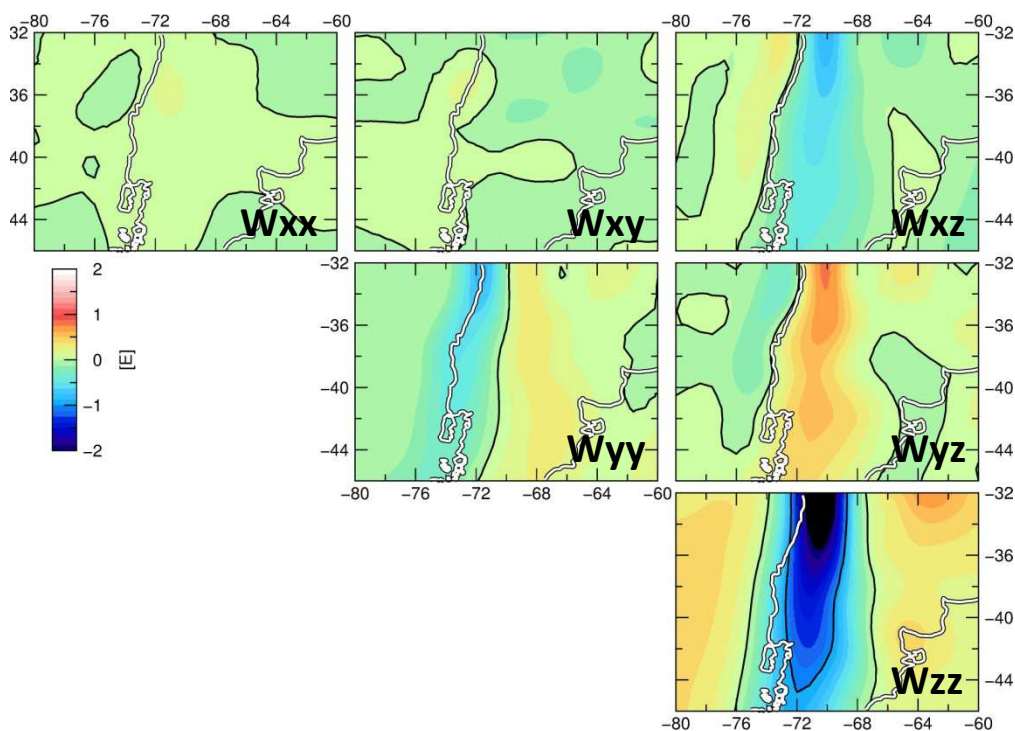


Figure 3-21: Gravity gradients from GOCO02-S in flight height of the satellite (254 km). The white line is the coastline.

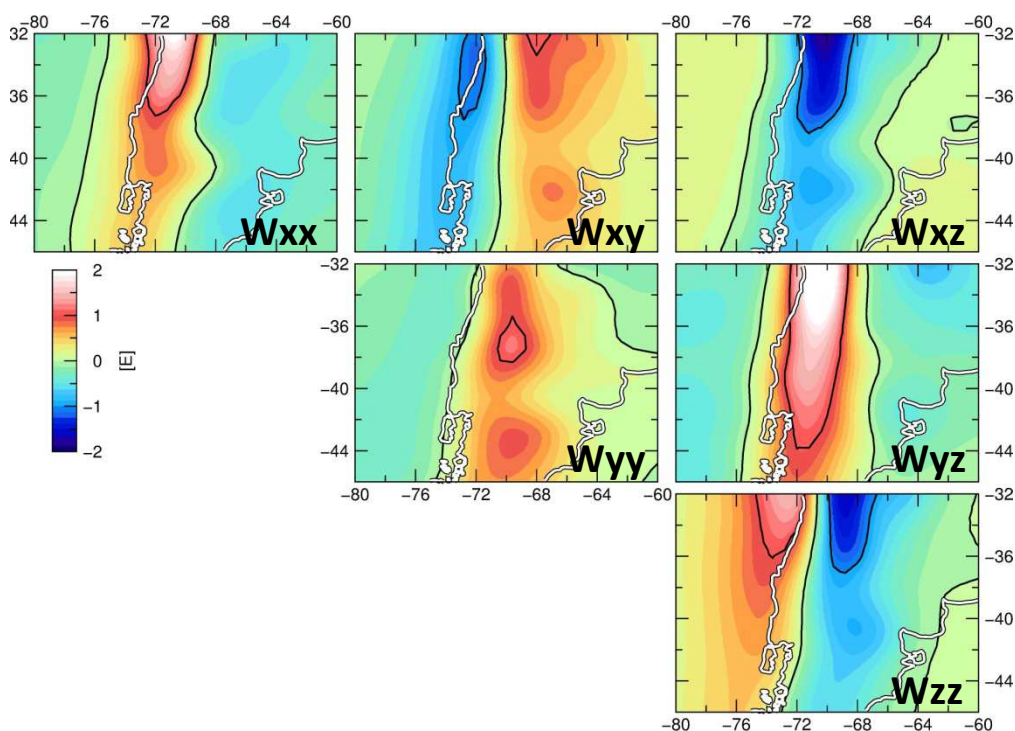


Figure 3-22: Gravity gradients caused by topography (calculations by TriTop). The magnitude of anomalies are in the same range as the measured gradients in Figure 3-21.

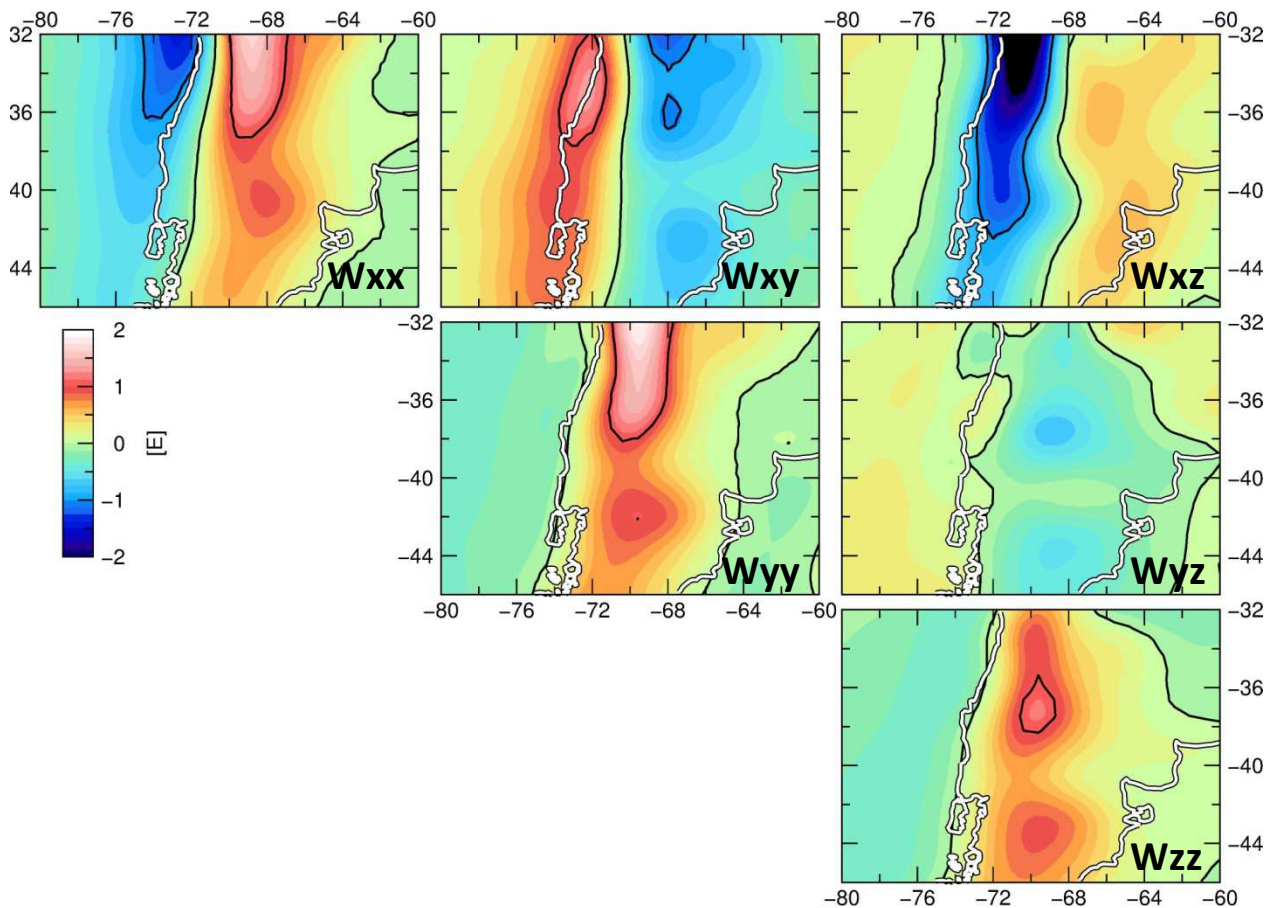


Figure 3-23: GOCE gradients corrected for topography. The anomalies show lithospheric structures like the crustal root and morphological boundaries.

3.7 Final conclusions for topographic correction

The preparation of gravity data for interpreting anomalous structures in the lithosphere involves several reductions which were shown in chapter 3.1. In theory, these reductions always subtract signals from "known" sources like the normal gravity of the earth. The quality of the correction depends on the quality of geometry and density representation of the algorithm.

Topographic correction is a mandatory processing step because free air gravity is highly influenced by topographic effects. After this step isostatic effects and anomalies caused by different morphological structures in the subsurface are visible. The historical overview shows first steps of topographic corrections which were conducted station dependent. Those methods lead to redundant calculations for estimating mean heights for each station. Since the 60s several computer methods were developed which eases this calculation step. A station independent resampling approach and a spherical representation of topography with prisms developed by Ehrismann and Lettau (1971) was presented.

A new correction algorithm based on polyhedrons Götze (1976) was set up. The algorithm were modified to consider sphericity of the earth and avoids using projected coordinates. In addition, a triangulation algorithm were developed which is capable to combine grids and irregular data with only few memory consumption. Furthermore, it divides land and oceanic bodies automatically.

The availability of global gravity and gradient models asked for an algorithm which is able to calculate the gravity gradient effect of topography, deals with large topographic grids and applies an "intelligent" resampling of topography to save computation time. A new method was developed and presented where the topography is resampled depending on its influence on gravity (gradients) at a station.

As a first test, different algorithms were compared for selected stations in the Himalayan region. The representation of topography with prisms, polyhedrons and tesseroids (all considering sphericity of the earth) provide similar results. Calculations with FFT feature large deviations for all stations. The test also compared the calculation for different grid resolutions. It was shown, that the choice of grid resolution has a large impact on the final results. It was also proved that the adaptive approach is similar to a calculation with a high resolution grid with only a fraction of computation time (compared to corrections with constant grid resolution).

The effect of distant terrain was investigated (beyond 167 km) because Mikuška *et al.* (2006) concluded that distant terrain can have an significant influence on gravity data and should be considered in areas of rugged terrain. The test bed around the Himalaya is a good example of rugged terrain, but the effect of distant terrain was not constant for all stations. Thus, corrections with a limiting radius around the stations cause different results compared to the correction without any limiting radius. The relative quantity between the stations changed by up to $6 * 10^{-5} \frac{m}{s^2}$ (cf. chapter 3.4).

Therefore, if computation time should be kept low one should not using a coarse grid, FFT or a limiting radius, but the new developed adaptive approach.

The algorithm were also tested on real stations, which were used for modelling at the Andean subduction zone by Tašárová (2004) (cf. chapter 2.4.3 and 3.5). For better comparison, topographic corrections were also recalculated with GR3 (which was also used by Tašárová (2004)) and the new topography grid. In this area, the corrections by polyhedrons and prism representation were similar. The correction with the adaptive approach and a 3" grid show slightly more positive anomalies at the coastal cordillera. However, also some more negative anomalies in the fore-arc basins are observed. In addition, the comparisons with the former Bouguer anomaly compilation (from (Tašárová, 2004) show deviations in the back-arc of the Andes, where the Neuquén basin adjoin the North Patagonian massif. My new corrected Bouguer anomaly correlates far better with the geological underground structures.

The grid for the Andean correction extends 20° in width and 14° in height with a resolution of 3" and consists of approximately 40 billion stations. In this case, the adaptive approach only needs ~1 sec. for reduction of a station.

The last example was the correction of gravity gradients in the Andean region. Gradients are more affected topography than gravity. Lithospheric structures are revealed by the effect of topography. The mass corrected gravity gradients show structures of the adjoining Neuquén basin and the North Patagonian massif and the crustal root of the Andes which were not visible beforehand. The new GOCE gradient data has to be corrected for interpretation and modelling and the polyhedron algorithm is one of the first methods which is capable to provide such correction data.

Beside the development of a new algorithm, a second objective was the development of a software package, which can be provided to researchers and applied to **any other area**. A new platform independent program were created which is capable to calculate corrections for all components of the gravity vector and the gravity gradient tensor.

Finally, the analysis show that high resolution grids and no limiting radius should be used. Furthermore, in mountainous area it is not possible to decide the necessary accuracy of topographic correction by qualitative analysis. Regional gravity (gradient) studies ask for a robust and quick method for correction. The new developed method is able to fit all that needs.

4 Crustal structure of the northern Perth Basin, southwest margin of Australia: insights from three-dimensional density models

After describing investigations in the fore-arc and back-arc of an active continental margin, the new algorithm TriTop now should be applied to another tectonic environment: a passive continental margin. Passive continental margins are in focus of international research and of hydrocarbon industry. Rifting can occur at these margins which causes the evolution of sedimentary basins. Tectonic processes cause rather small gravity anomalies and a careful topographic correction of both on and offshore gravity data is required. Here, my investigations are concentrating on potential resources located in these basins (Bähr *et al.*, 2003). The selected area is located at the Western Australian margin and the size of the investigation area is about 250 x 250 km which is much smaller than the area in the Andes. Figure 4-2 shows a geological overview over the area and the topography (and bathymetry). The modelled area comprises landmass and ocean and it was already mentioned in chapter 3.2.1 that the density boundaries between water and rock bears severe problems for topographic corrections. Therefore, this study seems to be very appropriate to test the new topographic correction algorithm.

Bouguer gravity was calculated with two different approaches: The initial correction was conducted with a spherical Bouguer slab combined with topographic correction (represented by prisms) and a limiting radius of 167 km. The new correction bases on TriTop with a 3" DTM and the new adaptive approach. The grid is 6° larger in all directions than the bounding box of the stations and no limiting radius is defined. Figure 4-1(A) shows the initial Bouguer gravity map, (B) the recalculation by TriTop and (C) a difference plot (new corrected Bouguer anomaly minus the initial compilation). Most remarkable differences are observed onshore. Here, deviations in the North of the Dandaragan trough are about $15 * 10^{-5} \frac{m}{s^2}$. Differences in the rest of the area feature only slight deviation from the initial calculations. Anomalies in the offshore areas are slightly more negative (with a mean of $\sim -1.6 * 10^{-5} \frac{m}{s^2}$) than in the initial compilation, while onshore areas are characterized by rather positive gravity values (mean of approximately $2.3 * 10^{-5} \frac{m}{s^2}$). In my new Bouguer map the gravity low, caused by structures of the Dandaragan trough extends less to the North which fits to the geological interpreted structural elements. In addition, the whole anomaly is slightly more positive (about $3-4 * 10^{-5} \frac{m}{s^2}$) than it is in the South of the trough.

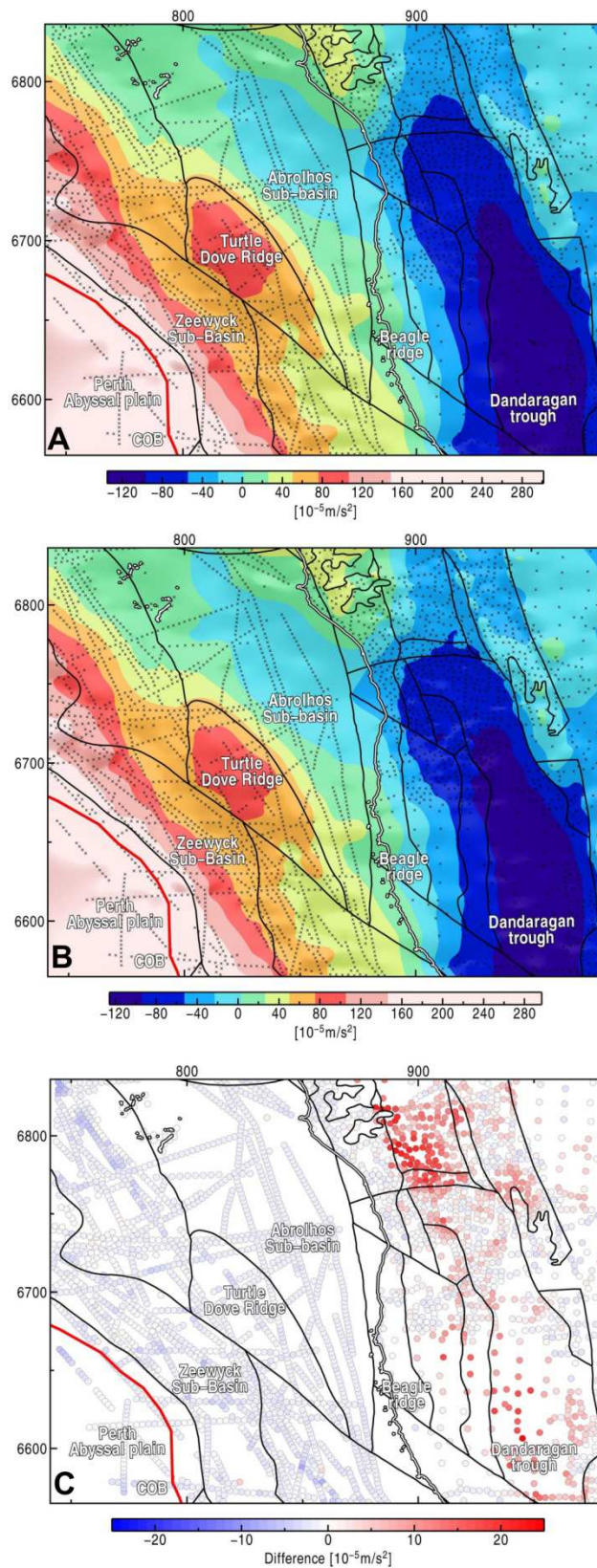


Figure 4-1: Bouguer anomaly maps at the West Australian margin. Part (A) shows the initial compiled Bouguer anomaly corrected by a spherical Bouguer slab and topographic correction which is conducted with prisms. Figure (B) shows the recalculated Bouguer anomaly based on the adaptive approach and part (C) illustrates the difference between both.

The new calculation improves the correlation of gravity and geological structures in the Dandaragan trough. The results stress out the need of an accurate topographic reduction even in onshore areas of rather flat terrain (compared to the other test beds in chapter 3.3 and 3.5).

The northern Perth Basin formed from rocks of the Paleozoic to Mesozoic within an obliquely-oriented extensional rift system on the southwest continental margin of Australia. A general knowledge of the basin in onshore and inboard areas allows better accessibility and can support the exploration of hydrocarbon resources. To constrain sediment thicknesses and crustal structures in the northern Perth Basin, 3D density modelling was conducted; it bases on terrestrial gravity data, particularly in offshore areas where coverage of seismic data is less extensive. This shows the importance to gravity ground data at a passive continental margins. Even more these terrestrial gravity provides added value to the interpretation of sedimentary thickness and the determination of the crust-Mantle boundary (Moho) in the transition of the oceanic and continental lithosphere. The final models and interpretations will be compared with satellite data to point out the different resolution of both measurements and interpret the sensitivity of satellite data in this area.

4.1 Introduction

The northern Perth Basin is an under-explored part of the southwest continental margin of Australia that formed from the Paleozoic to Mesozoic within an obliquely-oriented extensional rift system (Harris, 1994, Iasky and Mory, 1993, Mory and Iasky, 1996, Norvick, 2004, Quaife *et al.*, 1994). Onshore and inboard parts of the northern Perth Basin have proven hydrocarbon potential (Buswell *et al.*, 2004), while the prospectivity of deeper water areas has recently been re-examined (Jones *et al.*, 2011, Rollet *et al.*, in press). The availability of data that constrains crustal structure in the northern Perth Basin reflects the level of exploration. Onshore and inboard areas are well covered by seismic reflection data and some wells, whereas data coverage in outboard areas is far less comprehensive.

The main sediment depocentres of the northern Perth Basin (Figure 4-2) include the onshore Dandaragan Trough, the inboard Abrolhos Sub-basin and the deep water Houtman and Zeewyck sub-basins. The Beagle Ridge separates the Dandaragan Trough from the Abrolhos Sub-basin and the Abrolhos and Houtman/Zeewyck sub-basins are separated by the Turtle Dove Ridge. On its eastern margin, the northern Perth Basin is separated from the Archean Yilgarn Craton by the north-south-trending Darling Fault. Seismic reflection data suggest that the Darling Fault is a sub-vertical fault that penetrates through much of the crust (Dentith *et al.*, 1993).

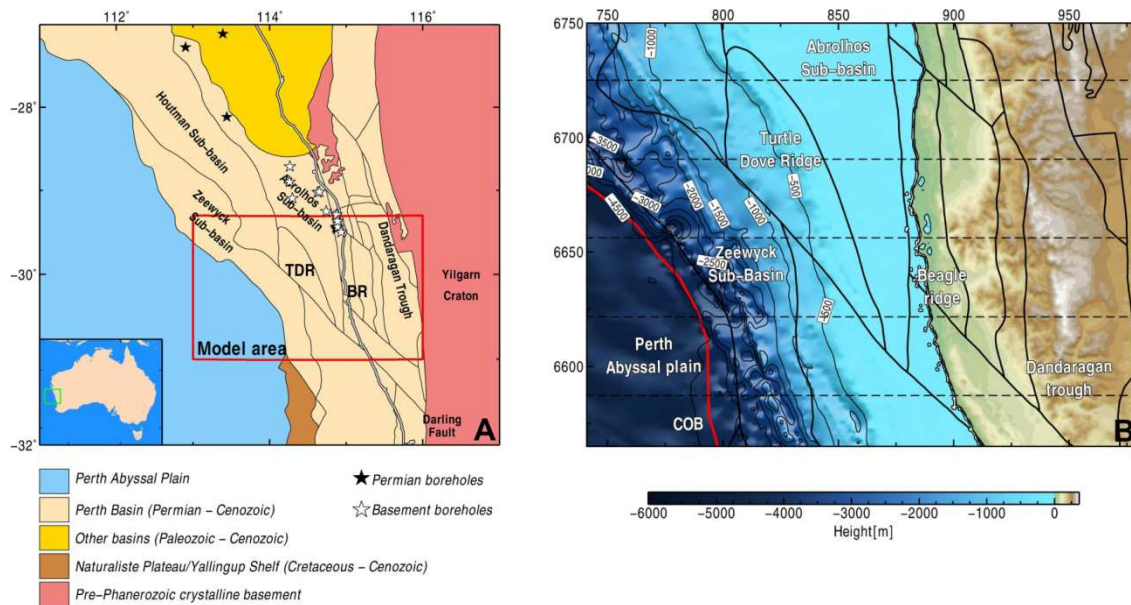


Figure 4-2: (a) Simplified geological map of the northern Perth Basin showing province boundaries from the Geoscience Australia Provinces Database (<http://www.ga.gov.au/provexplorer/>). The red box shows the area of the 3D gravity model. The main features included in the model are labelled (TDR, Turtle Dove Ridge; BR, Beagle Ridge). Black stars show selected boreholes that reached basement and white stars show selected boreholes that penetrated to Permian sediments. The white-on-black line is the Western Australian coast. (b) Bathymetry and topography in the model area (red box in A) from the compilation described by Whiteway (2009). Black solid lines show the boundaries of major geological features (as in A). Thin dashed lines show the location of the vertical sections used in the 3D models. The red line marks the continent–ocean boundary (COB) as interpreted by Hall (in press). Map projection is UTM Zone 49 South.

In 2008-09, Geoscience Australia acquired 7300 km of 2D seismic reflection data on the southwestern margin of Australia (Geoscience Australia, 2011). Together with re-processing of 11700 km of open-file industry seismic data, these data provided new impetus for studies of the frontier basins in the region. This work has revealed significant petroleum potential in the more outboard parts of the northern Perth Basin (Jones *et al.*, 2011, Rollet *et al.*, in press).

Whilst regional-scale interpretation of the new and existing 2D seismic reflection data has provided important new insights into the structural framework of the basin (Jones *et al.*, 2011, Rollet *et al.*, in press, Hall *et al.*, in press), a number of outstanding issues remain which cannot be addressed using seismic data alone. For example, depth to basement, basement architecture and crustal structure remain poorly determined in the deep water parts of the offshore northern Perth Basin. However, basement depth and crustal thickness are important parameters when interpreting the tectonic or thermal evolution of a margin.

Density modelling can help to constrain crustal structure and basement depth associated with sedimentary basins (e.g. Antobreh *et al.*, 2009, Ashcroft *et al.*, 1999, Barrère *et al.*, 2009, Blauch *et al.*, 2010, Chappell and Kusznir, 2008, Iasky *et al.*, 1997, Iasky *et al.*, 1991, Kimbell *et al.*, 2010,

Reynisson *et al.*, 2010, Smallgood *et al.*, 2001, Sweetman, 1997, Welford *et al.*, 2010). To help constrain uncertainties in the northern Perth Basin, we constructed three-dimensional (3D) forward gravity models of a part of the northern Perth Basin that encompasses the Zeewyck Sub-basin, Turtle Dove Ridge, the southern parts of the Abrolhos Sub-basin, the Beagle Ridge and the onshore Dandaragan Trough. This area was chosen for the reasonable coverage of data and unknowns such as the depth of sediments in the Zeewyck Sub-basin and the origin of the Turtle Dove Ridge (Jones *et al.*, 2011, Hall *et al.*, in press). The 3D models are used to test seismic interpretations of geological horizons and to provide insights into crustal structure and the deeper parts of the basins where the seismic data do not resolve geological features. The models also provide the impetus to re-interpret areas where the existing seismic interpretation appears to be inconsistent with the subsurface mass distribution reflected in the gravity field (cf. Sweetman, 1997, Higgins *et al.*, 2011).

4.2 Constraining Data

4.2.1 Bathymetry and Topography

The bathymetry and topography data used (Figure 4-2b) are from the compilation described by Whiteway (2009). In offshore areas, this dataset combines swath bathymetry data with data from the ETOPO1 global dataset (Amante and Eakins, 2009). Onshore elevation data are from Geoscience Australia's 9" digital elevation model (Geoscience Australia, 2008). In the modelling area, the maximum water depth is about 6000 m and onshore elevations reach 350 m (Figure 4-2a).

4.2.2 Gravity Data

Our modelling relies on a new compilation of onshore and offshore gravity and magnetic data for the southwest margin of Australia (Hackney, 2012). Onshore gravity data are from the Australian National Gravity Database (Tracey and Nakamura, 2010). The standard deviation for values in the onshore dataset is $1 \times 10^{-5} \frac{m}{s^2}$ and the error is in the range of $0.6-6 \times 10^{-5} \frac{m}{s^2}$. In offshore areas, levelled ship-track gravity data from a dataset described by Petkovic *et al.* (2001) were combined and re-levelled with data from three more recent marine surveys (Hackney, 2012).

We used free-air anomalies from the merged onshore and offshore gravity dataset and recomputed Bouguer anomalies onshore and offshore using a spherical cap Bouguer correction and densities of 2670 kg/m^3 onshore and 1640 kg/m^3 offshore (Figure 4-3a). In offshore areas, the Bouguer correction seeks to minimize the gravity effect of the seafloor density contrast between water and rock. This is achieved by replacing the seawater with rock with a density of 2670 kg/m^3 , so the correction density of 1640 kg/m^3 is the density difference between rock and seawater (1030 kg/m^3).

There are some prominent features in the Bouguer gravity map (Figure 4-3a). Onshore, a north-south-trending negative anomaly (about $-130 \times 10^{-5} \frac{m}{s^2}$) is related to the Dandaragan Trough.

Mory and Iasky (1996) estimated a maximum sediment thickness of more than 10 km in the Dandaragan Trough. Northeast of this anomaly, a positive anomaly with an amplitude of $10\text{--}40 \times 10^{-5} \frac{m}{s^2}$ is evident. This is related to the outcropping Yilgarn Craton.

To the west of the gravity low associated with the Dandaragan Trough, the Beagle Ridge and Abrolhos Sub-basin correspond with an increase in gravity towards the Turtle Dove Ridge, a basement high associated with a positive Bouguer anomaly of about $100 \times 10^{-5} \frac{m}{s^2}$. To the west of the Turtle Dove Ridge, the Zeewyck Sub-Basin is associated with a relative Bouguer gravity low that is about $10\text{--}20 \times 10^{-5} \frac{m}{s^2}$ less than adjacent areas. Further west, the Perth Abyssal Plain correlates with a positive Bouguer anomaly of about $120 \times 10^{-5} \frac{m}{s^2}$. The eastern limit of this high coincides with the continent–ocean boundary (COB) as defined by Hall (in press).

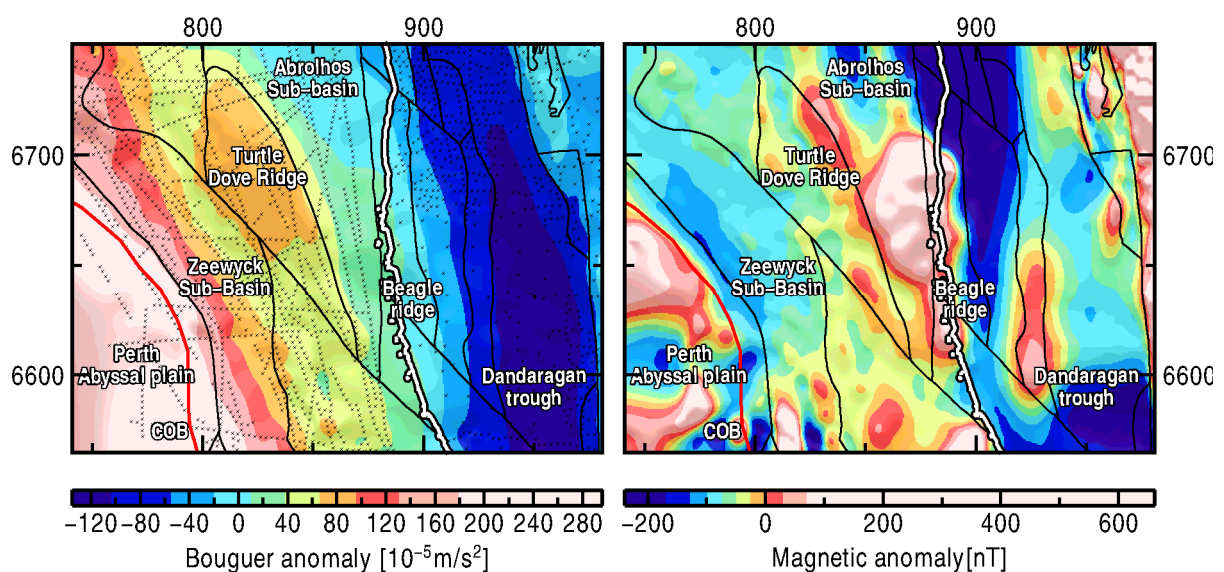


Figure 4-3: (a) Bouguer gravity anomaly and measurement locations (black dots). (b) Induced magnetic anomaly in the model area. The red line marks the continent–ocean boundary (COB) as interpreted by Hall (in press). The white-on-black line shows the coastline. Black lines outline the major structural elements (as in Figure 4-2). Map projection is UTM Zone 49 South.

Magnetic anomaly data for the model area are shown in Figure 4-3b. The highest magnetic anomalies are associated with the Archean Yilgarn Craton (east of the Darling Fault) and oceanic crust (southwest of the continent–ocean boundary). Apart from relatively high anomalies in the southern Abrolhos Sub-basin, much of this part of the northern Perth Basin is associated with relatively subdued magnetic anomalies. There are few obvious correlations between magnetic data and structural elements, but the magnetic anomalies are more positive over the Turtle Dove Ridge than over the Zeewyck Sub-basin. Hence, magnetic data appear to dominantly reflect changes in depth to basement. We did not model the magnetic data, but in this area, Johnston and Petkovic (2012) conducted 2D forward modelling and spectral depth-to-basement estimation. They showed that long-wavelength magnetic anomalies are generally related to variations in depth to basement. They accounted for short-wavelength anomalies by including strongly magnetized, arbitrarily-shaped bodies within basement or the deepest sediments. Though not

constrained by independent observations, these magnetized bodies were attributed to dykes or sills within or just above basement.

4.2.3 Seismic Interpretation of Sediment Thickness

To constrain the geometry of the sediment bodies in onshore areas, mainly the Dandaragan Trough, we used the interpretation described by Mory and Iasky (1996) along the white seismic lines shown in Figure 4-4a and b. In offshore areas, geometrical constraints are from the interpretation of both reprocessed seismic reflection data and newer data from the GA-310 seismic reflection survey (Jones *et al.*, 2011). Conversion of the seismic interpretation from time to depth was made using average velocities computed from seismic stacking velocities. The stacking velocities were compared to sparse borehole checkshots in the region to assess their applicability for depth conversion. There is a good correlation between depth obtained from stacking velocities and checkshots, at least over the depth range of the boreholes (Johnston and Goncharov, 2012).

We used a two-layer model of the sedimentary units that comprises post-Permian and Permian sediments (Fig. 3). The water bottom, which marks the top of the sediments, is from the bathymetry dataset described by (Whiteway). The boundary between the two sedimentary layers is defined by the Top Permian horizon interpreted from seismic reflection data (Figure 4-4b). The depth-to-basement is based on the “base resolvable section” horizon (Figure 4-4a), a horizon that represents the depth to the deepest reflectivity evident in the seismic sections.

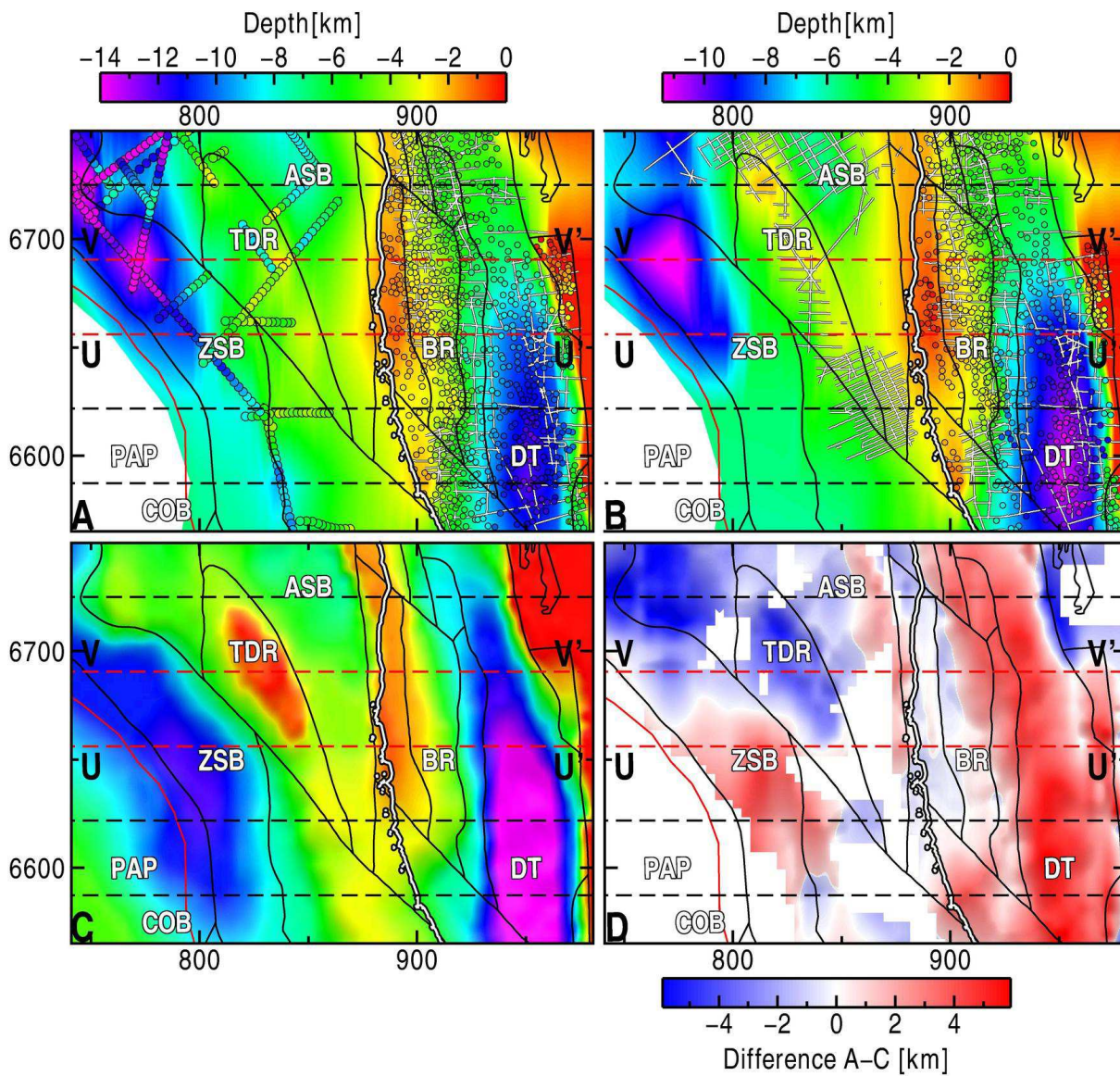


Figure 4-4: Maps showing depths to sedimentary horizons from the interpretation of new and re-processed seismic reflection data. (a) Depth to “base resolvable section” derived from seismic interpretation (onshore from Mory and Iasky, 1996; offshore from Bernardel and Nicholson, 2013). This horizon is used to represent the top of basement. Colored circles show the depths along the seismic lines to the respective horizons from the depth-converted seismic interpretation. In a, interpretation issues are highlighted by mismatches at line cross-overs. (b) Depth to the Top Permian horizon (Mory and Iasky, 1996, Jones et al., 2011). The colored image in the background shows the interpolated surface that was imported into the initial 3D gravity model (note that sediment thickness was forced to zero at the continent–ocean boundary). The white lines show the extent of interpretation onshore and offshore (Mory and Iasky, 1996). (c) Depth to basement from the OZ-SEEBASE dataset (FrOG Tech, 2005) plotted using the same color scale as the depth to base resolvable section in a. (d) Difference between basement depths in “base resolvable section” (a) and OZ-SEEBASE (c). Each map includes structural elements, continent–ocean boundary and coastline as described in Figure 4-1 (PAP, Perth Abyssal Plain; ZSB, Zeewyck Sub-basin; TDR, Turtle Dove Ridge; ASB, Abrolhos Sub-basin; BR, Beagle Ridge; DT, Dandaragan Trough). East–west dashed lines show the location of the vertical sections used to define the geometry of the 3D

gravity model (red dashed lines show sections U and V through the 3D model that are illustrated in Figures 4-7 to 10). Map projection is UTM Zone 49 South.

The seismic interpretation of both horizons (Figure 4-4a and b) is generally reliable because it is sufficiently resolved in the seismic reflection data (cf. Jones *et al.*, 2011, Mory and Iasky, 1996). However, the coverage of seismic lines varies considerably, meaning that the horizons are better constrained in onshore areas than in offshore areas. For both horizons, coverage over the Turtle Dove Ridge and in the north of the Abrolhos Sub-basin is reasonable. However, for the Top Permian horizon, there is no interpretation to the west of the Turtle Dove Ridge in the Zeewyck Sub-basin, mainly because it is not resolved in the seismic data (cf. Jones *et al.*, 2011). This means that the geometry of the Top Permian horizon used in the Zeewyck Sub-basin parts of the model is based purely on extrapolation and is less reliable. The Top Basement boundary is better constrained in the Zeewyck Sub-basin. However, in some areas (especially in the Zeewyck Sub-basin) there are large misties of about 2000 m at the intersection of some seismic lines (Figure 4-4a). Therefore, for the Top Basement boundary (base resolvable section), an uncertainty of ± 2000 m is expected in offshore areas. Due to the decreasing seismic resolution with depth, it is expected that the interpretation of the Top Basement boundary is even more uncertain in the deepest sedimentary basins.

The depth of the Abroholos Sub-Basin inferred from new and re-processed seismic data is similar to the depth in an existing model of basement for this region (OZ-SEEBASE, FrOG Tech, 2005) (Figure 4-4c). This is also true for the Zeewyck Sub-basin, although the OZ-SEEBASE dataset suggests that sediments extend beyond the continent–ocean boundary. Basement depth over the Turtle Dove Ridge is shallower in the OZ-SEEBASE dataset than in the interpretation of more recent seismic data (Jones *et al.*, 2011, Bernardel and Nicholson, 2013).

4.2.4 Densities

We modelled Bouguer gravity using the densities outlined in Table 1. Sediment density was defined differently above and below the Top Permian horizon. The deeper Permian sedimentary layer was assigned a constant density of 2650 kg/m^3 . The density of the post-Permian sediments increased exponentially with depth from 2200 kg/m^3 to 2650 kg/m^3 . This is an appropriate first-order approximation for a general density gradient in sedimentary basins (Bahr *et al.*, 2001). Density information for the sediments is available from several borehole logs (Batavia-1, Cliff Head-1/2/6, Fiddich-1, Flying Foam-1, Frankland-2, Geelvink-1A, Hadda-1, Leander Reef-1, Livet-1, Moondah-1, Morangie-1, Twin Lions-1, Vindarra-1, see stars in Figure 4-1a). The boreholes do not extend to the full depth of the model, but the borehole logs indicate a density of about 2600 kg/m^3 at a depth of about 2000 m. The calculation of porosity profiles was made using the formula provided by Athy (1930). For deeper sediments (>8000 m) the porosity is less than 1%. Therefore, we assumed that the deeper sediments have a constant density of 2650 kg/m^3 , which is equivalent to the grain density of quartz (Sclater and Christie, 1980).

A constant crustal density of 2800 kg/m^3 was used, which is roughly representative of the global average crustal density of 2830 kg/m^3 (Christensen and Mooney, 1995). It is likely that the density of the crust changes through the transition zone between oceanic and continental crust, so a denser crust (2900 kg/m^3) is modelled seaward of the continent–ocean boundary. The mantle was assigned a density of 3300 kg/m^3 . This mantle density was also used in the computation of a Moho model for the Australian region using gravity inversion (Aitken, 2010). Our choice of crust and mantle density results in a large density contrast at the Moho (500 kg/m^3), but we tested different values for density, including a crustal density that increased linearly with depth, and found only minimal differences in computed gravity.

Modelled structure	Density [kg/m^3]
Water	1030
Post-Permian Sediments	2200–2650*
Permian Sediments	2650
Crust	2800
Mantle	3300

Table 4-1: Density values used for modelling and isostatic calculations. For local isostatic calculation of Moho depth, a compensation depth of 32 km was chosen. * A mean density of 2570 kg/m^3 was used for local isostatic computations

4.2.5 Crustal Thickness

Given the uncertainty in the thickness of the sediments and the intricate link between the gravity signature of Moho and sediments (as a result of isostatic compensation or flexural loading), it is crucial in this area to consider the nature of the Moho. However, Moho depths along the southwestern Australian margin are very poorly constrained (Figure 4-5). The most recent seismological Moho model for the Australian region is AusMoho (Figure 4-5a, b) (Kennett *et al.*, 2011), but this model is very poorly constrained on the southwest margin of Australia where only a few refraction or receiver function observations of Moho depth are available (Figure 4-5a) (cf. Clitheroe *et al.*, 2000, Collins *et al.*, 2003, Dentith *et al.*, 2000, Francis and Raitt, 1967). An earlier compilation of seismological Moho depths has also been used in a continent-wide gravity inversion to generate the “MoGGIE” crustal model for the Australian region (Aitken, 2010) (Figure 4-5d).

Given the limited constraints on Moho depth, we considered two options for inferring crustal thickness in the 3D gravity models. The first involved making a simple local isostatic assumption and computing the Moho that compensates for water depth and sediment thickness variations (Figure 4-5c). Thus, we calculated the crustal load by including water (topography onshore) and sediments (see Table 1 for parameters). This is more realistic than taking only bathymetry into account, because it considers the density distribution of the whole upper crust.

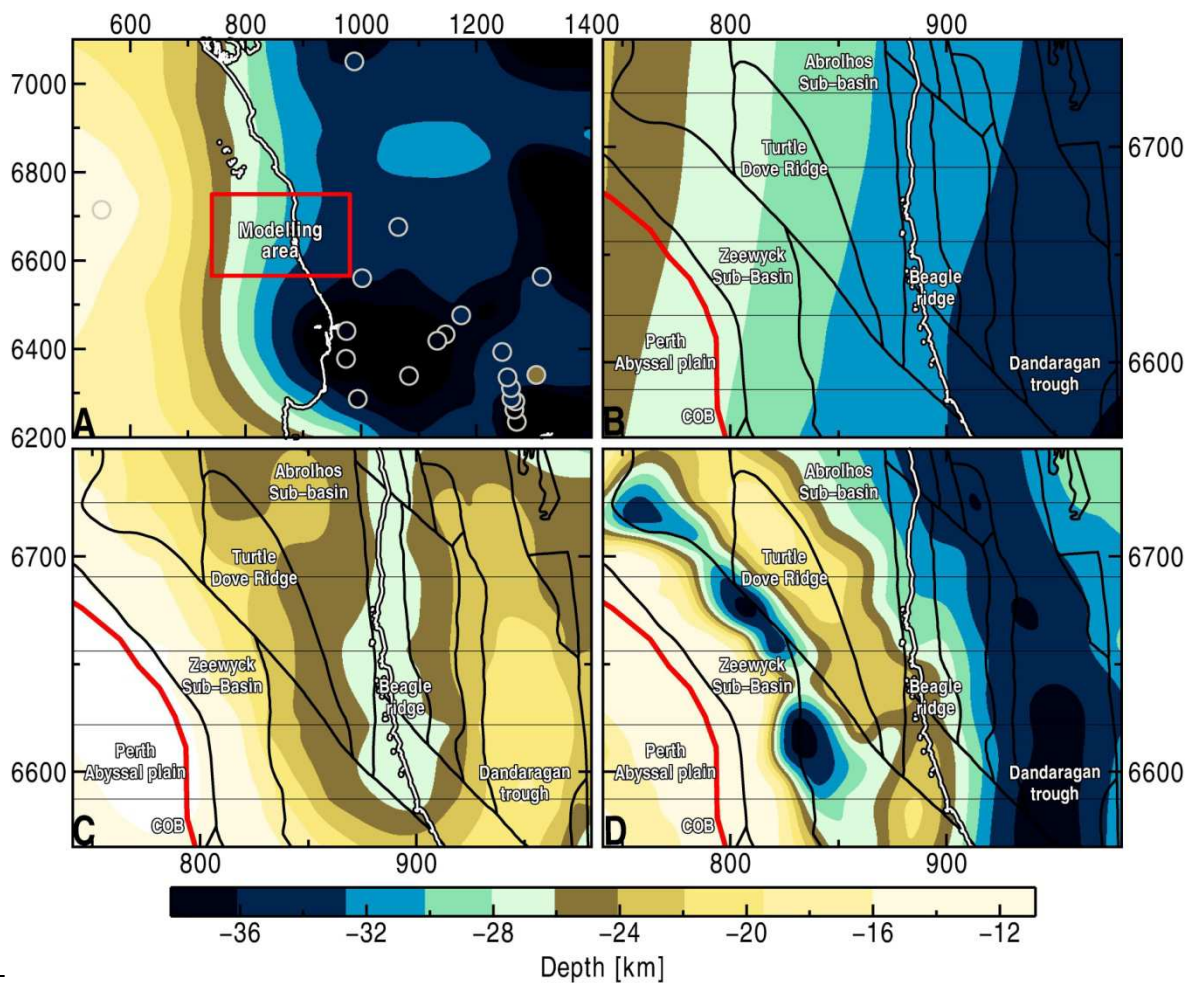


Figure 4-5: Maps showing the different Moho estimates in this area. (a) AusMoho surface from Kennett *et al.* (2011) over a larger area showing the data points that are used to constrain the model (circles). The red rectangle shows the area represented in b–d. (b) AusMoho in our modelling area. (c) Moho depth computed by assuming local isostatic balance of bathymetric and sedimentary loads. (d) The seismologically-constrained gravity inversion Moho model (MoGGIE) from Aitken (2010). Map projection is UTM Zone 49 South.

Our second model incorporates the “MoGGIE” continent-wide Moho model (Aitken, 2010) (Figure 4-5d). This Moho model is derived from a gravity inversion constrained using OZ-SEEBASE sediment thickness (FrOG Tech, 2005) (Figure 4-4c) and essentially the same seismological estimates of Moho thickness used for AusMoho (i.e. also with limited constraints off southwestern Australia). The inversion to generate the MoGGIE Moho is based on a six-layer model in which densities and the geometry of the model were iteratively varied in order to achieve the best fit to gravity data.

4.3 Modelling strategy

The 3D forward gravity modelling was conducted using the IGMAS+ software (Schmidt *et al.*, 2011, Götze and Lahmeyer, 1988), a package that is well suited to incorporating constraining information as a guide to developing a plausible model. For this study, the 3D representation of the subsurface is achieved by defining geometry on a series of parallel 2D sections that cover the area of interest. The 3D geometry is achieved by triangulating between common interfaces on adjacent sections. The program calculates the exact 3D gravity response on the basis of the triangulated surfaces that define each body and a density, or density gradient, assigned to the bodies (Götze and Lahmeyer, 1988, Schmidt *et al.*, 2011). The calculated gravity response of the model is then compared to the measured gravity.

The inherent non-uniqueness of the inversion of potential field data requires additional constraints during the setup of a model. Misfits between measured and calculated gravity can be reduced by changing geometry and density of the model. If no "hard" constraints are available (e.g. geometry from seismic reflectors), physical or geological assumptions need to be considered and included in the model (e.g. expected geometry based on isostatic assumptions or the tectonic evolution of the area (cf. (Köther, 2009)). In our modelling, ambiguity was reduced by considering two hypotheses about the isostatic state of the area.

We initially set up two models that each incorporated the same sedimentary layers constrained by the interpretation of seismic reflection data, but with the two different choices of Moho outlined in the previous section. By analysing the parts of these initial models where measured and calculated gravity do not fit, we made minor adjustments to the geometry of the model that lead to an improved fit.

After generating a forward model that satisfactorily fit the measured gravity field, we also estimated the effective elastic thickness for the model region. The resulting estimate of variations in flexural rigidity aids interpretation of the crustal structure and evolution of the northern Perth Basin.

The 3D forward model is based on five east–west sections with an average separation of 34.5 km. These sections are used to define the model geometry in the area of interest. Overall, the model comprises ten sections, including sections well beyond the area of interest that are used to reduce edge effects. The horizons from the seismic interpretation and Moho depth were imported into IGMAS+ and triangulated to generate the 3D surfaces shown in Figure 4-4.

4.4 Results

We present the results of our models as maps and sections. We show maps of calculated and residual gravity to illustrate the fit for the entire 3D density model (Figure 4-6). We also present a detailed analysis along two sections through the model (marked in red in Figure 4-4 and Figure 4-6). These sections were selected because they are located in the areas of the largest misfit in the

unmodified initial models and because they cover all the major geological elements in this part of the northern Perth Basin.

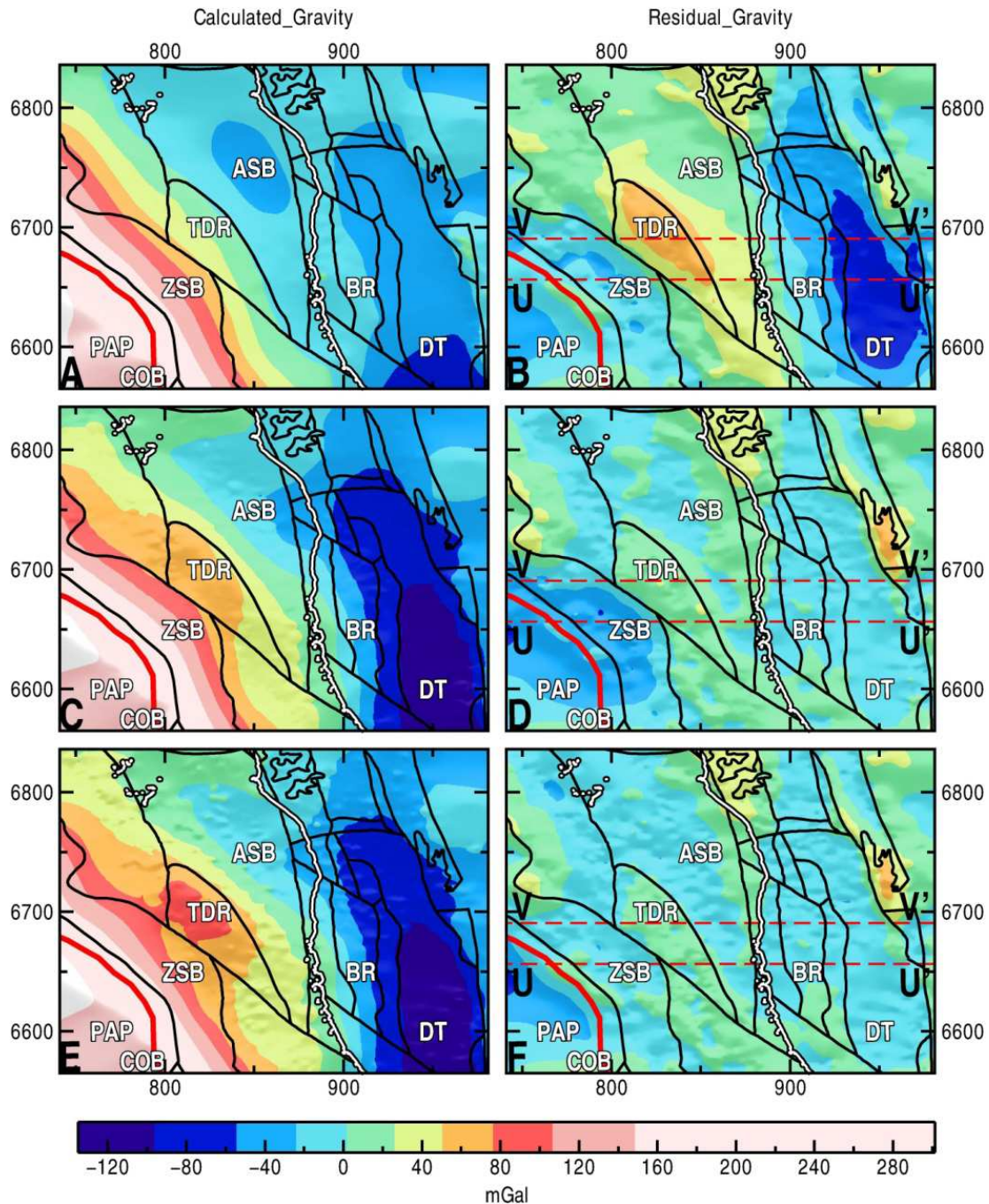


Figure 4-6: Map views of calculated and residual (measured minus calculated) gravity for all three gravity models. (a), (c) and (e) show the calculated gravity, (b), (d) and (f) show the residual gravity anomalies. (a) and (b) are for Model 1 incorporating a Moho defined by local isostasy, (c) and (d) for Model 2 incorporating the MoGGIE Moho (Aitken, 2010), (e) and (f) are for the adjusted version of Model 2. Red dashed lines labelled U and V mark the cross-sections through the model shown in Figs 6–9. The black lines outline the main crustal elements, as described in Fig. 1. Map projection is UTM Zone 49 South.

4.4.1 Model 1: Moho defined by local isostasy

Model 1 incorporates the sediment body defined by the horizons illustrated in Figure 4-4a and b and the Moho calculated assuming local isostatic compensation (Figure 4-5c). In this model, local isostatic balance is maintained by shallower Moho beneath the regions with the thickest low-density sediments (i.e. reduced load).

Figure 4-6b shows residual gravity for Model 1, the difference between measured (Figure 4-3a) and calculated gravity (Figure 4-6a). The calculated gravity for Model 1 does not reproduce many of the high-frequency features evident in the measured gravity field, but the regionally-decreasing gravity gradient from southwest to northeast shows up quite well. In the northeast parts of the model, onshore, a weak correlation with the negative anomaly of the Dandaragan Trough is evident. The anomalies caused by the Zeewyck Sub-basin, Turtle Dove Ridge and Dandaragan Trough are not reproduced by the model. The misfit between measured and calculated gravity varies between 100 and $-120 \times 10^{-5} \frac{m}{s^2}$ (Figure 4-6b). The largest misfits are located in the Dandaragan Trough ($-120 \times 10^{-5} \frac{m}{s^2}$) and over the Turtle Dove Ridge ($80 \times 10^{-5} \frac{m}{s^2}$).

Figure 4-7b shows vertical section U through Model 1. The crust is thinner under the deep sedimentary basins (Dandaragan Trough and Zeewyck Sub-basin) as a result of local isostatic compensation. The thinner sediments over the Turtle Dove and Beagle ridges mean that the crustal thickness is greater than in adjacent areas. On this section, the large misfit between measured (black line in Figure 4-7a) and calculated gravity (red dashed line in Figure 4-7a) associated with the Dandaragan Trough is evident. Due to the thinner crust (Moho depth of about 25 km), the calculated gravity is much higher than observed ($+100 \times 10^{-5} \frac{m}{s^2}$). The relative gravity high associated with the Turtle Dove Ridge is also not evident. The misfit here ($\sim 80 \times 10^{-5} \frac{m}{s^2}$) is the result of the generally small variations in Moho depth. The relative gravity low associated with the Zeewyck Sub-basin does not show up in the calculated gravity field. The misfit in this area is about $20 \times 10^{-5} \frac{m}{s^2}$.

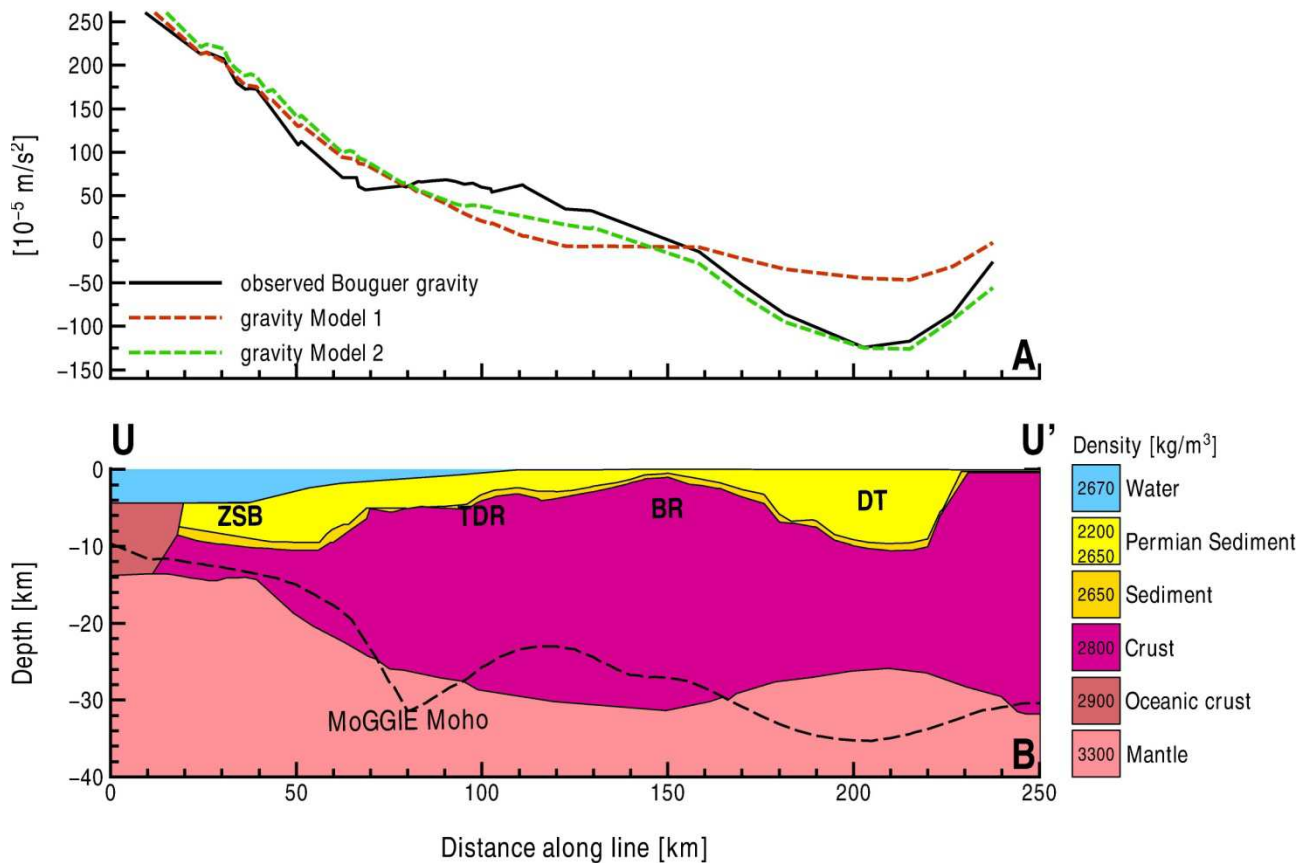


Figure 4-7: (a) Measured (black solid line) and calculated (coloured dashed lines) gravity profiles for Models 1 and 2 along section U (see Figure 4-6b for location). (b) Section U through Model 1 (local isostatic Moho). The dashed line shows the Moho from Model 2 (MoGGIE Moho).

Figure 4-8b shows vertical section V through Model 1. The fit between observed and calculated gravity towards the continent–ocean boundary and over the Zeewyck Sub-basin is better than for section U. However, to the east over the Beagle Ridge and Turtle Dove Ridge, the sign of the calculated gravity field is almost opposite to the sign of measured gravity. Here, the misfit is also about $100 \times 10^{-5} \frac{m}{s^2}$. Over the Dandaragan Trough, the negative measured gravity caused by the sedimentary basin is completely compensated by the high-density mantle under thinned crust, which leads to a misfit of about $100 \times 10^{-5} \frac{m}{s^2}$.

The large misfits between measured and calculated gravity for Model 1 imply that the gravity field associated with this part of the northern Perth Basin cannot be explained by a model incorporating local isostatic balance of sediments.

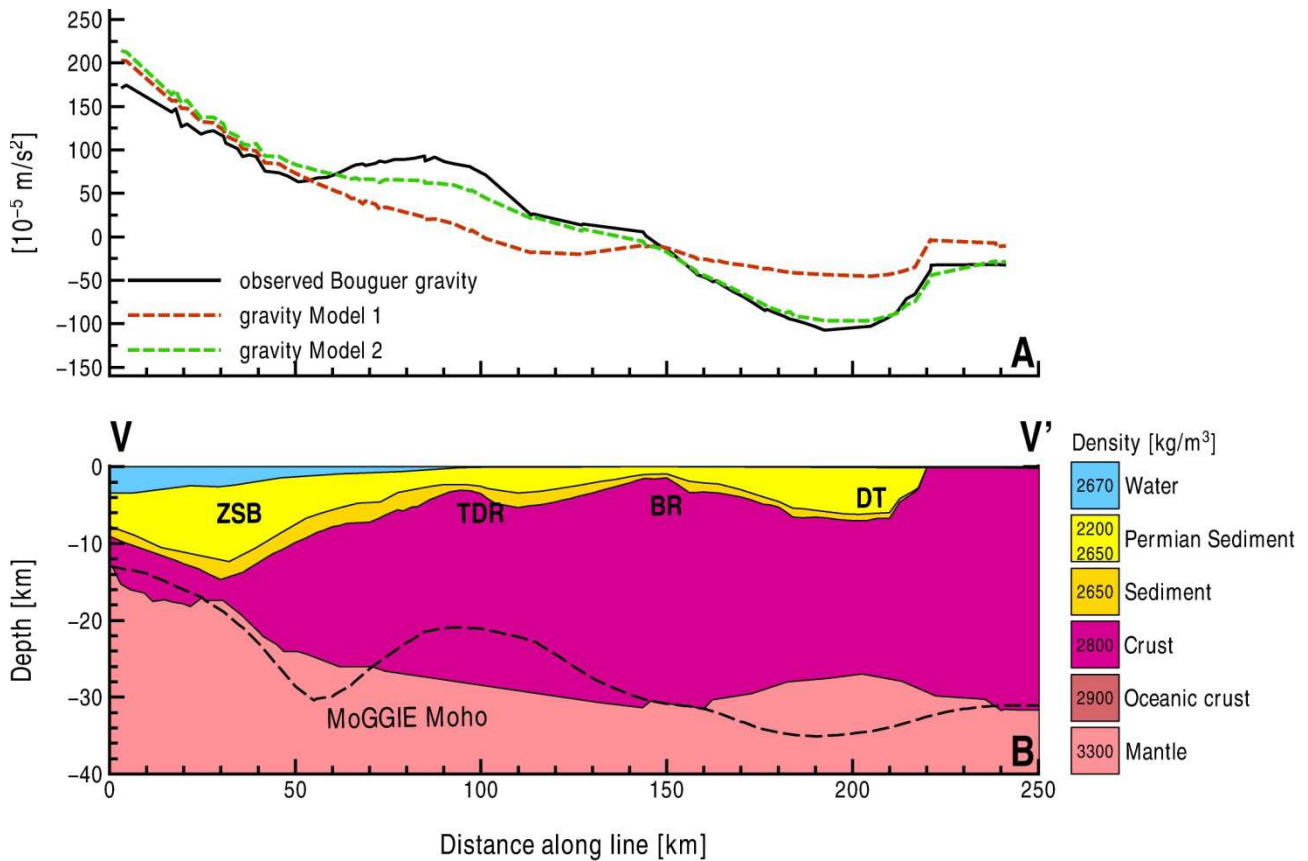


Figure 4-8: (a) Measured (black solid line) and calculated (coloured dashed lines) gravity profiles for Models 1 and 2 along section V (see Figure 4-6b for location). (b) Section V through Model 1 (local isostatic Moho). The dashed line shows the shape of the MoGGIE Moho in Model 2.

4.4.2 Model 2: MoGGIE Moho

Model 2 uses the same sediment bodies as Model 1, but instead incorporates the MoGGIE Moho from Aitken (2010). Because the MoGGIE Moho was derived from a continent-wide gravity inversion that incorporated sediments with a similar thickness to those used here (i.e. OZ-SEEBASE, FrOG Tech, 2005), an improved fit between measured and calculated gravity for Model 2 is to be expected. Remaining misfits between measured and calculated gravity largely reflect the use of an alternative interpretation of the sedimentary layers (as shown in Figure 4-4).

Figure 4-6c and d shows maps of calculated and residual gravity for Model 2. The calculated gravity for Model 2 shows a much better fit than for Model 1. The gravity signature of the Dandaragan Trough is reproduced very well, other than in the southeast where the computed anomaly is more negative than the measured signal. Larger misfits to the east of the Darling Fault reflect the fact that the detailed geology of the Yilgarn Craton was not included in the model. Model 2 also partially reproduces the gravity high of the Turtle Dove Ridge. The amplitude of the modelled Turtle Dove Ridge anomaly is lower than the measured anomaly by no more than about $30 \times 10^{-5} \frac{m}{s^2}$. The relative negative anomaly related to the Abrolhos Sub-basin is also reproduced well, but the measured anomaly gradient associated with the Zeewyck Sub-basin is different to the

gradient evident in the calculated gravity. The calculated gravity in this area is higher than measured, with a maximum misfit of about $-40 \times 10^{-5} \frac{m}{s^2}$.

The dashed line in Figure 6b shows the Moho on section U through Model 2. Compared to Model 1, the crustal thickness is significantly greater under the Dandaragan Trough. The Moho depth decreases towards the Beagle Ridge, but overall the thickness of the crystalline crust from the Dandaragan Trough to the Beagle Ridge remains relatively constant at about 26 km. The Moho is relatively shallow beneath the Turtle Dove Ridge (~20 km) and its geometry is consistent with deep-crustal (possibly Moho) reflectors in seismic data that dip away from the axis of the ridge (Bernardel and Nicholson, 2013, Hall *et al.*, in press). Between the Turtle Dove Ridge and the Zeewyck Sub-basin, there is a steep deepening of the Moho to about 30 km over a distance of about 40 km. This deeper Moho feature is characteristic of much of the eastern flank of the Zeewyck Sub-basin (Figure 4-5d).

To the west of the Beagle Ridge, there are two shorter-wavelength anomaly features that do not show up well in the modelled gravity. Over the Zeewyck Sub-basin, the modelled gravity is about $20 \times 10^{-5} \frac{m}{s^2}$ too high (i.e. too much mass in the model), whereas over the Turtle Dove Ridge, the modelled gravity is $10-20 \times 10^{-5} \frac{m}{s^2}$ too low (i.e. not enough mass in the model). Similar relationships between measured and calculated gravity are evident on Profile V (Figure 4-8).

4.4.3 Adjusted MoGGIE model

In this section, we describe a modified model that leads to an improved fit between measured and calculated gravity (Figure 4-6e and f, Figure 4-9 and Figure 4-10). The modifications were made to Model 2 that incorporates the MoGGIE Moho. Given the lack of direct constraints in some areas, these adjustments are kept to a minimum and are only applied in the areas of substantial misfit outlined in the previous section.

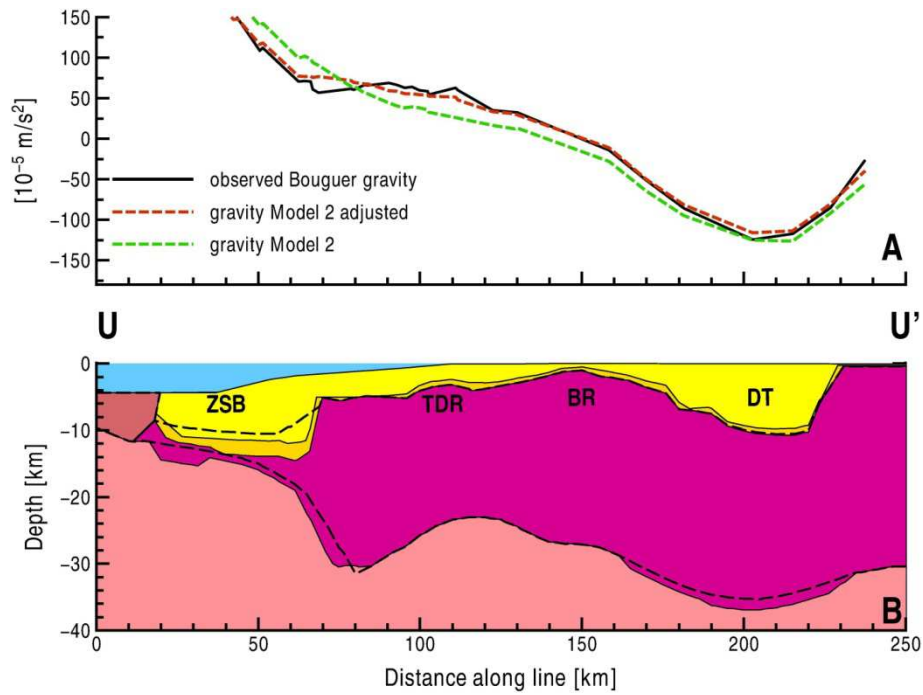


Figure 4-9: Section U–U' showing through the adjusted version of Model 2 (see Figure 4-6f for location). (a) Measured (coloured black line) and calculated (dashed lines) gravity profiles. (b) Model 2 geometry after the adjustments described in the text. Dashed lines show the geometry from the initial version of Model 2.

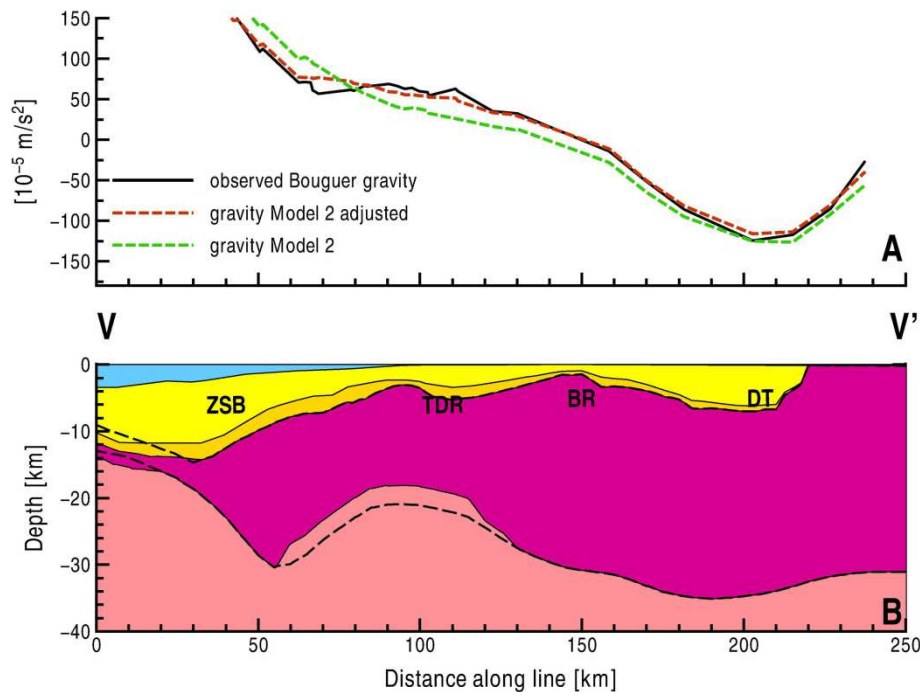


Figure 4-10: Section V–V' through showing Model 2 before and after adjustment (see Figure 4-6f for location). (a) Measured (black line) and calculated (coloured dashed lines) gravity profiles. (b) Model 2 after the adjustments described in the text. Dashed lines show the geometry from the initial version of Model 2.

To account for the misfit between measured and calculated gravity over the Turtle Dove Ridge, we have added additional mass to the MoGGIE model by decreasing the depth to the Moho in parts of the model (Figure 4-10). The fit could also be improved by reducing the thickness of sediments over the Turtle Dove Ridge. However, to achieve a good fit, the sediment thickness must be reduced to almost zero, which is not consistent with available constraints (Jones *et al.*, 2011).

To achieve the reduction in mass required to match measured and calculated gravity associated with the Zeewyck Sub-basin, we have increased both the Moho depth and the sediment thickness. Johnston and Petkovic (2012) also suggest deeper sediments in the Zeewyck Sub-basin. The choice to modify both reflects the uncertainty in crustal geometry in this poorly-constrained region. On section U, we changed the depth of the sediments by about 3 km in the area of Zeewyck Sub-basin and deepened the Moho by about 2 km. As a result, the Zeewyck Sub-basin is modelled as a deep, steep sided depocentre. Given the lack of constraints on the thickness of sediments in the Zeewyck Sub-basin and the uncertainty in Moho depths derived from the MoGGIE model (± 5 km), these adjustments are permissible and provide an interpretation that can be tested by future data acquisition.

To refine the fit between measured and calculated gravity over the Beagle Ridge, Turtle Dove Ridge and Dandaragan Trough, we also made minor modifications to the Moho depth in some areas. The shallowing of the Moho by 3–4 km under the Turtle Dove Ridge (Figure 4-10) and the deepening of the Moho by no more than 2 km under the Dandaragan Trough (Figure 4-9) is within the uncertainty associated with Moho depths from the MoGGIE model (± 5 km).

Figure 4-6e and f show the overall fit for the adjusted version of Model 2 and Figure 4-11 shows maps of the Top Basement and Moho in this final model. In particular, the regions of the Zeewyck Sub-basin and the Turtle Dove Ridge feature an improved fit. Overall, because only small adjustments were made to the initial model, the calculated field for the adjusted model does not differ greatly from the gravity calculated for Model 2.

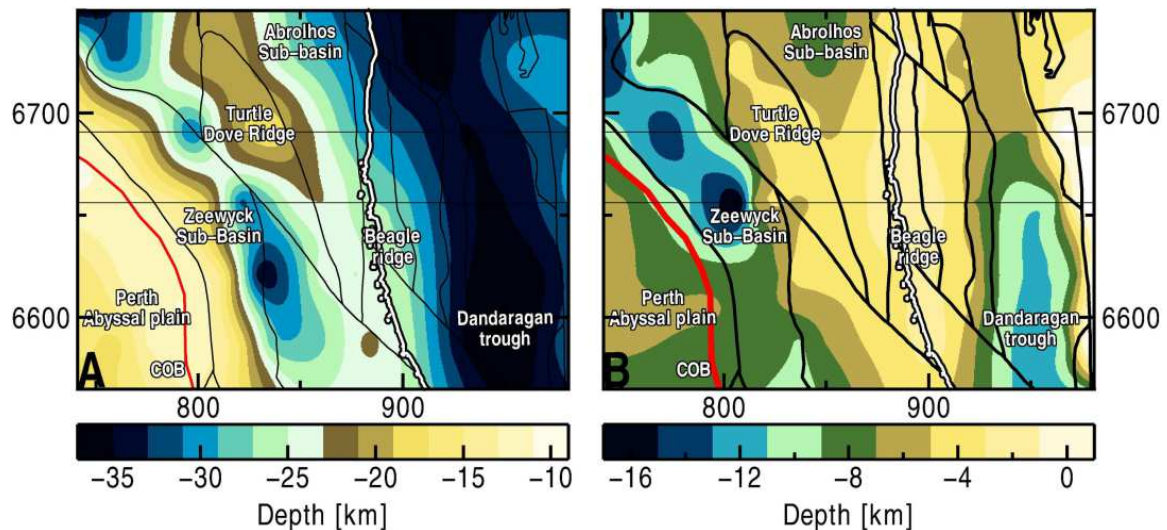


Figure 4-11: (a) Moho and (b) Top Basement maps from the adjusted version of Model 2. East-west black lines mark the cross-sections through the model shown in Figure 4-7 to 10. The black lines outline the main crustal elements, as described in Figure 4-2. Map projection is UTM Zone 49 South.

The variations in Moho depth that we infer in our adjusted model are consistent with 2D gravity models described by Petkovic (2012). He used the MoGGIE Moho in an initial model and then modified the model arbitrarily to achieve a fit between measured and calculated gravity along the profiles. Compared to our model, Petkovic's results imply that the Moho under the sedimentary basins is significantly deeper than in the MoGGIE model (e.g. 8 km deeper under the Zeewyck Sub-basin). This dramatic increase in Moho depth compared to the MoGGIE model is not necessary in our 3D models, but our results imply similar changes in Moho depth over short horizontal distances.

4.4.4 Inversion for flexural rigidity

The previous sections showed that measured gravity in this part of the northern Perth Basin cannot be explained by simple local isostasy. The deeper Moho under the sedimentary basins in Model 2 has implications for the isostatic mechanism applicable to this area. In order to further examine the isostatic state and to provide a context for discussing the implications of the 3D density model, we computed the distribution of effective elastic thickness.

Effective elastic thickness (T_e) is a quantity that parameterises lithospheric flexural rigidity, a measure of the strength of the lithosphere. Where T_e is low, the lithosphere is weak and isostatic balance tends to local (Airy) compensation of loads. When T_e is high, the lithosphere is stronger (rigid) and flexural support of loads dominates.

We inverted for T_e using the convolution approach described by Braitenberg et al. (2002). Using this approach, T_e was estimated iteratively in a 30×30 km moving window. For each window, a Moho depth is computed as compensation for combined bathymetric/topographic and sediment loads using T_e values in the range 1–70 km. The chosen T_e for each window is the value that gives the minimum root mean square misfit between the Moho computed during the inversion and the Moho from the adjusted version of Model 2.

Figure 4-12 shows the results of the T_e inversion. The misfit between the adjusted Model 2 Moho and the Moho resulting from the inversion generally lies within the range ± 5 km, but reaches up to 10 km on the eastern flank of the Zeewyck Sub-basin where the MoGGIE model contains an elongate band of relatively deep Moho (Figure 4-5d). This level of misfit is consistent with the level of error in the MoGGIE Moho used in Model 2 (± 5 km, Aitken, 2010).

Computed T_e values are near zero in the Zeewyck Sub-basin and towards the Perth Abyssal plain. The Turtle Dove Ridge is associated with very high T_e (up to 70 km), while T_e in the Abrolhos Sub-basin is higher than for the Zeewyck Sub-basin (20–30 km). Towards the Dandaragan Trough, T_e is about 10–20 km. In the northeast of the model area over the Yilgarn Craton, T_e values reach 70 km.

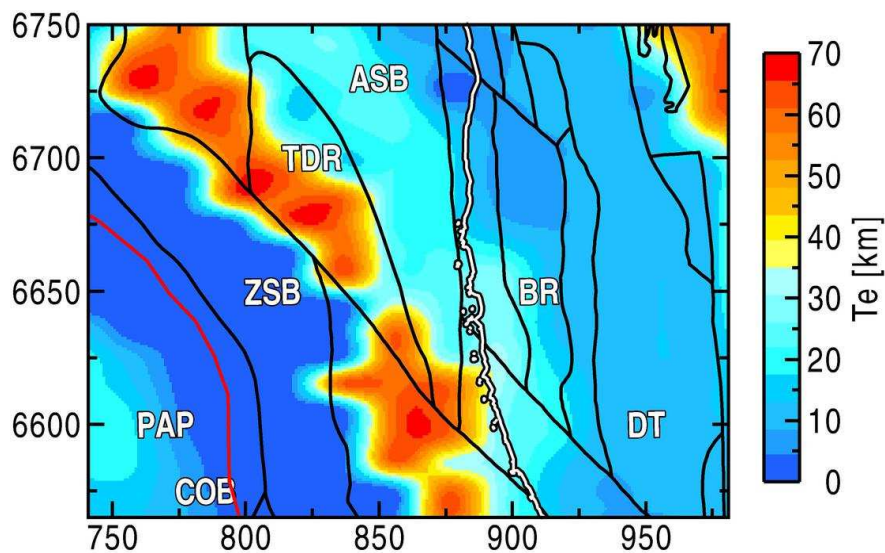


Figure 4-12: Map showing results of the inversion for effective elastic thickness (T_e). The map shows low T_e (weak lithosphere) associated with the Zeewyck Sub-basin, very high T_e along the Turtle Dove Ridge and moderate T_e for the Abrolhos Sub-basin, Beagle Ridge and Dandaragan Trough. The black lines outline the main structural elements and the red line marks the continent–ocean boundary (as described in Figure 4-2). Map projection is UTM Zone 49 South.

4.5 Discussion

The results of our initial modelling of the northern Perth Basin (Figure 4-6 to 8) show that a model incorporating a local isostatic Moho (Model 1) explains the measured gravity field only for few parts of the model. Using the MoGGIE Moho (Model 2) leads to a better fit, but the parts of Model 2 that do not fit help to identify areas where interpretation of basin geometry and crustal structure need to be better constrained or revised. Below we outline possible reasons for the misfits between measured and calculated gravity and discuss the implications of the modelling for the crustal structure and tectonic evolution of the northern Perth Basin.

4.5.1 Dandaragan Trough

Under the Dandaragan Trough, the MoGGIE model (Model 2) is characterised by deeper Moho and a crystalline crust that has a relatively constant thickness (~25 km) between the Darling Fault and the Beagle Ridge. This configuration reproduces the measured gravity field well and is consistent with the interpretation of Iasky et al. (1991), who also suggested an increased Moho depth of about 30 km beneath the Dandaragan Trough.

We interpret the deeper Moho and roughly constant thickness of sub-sediment crust beneath the Dandaragan Trough to be the result of crustal-scale tilting about a pivot point near the Beagle Ridge. This tilting leads to normal displacement on a steeply west-dipping Darling Fault (Figure 4-13).

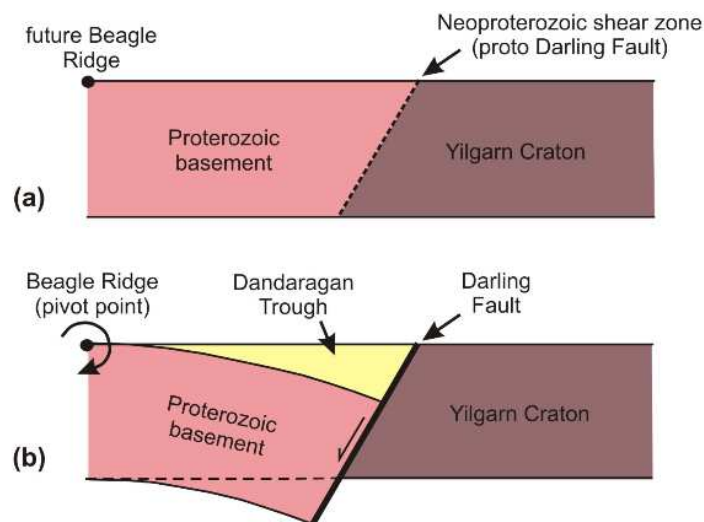


Figure 4-13: Schematic diagram based on the Model 2 illustrating crustal-scale regional block tilting to form the Dandaragan Trough. (a) Initial configuration. (b) Configuration after crustal-scale block tilting about a pivot point at the Beagle Ridge that results in normal movement on the steeply west-dipping Darling Fault.

This conceptual model implies that the Darling Fault is a crustal-scale fault that extends to the base of the crust. Evidence for the deep nature of the Darling Fault is limited to two seismic

reflection profiles that cross the fault in the southwestern corner of the model area (Dentith *et al.*, 1993). Reflections from the fault plane itself and the termination of reflectors in the Dandaragan Trough that dip toward the Darling Fault define the fault as a steeply west-dipping structure that extends to depths of at least 6 seconds two-way time (~ 20 km). Dentith *et al.* (1993) also suggest that the associated proto-Darling Fault, an older, pre-cursor structure to the Darling Fault, is a sub-vertical structure that extends to the base of the crust. These interpretations are consistent with the conceptual model illustrated in Figure 4-13.

Crustal block rotation on the Darling Fault is also consistent with the moderate T_e values associated with the Dandaragan Trough (Figure 4-12). These values suggest that the lithosphere here has considerable strength ($T_e = 10\text{--}20$ km), so the crust is likely to respond as a coherent block in response to the extensional events that lead to the formation of the Perth Basin.

4.5.2 Beagle Ridge and Abrolhos Sub-basin

In Model 2, the fit between measured and calculated gravity in the vicinity of the Abrolhos Sub-basin and Beagle Ridge is reasonable, which suggests that, as in the Dandaragan Trough, the geometry in this part of the model is generally sufficiently constrained and plausible. T_e values are similar to those associated with the Dandaragan Trough.

4.5.3 Turtle Dove Ridge

Measured gravity over the Turtle Dove Ridge is characterised by a relative gravity high (more than $10 \times 10^{-5} \frac{m}{s^2}$ greater than adjacent areas) and is fit better by the shallow Moho of the MoGGIE model (Model 2) than by the deep Moho of the local isostatic model (Model 1) (Figs 5–7). The differences in calculated gravity for these two models reflect large difference in Moho depth beneath the Turtle Dove Ridge (up to about 8 km deeper in the local isostatic model).

Despite the improved fit between measured and calculated gravity in Model 2 (MoGGIE model; misfit reduced by about $20 \times 10^{-5} \frac{m}{s^2}$), the difference between measured and calculated gravity is still up to about $25 \times 10^{-5} \frac{m}{s^2}$. Accounting for this difference requires additional mass in the vicinity of the Turtle Dove Ridge. This additional mass could be included by decreasing the Moho depth by 2–3 km or by reducing the thickness of low-density sediments over the Turtle Dove Ridge by several kilometres. Given the available constraints, reducing the crustal thickness is allowable, but substantial reductions in the thickness of sediments would not be consistent with the interpretation of seismic reflection data (cf. Jones *et al.*, 2011, Hall *et al.*, in press). Variations in basement, crustal or mantle density could also be invoked to add the required mass, though such variations would not be constrained.

The Turtle Dove Ridge and areas along strike to the northwest and south are associated with T_e values of almost 70 km. This suggests that the basement high that forms the Turtle Dove Ridge reflects the presence of an extremely rigid block wedged between the inboard and outboard parts

of the northern Perth Basin. Rather than explaining the misfit between measured and calculated gravity by increased mass related to shallower Moho, the high T_e might be an indication that the additional mass required in the model could be achieved through the presence of high-density, rigid material within or immediately below the crust.

4.5.4 Zeewyck Sub-basin

Explaining the misfit between measured and calculated anomalies over the Zeewyck Sub-basin is more difficult than for other areas. Sediment thickness in the Zeewyck Sub-basin is not well constrained by seismic data (Bernardel and Nicholson, 2013, Jones *et al.*, 2011, Hall *et al.*, in press) and neither the MoGGIE nor the local isostatic model provide a satisfactory fit. Interestingly, the Moho depth in both models is similar in the western part of the Zeewyck Sub-basin and through the continent–ocean transition zone to the Perth Abyssal Plain (Figure 4-7 and 8). There, the fit is reasonable (maximum misfit less than $5 \times 10^{-5} \frac{m}{s^2}$), but the calculated gravity is slightly greater than the measured gravity.

To the east of the Zeewyck Sub-basin, the difference in Moho depth in Models 1 and 2 is up to 6 km (Figure 4-7 and 8). The calculated gravity is generally higher than observed over the Zeewyck Sub-basin, especially on profile U (Figure 4-7). Thus, the adjustments to the model required to improve the fit need to involve a reduction in mass. This mass reduction could be achieved by increasing the thickness of the already-thick sediments, or by increasing the crustal thickness. Lateral changes in basement, crustal or mantle density cannot be ruled out, especially given that the proximity of the Zeewyck Sub-basin to the continent–ocean boundary means that factors like upper mantle serpentinisation or magmatic underplating might influence subsurface mass distribution.

The 2.5D forward magnetic modelling conducted by Johnston and Petkovic (2012) suggests that strongly magnetised magmatic bodies could exist in the deeper parts of the sub-basin. However, adding such bodies to the 3D density model would impart an increase in mass and would not, therefore, help to account for the excess mass in Model 2 that leads to the misfit between measured and calculated gravity over the Zeewyck Sub-basin.

In the adjusted version of Model 2 (Figure 4-6e, f, Figure 4-9 and Figure 4-10), the Zeewyck Sub-basin is characterised by steep edges, thick sediments and large changes in crustal thickness over short distances. These features are characteristic of transtensional basins (e.g. Antobreh *et al.*, 2009, Bird, 2001, Greenroyd *et al.*, 2007, Parsieglia *et al.*, 2009) and a transtensional origin for the Zeewyck Sub-basin is implied by the interpretation of seismic reflection data and studies of the tectonic evolution of the southwest margin of Australia (Bernardel and Nicholson, 2013, Hall *et al.*, in press). A transtensional origin for the Zeewyck Sub-basin is also consistent with the near-zero T_e associated with the sub-basin (Figure 4-13). The lithosphere associated with transtensional basins would be weakened by the predominance of strike-slip faults that tend to penetrate to large depths. If these strike-slip faults penetrate beyond the crust, then serpentinisation of the mantle is

possible. The associated reduction in mantle density could help to explain the reduced mass required in this part of the model to achieve a fit between measured and calculated gravity.

4.6 Conclusions and outlook

3D density modelling and analysis of the isostatic state of the northern Perth Basin show differences in the crustal structure and effective elastic thickness associated with the different structural elements of the basin. The area lacks the constraints that would allow a reliable interpretation of Moho depth, which requires the testing of various assumptions on the isostatic state of the area. We have shown that a model in which the Moho was inferred under the assumption of local isostatic balance of bathymetric and sedimentary loads does not explain measured gravity everywhere over the basin. In contrast, a model that incorporates modifications to a pre-existing Moho model derived from continent-wide inversion of gravity data can explain the gravity anomalies over the basin.

The adjusted 3D density model incorporating the MoGGIE Moho suggests that the negative gravity anomaly associated with the Dandaragan Trough is not only caused by the deep sedimentary infill (>12 km), but also by a deep Moho. Unlike a model incorporating stretched and thinned crust (i.e. local isostatic model), a model with crustal-scale rigid block rotation on a steeply west-dipping Darling Fault can explain the dominantly negative gravity anomalies over the Dandaragan Trough. Crustal-scale rigid block faulting is consistent with the moderately-high T_e values (10–20 km) inferred for the onshore and inboard parts of the northern Perth Basin.

The modelled distribution of effective elastic thickness also shows that the crust below the poorly-constrained Zeewyck Sub-basin is significantly weaker than the crust of the Turtle Dove Ridge and Dandaragan Trough. This weakness can be explained by the presence of deep-penetrating strike-slip faults that may have facilitated serpentinisation of the upper mantle. A weak transtensional Zeewyck Sub-basin is also consistent with the steep edges, thick sediments and the large lateral variations in Moho depth over short distances that are evident in the 3D density model.

Crustal-scale rigid block faulting is consistent with the moderately-high T_e values (15–25 km) inferred for the onshore and inboard parts of the northern Perth Basin.

4.7 Applicability of satellite data at a passive continental margin

Chapter 2.4.3 discussed the spatial resolution of different satellite gravity models and the resolution of lithospheric structures for 3D density models. The models in the previous chapters

were set up with ground based gravity data. The models feature the crust-mantle boundary, the crust-ocean boundary and the sedimentary basins located in this area. The interpretation focused on the isostatic state of the area and the depth and geometry of the basins. According to chapter 2.4.3, this chapter assesses the applicability of GOCE satellite gravity data in this area. For this purpose, a Bouguer anomaly was compiled on the basis of the satellite only model GOCO-03S (Mayer-Gürr, 2012). This gravity field was compared to calculated gravity from the final 3D density model (Model 2, cf. 4.4.3). Figure 4-14 shows the Bouguer gravity anomaly of GOCO-03S. The wavelengths of the anomalies are about 100 km. The high positive anomaly over the Perth Abyssal plain ($250 * 10^{-5} \frac{m}{s^2}$) shows up, as well as the gravity low onshore associated to the Dandaragan trough ($-60 * 10^{-5} \frac{m}{s^2}$). Anomalies caused by the Zeewyck Sub-basin and the basement high over Turtle Dove ridge are not highlighted by the measurements.

Therefore, Model 2 was modified to a simple two layer model only comprising crust (oceanic and continental) and mantle (density contrast 500 kg/m^3). Figure 4-15 shows the calculated gravity of the new model.

The calculated gravity correlated with the satellite gravity observations. Thus, the measured signal reflects mainly the deep density contrast located at the Moho. The residual gravity map (Figure 4-16) highlights the misfits of calculated and measured gravity. Positive deviations imply too much mass included in the model. In the area of the Sub-basins and the Dandaragan trough positive residual anomalies show up. These point to less mass in this area which can be explained with sedimentary infill. However, the anomalies caused by the sediments are higher and cannot be included in the satellite only density model.

Finally, the comparison confirms the conclusions from chapter 2.4.3. The anomalies observed by the GOCE satellite are appropriate to reflect deep lithospheric structures. In chapter 2.4.3 the long wavelengths caused by the subduction zone are highlighted. Here the investigation area is much smaller (\sim half of the size), but again the measurements reflect anomalies caused by the crust-mantle boundary. Table 4-2 gives a comprehensive overview which features can be resolved by satellite and terrestrial data, respectively.

The modelling of the crust-mantle boundary allows assumptions and interpretation about the isostatic state of an investigation area. Thus, satellite gravity data can be used for interpretation of such long wavelength features.

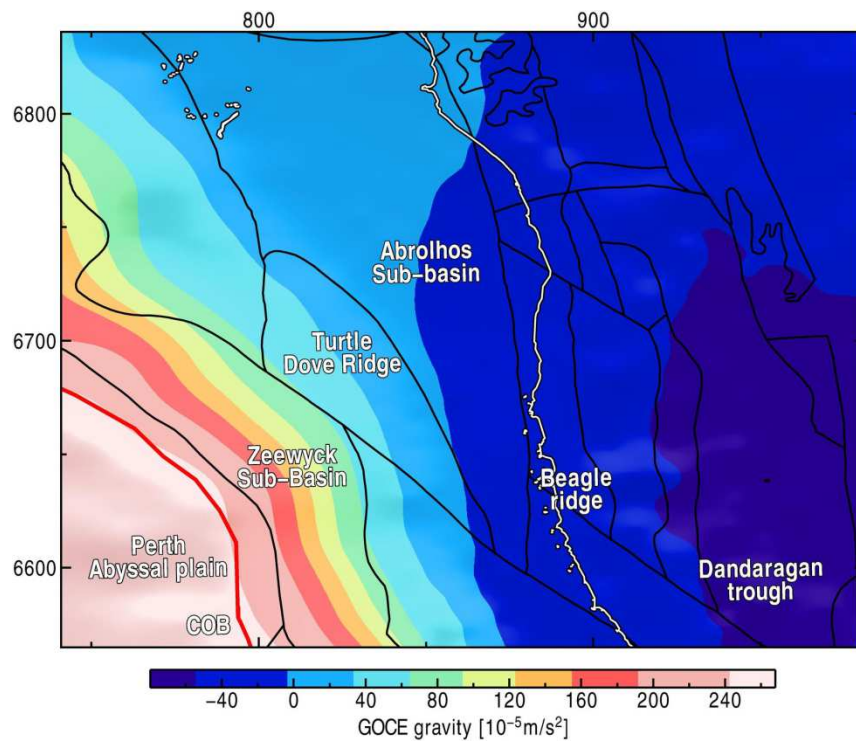


Figure 4-14: Bouguer anomaly derived from GOCO-03S.

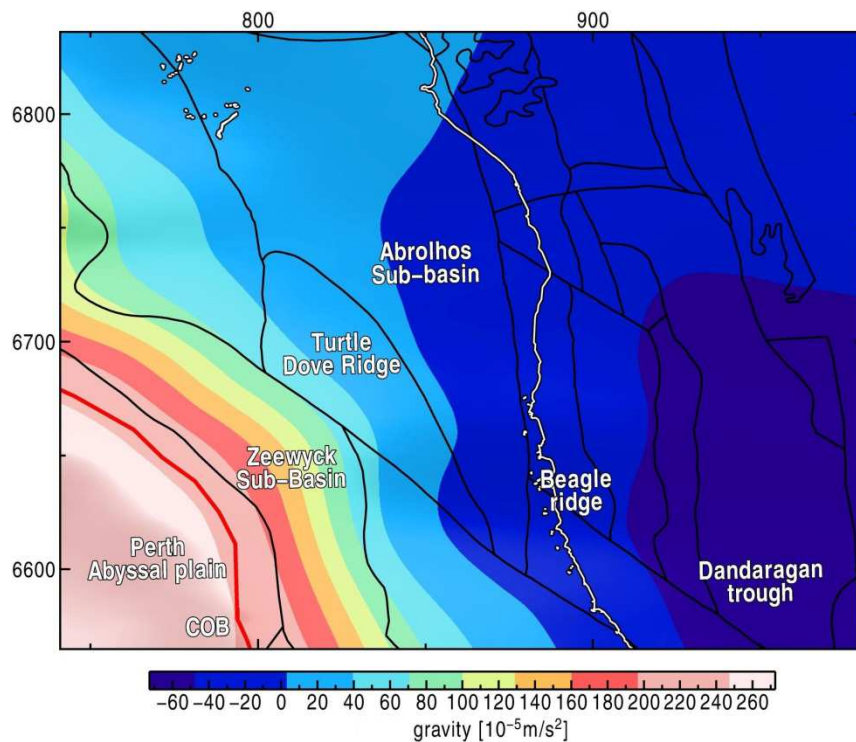


Figure 4-15: Calculated gravity from the modified Model 2 (chapter 4.4.3). Here, only the Moho is modelled to achieve a fit to the satellite gravity field.

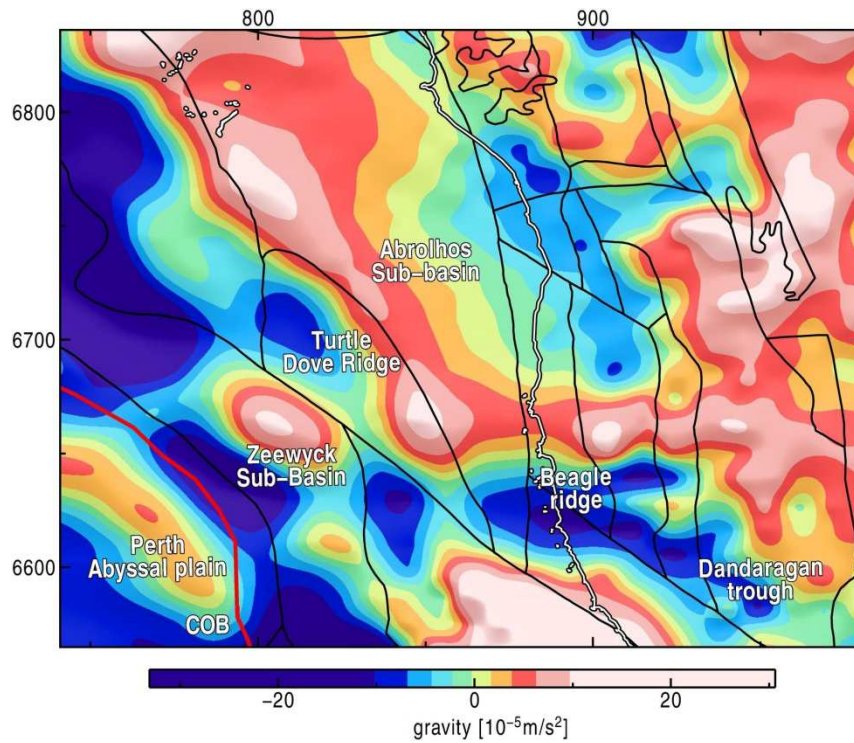


Figure 4-16: Residual gravity between the modelled and calculated gravity field of the satellite only model. Large positive misfits are visible in the Abrolhos Sub-basin and the Dandaragan trough. These indicate too much mass in the 3D model which can be modelled with sedimentary infill. However, the actual anomalies caused by the sedimentary basins are larger than the misfit.

Structure	Satellite gravity data	Ground based gravity data
Moho (crust mantle boundary)	++	+
Sedimentary basins	-	++
Lithosphere-asthenosphere boundary	+	--
Volcanic back-arc	--	++
Deep sea trench	+	++

Table 4-2: An overview how the discussed features from chapter 2.4.3 and 4.4 are visible in the satellite and ground based gravity data. In general, long wavelength features can be seen well in satellite gravity data. Ground based data shows better sensitivity of smaller anomalies.

5 Conclusion and Outlook

5.1 Conclusion

Satellite gravity missions offers global gravity models which can be used for density modelling. The global availability of these datasets makes it possible to investigate almost any region of the world. Due to low spatial resolution ($\sim 100 \text{ km}$) the data has to be rather used for regional (several hundreds of kilometres) than for local scales. Global gravity models are available with several different definitions introduced by geodesists and geophysicists. Chapter 2.4 compared Bouguer gravity compiled from the EGM2008 "classic gravity anomaly" (defined on the geoid) and the gravity disturbance (defined at the terrestrial surface) with terrestrial data. The definition of the gravity disturbance is identical to the "geophysical free air anomaly". The comparisons showed high correlation for both fields (over 90 %). However, in regions of high topography, both anomalies feature deviations from the terrestrial data. The Bouguer slab corrected gravity disturbance provided a better correlation to the terrestrial data in the North Andes where topography is higher. Comparisons in the area of Costa Rica showed large deviations ($\sim 100 * 10^{-5} \frac{m}{s^2}$) in the "classic gravity anomaly" at the Talamanka mountain range which do not show up in the gravity disturbance Bouguer anomaly. Therefore, for geophysical subsurface modelling, the gravity disturbance has to be used and corrected for the topographic mass.

Topographic correction is a mandatory step for compiling Bouguer anomalies in areas of rugged terrain. Combined satellite gravity models feature high frequent anomalies at high elevations. In addition, regional investigations of gravity, satellite gravity (gradients) and high resolution DTMs asked for revision of existing topographic correction methods. Existing methods can be classified in two categories: station dependent and station independent corrections. Station dependent corrections were developed before computers were available. The correction involved calculating mean heights for each station by hand. This undertaken includes lot of redundant calculations, especially for nearby stations. The representation of topography by mean heights could not account for rugged terrain correctly. Station independent algorithms were developed starting in the 60s. Here, topography grids with different resolution were calculated once and used for corrections. The algorithms used different resolutions which reflects the $\frac{1}{r^2}$ dependency of gravity between station and attracting mass. Usually, for representation of the terrain geometry, cubes (rectangular prisms) are used. It was shown that prisms causes overlaps and gaps between the element bodies, if sphericity of the earth is considered. The resampling of topography only dependent on the distance to the station cannot account for distant terrain effects correctly, because this method does not account the geometry of topography for resampling.

As a consequence, a new correction algorithm for topographic masses was developed based on polyhedral shapes. It was proven that polyhedral bodies feature a better representation of the terrain geometry. In particular, valleys and coast lines are mapped with higher accuracy. The new adaptive approach for resampling of topography was developed to deal correctly with distant terrain and save computation time. This algorithm uses a higher resolution of topography **if it influences the gravity at the station**. Therefore, it accounts for the distance of the station and the

geometry of the terrain implicitly. As a first test, calculations with different algorithms (prism, tesseroid and polyhedron representation and FFT) and different DTM resolutions were performed in central Asia. The area included the Himalayan and Kunlun mountain range and the Tibetan plateau. It was proven that all algorithms calculate similar corrections (except for the FFT corrections). Misfits (about $5 * 10^{-5} \frac{m}{s^2}$) between prisms and tesseroids compared to polyhedrons occur when coarser DTM are used. Second, the effect of the DTM grid spacing on the topographic corrections were investigated. The results pointed out that the resolution of the initial DTM has a significant impact on the corrections. Therefore, the highest available resolution of DTM should be chosen to achieve the best approximation of the gravitational effect of topographic masses. Finally, the impact of distant terrain was investigated. Accounting for distant terrain (distance > 167 km) caused up to $6 * 10^{-5} \frac{m}{s^2}$ difference between two stations in the first test bed. The gravity effect was largest for stations located in (rather) flat terrain but surrounded by rugged distant terrain. If stations were located in nearby rugged terrain and surrounded by smooth distant terrain the gravity effect was lower. Limiting the correction to a specific radius around the station can cause different Bouguer anomalies compared to corrections considering distant terrain. But, calculation of distant terrain in high resolution can be very time consuming. Thus, the adaptive approach was tested against corrections without any resampling. It could be shown that corrections with the adaptive approach are almost identical to corrections considering a full resolution for the whole DTM in only a fraction of time (100 - 300 times faster in the Himalayan test bed). Thus, the adaptive approach makes it possible to perform an accurate correction of distant terrain with massive savings in computation time.

The polyhedron and prism algorithm was used to recalculate the Bouguer anomaly compiled by Tašárová (2004) at the Andean margin. Differences occur when corrections are calculated with the adaptive approach and a limiting radius of 167 km. Here, the Bouguer anomaly changed at the coastal cordillera and the fore-arc basin. Comparisons with former Bouguer anomaly corrections feature larger deviations in the back-arc of the Andes and the recalculation correlated better with geological underground structures in the area. The tests show that the new developed correction method is a valuable tool to correct gravity data on local and regional scales. The adaptive approach leads to significant computational savings which allows the correction of effects of distant terrain in an acceptable runtime. The new GOCE satellite mission provides directly measured gravity gradients. Therefore, gradient correction was implemented in the new software. A test calculation in the Andes shows that gradients are highly influenced by topography. The correction revealed lithospheric structures.

There were three test beds introduced which can prove the advantages of the new method compared to older ones in different tectonic environments in areas (1) of very high topography (Central Asia) and (2) active continental margins (Andes) as well as (3) the passive continental margin. The North Perth basin at the West Australian margin was selected for this test bed (3). The gravity correction was initially conducted with a spherical Bouguer slab and a topographic correction approximated with prisms. A limiting radius of 167 km was internationally defined. The new correction by polyhedrons combined with the adaptive approach showed a different Bouguer anomaly in the North of the Dandaragan trough. The contrast between the negative gravity

anomaly caused by sedimentary infill and higher gravity anomalies in the North shifted more to the South in the recalculated Bouguer anomaly. This correlates far better with the geological structures in this area.

The modelling of the North Perth basin was conducted with terrestrial gravity data and later compared to satellite gravity data. This was done to test how interpretations and findings of 3D density modelling changes if terrestrial data or satellite data is used.

The main focus in this study was put on the modelling of the sedimentary basins and the crust-mantle boundary. Sedimentary basins were constrained by reflection seismics. The area lacks of constraints about the crust-mantle boundary, so different assumptions about the isostatic state were tested and analysed. It was shown that local isostasy does not explain the present isostatic state in the whole basin. An external Moho model (Aitken, 2010) derived from continental-wide inversion of the gravity field could explain the observed gravity in the entire basin. It was shown from 3D density modelling that the negative anomaly associated with the Dandaragan trough is caused by deep sedimentary infill (>12 km) and a deep Moho. Thus, the evolution of the basin cannot be explained with crustal thinning and stretching, but with a crustal-scale rigid block rotation on the Darling Fault. This is also consistent with higher T_e values (15-25 km) which were calculated in this area. The modelling also indicated that the crust under the Zeewyck Sub-basin is significantly weaker than the crust in the other parts of the model. This could be explained by deep-penetrating strike-slip faulting. Finally, the geometry from the 3D density modelling showed steep edges and thick sediments at the Zeewyck Sub-basin which is consistent with a transtensional basin evolution.

The calculated gravity of the final models was compared to GOCE satellite gravity data. The satellite gravity field reflects the effect of Moho in this region. The anomalies caused by the sedimentary basins do not show up clearly. The effect of slightly less mass in the Sub-basins can be obtained if satellite gravity is compared with the gravity effect of a simple two layer crust-mantle model. Therefore, the interpretations about the crust-mantle boundary are also possible with satellite derived gravity. This was demonstrated in chapter 2.4.3 where anomalies of satellite gravity shows were caused by the deep trench west of the Andean margin and onshore by long wavelength domains of the crust, mantle and asthenosphere all show up in the satellite gravity models.

Satellite gravity models have a good resolution for long wavelength features and can be used for 3D density modelling of deeper density contrasts represented by the Moho and/or lithosphere-asthenosphere boundary (LAB). For interpretations at smaller lithospheric scales e.g. in sedimentary basins, additional terrestrial data has to complement satellite gravity.

5.2 Outlook

The main results of the thesis proved that topographic corrections of measured gravity are mandatory for interpreting anomalies in the lithosphere. If structures close to the surface are investigated, other long wavelengths caused by isostasy (e.g. Moho or LAB) are removed to interpret residual gravity anomalies. The new method for topographic correction can be used to remove the gravity effect those deep seated density boundaries. For this purpose, the geometry of the Moho (or LAB) interface has to be calculated from independent information (MT, receiver functions, etc.). Then, the new algorithm could be used to correct the measured gravity for these long wavelengths. The resampling conducted by the adaptive approach can be analysed and provides hints on the sensitivity of structural shapes which causes the modelled gravity. Of course, this analysis can also be extended to other surfaces/interfaces of 3D density models to assess for accurate bodies. In general, the resampling methods could also be used to reduce quantity of model constraints provided by other methods (e.g. seismic reflectors).

Satellite gravity missions can be used to interpret deep seated density contrasts of the lithosphere. Geophysical lithospheric modelling with satellite gravity data is still under ongoing research. However, satellite gravity provides very low resolution if upper crustal anomalies should be investigated. The combination of satellite gravity data and terrestrial data (as done for the EGM2008) is promising to combine the good resolution of long wavelengths by the satellite measurements and the small wavelengths inherent in the measured terrestrial data. In inaccessible areas where no ground based data exist, only satellite gravity provides a unique source. Next future satellite missions will not be able to measure gravity with a higher resolution than the recent GOCE mission (about 80 km wavelength) due to limitations of the flight height. Therefore, the assessment of high resolution gravity data (e.g. airborne measurements of the HALO project: <http://www.halo.dlr.de/>) could be acquired and combined with satellite gravity for better gravity coverage in such regions.

The availability of vast datasets will increase in future. Storage, distribution and acquiring of large datasets are not a problem any longer. Therefore, approaches are necessary to reduce data without loss of information. The software developments and modelling results described in this thesis provide promising approaches toward geophysical applications.

References

- Aitken, A.R.A., 2010. Moho geometry gravity inversion experiment (MoGGIE): A refined model of the Australian Moho, and its tectonic and isostatic implications, *Earth and Planetary Science Letters*, 297, 71–83.
- Alasonati-Tašárová, Z.A., 2007. Towards understanding the lithospheric structure of the southern Chilean subduction zone (36°S-42°S) and its role in the gravity field, *Geophys. J. Int.*, 170, 995–1014.
- Allmendinger, R.W., Jordan, T.E., Kay, S.M. & Isacks, B.L., 1997. The Evolution of the Altiplano-Puna Plateau of the Central Andes, *Annu. Rev. Earth Planet. Sci.*, 25, 139-174.
- Amante, C. & Eakins, B.W., 2009. ETOPO1 1 Arc-Minute Global Relief Model: Procedures, Data Sources and Analysis, pp. 19NOAA Technical Memorandum NESDIS NGDC-24.
- Andersen, O.B. & Knudsen, P., 1998. Global marine gravity field from the ERS-1 and Geosat geodetic mission altimetry, *J. Geophys. Res.*, 103, 8129-8137.
- Antobreh, A.A., Faleide, J.I., Tsikalas, F. & Planke, S., 2009. Rift–shear architecture and tectonic development of the Ghana margin deduced from multichannel seismic reflection and potential field data, *Marine and Petroleum Geology*, 26, 345–368.
- Aochi, R., Madariaga, E. & Fukuyama, E., 2003. Constraint of fault parameters inferred from nonplanar fault modeling, *Geochem. Geophys. Geosyst.*, 4, 16.
- Arroyo, I.G., Husen, S., Flueh, E.R., Gossler, J., Kissling, E. & Alvarado, G.E., 2009. Three-dimensional P-wave velocity structure on the shallow part of the Central Costa Rican Pacific margin from local earthquake tomography using off- and onshore networks, *Geophysical Journal International*, 179, 827-849.
- Asgharzadeh, M.F., Von Frese, R.R.B., Kim, H.R., Leftwich, T.E. & Kim, J.W., 2007. Spherical prism gravity effects by Gauss-Legendre quadrature integration, *Geophysical Journal International*, 169, 1-11.
- Ashcroft, W.A., Hurst, A. & Morgan, C.J., 1999. Reconciling gravity and seismic data in the Faeroe–Shetland Basin, West of Shetland, *Geological Society, London, Petroleum Geology Conference Series*, 5, 595–600.
- Athy, L.F., 1930. Density, porosity, and compaction of sedimentary rocks, *AAPG Bulletin*, 14, 1-24.
- Babeyko, A.Y., Sobolev S. V. Vietor T. Oncken O. & Trumbull, R.B., 2006. Numerical Study of Weakening Processes in the Central Andean Back-Arc. In: The Andes – active subduction

- orogeny. *Frontiers in Earth Science Series*, pp. 495-512 Springer-Verlag, Berlin Heidelberg New York.
- Bahr, D.B., Hutton, E.W.H., Syvitski, J.P.M. & Pratson, L.F., 2001. Exponential approximations to compacted sediment porosity profiles, *Computers & Geosciences*, 27, 691–700.
- Bähr, H.-P., Ehlers, E., Emmermann, R., Harjes, H.-P., Lauterjung, J., Mosbrugger, V., Rudloff, A., Seifert, F., Stroink, L., Thiede, J., Wefer, G. & Wellmer, F.-W., 2003. GEOTECHNOLOGIEN: Das System Erde: Vom Prozessverständnis zum Management, Programmschrift.
- Barckhausen, U., Roeser, H.A. & von Huene, R., 1998. Magnetic signature of upper plate structures and subducting seamounts at the convergent margin off Costa Rica, *J. Geophys. Res.*, 103, 7079-7093.
- Barrère, C., Ebbing, J. & Gernigon, L., 2009. Offshore prolongation of Caledonian structures and basement characterisation in the western Barents Sea from geophysical modelling, *Tectonophysics*, 470, 71–88.
- Barthelmes, F., 2009. Definition of Functionals of the Geopotential and Their Calculation from Spherical Harmonic Models: Theory and formulas used by the calculation service of the International Centre for Global Earth Models (ICGEM), <http://icgem.gfz-potsdam.de>.
- Bäschlin, C.F., 1948. *Lehrbuch der Geodäsie*, edn, Vol. 1, pp. Pages, Orell Füssli.
- Becker, J.J., Sandwell, D.T., Smith, W.H.F., Braud, J., Binder, B., Depner, J., Fabre, D., Factor, J., Ingalls, S., Kim, S.H., Ladner, R., Marks, K., Nelson, S., Pharaoh, A., Trimmer, R., Von Rosenberg, J., Wallace, G. & Weatherall, P., 2009. Global Bathymetry and Elevation Data at 30 Arc Seconds Resolution: SRTM30_PLUS, *Marine Geodesy*, 32, 355-371.
- Bernardel, G. & Nicholson, C., 2013. Geoscience Australia Seismic Survey GA 310 — revealing stratigraphy and structure of the outer northern Perth Basin margin, *APPEA Journal and Conference Proceedings, Extended Abstracts*, 53, 4pp.
- Berry, P.A.M., Smith, R. & Benveniste, J., 2008. ACE2: the new Global Digital Elevation Model. *in IAG International Symposium on Gravity, Geoid & Earth Observation*, Chania, Crete, 23-27th June 2008.
- Bird, D., 2001. Shear margins: Continent-ocean transform and fracture zone boundaries, *The Leading Edge*, 20, 150–159.
- Blaich, O.A., Faleide, J.I., Tsikalas, F., Lilletveit, R., Chiossi, D., Brockbank, P. & Cobbold, P., 2010. Structural architecture and nature of the continent-ocean transitional domain at the Camamu and Almada Basins (NE Brazil) within a conjugate margin setting, *Geological Society, London, Petroleum Geology Conference Series*, 7, 867–883.

References

- Bohm, M., Lüth, S., Echtler, H., Asch, G., Bataille, K., Bruhn, C., Rietbrock, A. & Wigger, P., 2002. The Southern Andes between 36° and 40°S latitude: seismicity and average seismic velocities, *Tectonophysics*, 356, 275-289.
- Bolge, L.L., Carr, M.J., Milidakis, K.I., Lindsay, F.N. & Feigenson, M.D., 2009. Correlating geochemistry, tectonics, and volcanic volume along the Central American volcanic front, *Geochem. Geophys. Geosyst.*, 10, Q12S18.
- Boutelier, D.A. & Oncken, O., 2010. The role of the plate margin curvature in the plateau build-up: consequences for the Central Andes, *J. Geophys. Res.*, 115.
- Braitenberg, C., Ebbing, J. & Götze, H.-J., 2002. Inverse modelling of elastic thickness by convolution method – the eastern Alps as a case example, *Earth and Planetary Science Letters*, 202, 387–404.
- Brasse, H., Kapinos, G., Mütschard, L., Alvarado, G.E., Worzewski, T. & Jegen, M., 2009. Deep electrical resistivity structure of northwestern Costa Rica, *Geophys. Res. Lett.*, 36, L02310.
- Buske, S., Lüth, S., Meyer, H., Patzig, R., Reichert, C., Shapiro, S., Wigger, P. & Yoon, M., 2002. Broad depth range seismic imaging of the subducted Nazca Slab, North Chile, *Tectonophysics*, 350, 273-282.
- Buswell, A.J., Powell, W.D. & Scholefield, T., 2004. The northern Perth Basin - from marginally prospective for gas to highly prospective for both oil and gas, *The APPEA Journal*, 44, 181–199.
- Chappell, A.R. & Kusznir, N.J., 2008. Three-dimensional gravity inversion for Moho depth at rifted continental margins incorporating a lithosphere thermal gravity anomaly correction, *Geophysical Journal International*, 174, 1–13.
- Christensen, N.I. & Mooney, W.D., 1995. Seismic velocity structure and composition of the continental crust: A global view, *Journal of Geophysical Research*, 100, 9761–9788.
- Clitheroe, G., Gudmundsson, O. & Kennett, B.L.N., 2000. The crustal thickness of Australia, *Journal of Geophysical Research*, 105, 13697–13713.
- Cloos, M., 1992. Thrust-type subduction-zone earthquakes and seamount asperities: a physical model for seismic rupture, *Geology*, 20, 601-604.
- Collins, C.D.N., Drummond, B.J. & Nicoll, M.G., 2003. Crustal thickness patterns in the Australian continent. in *Evolution and Dynamics of the Australian Plate*, pp. 121–128, eds. Hillis, R. R. & Müller, R. D. Geological Society of Australia Special Publication 22 and Geological Society of America Special Paper 372.

- Delaunay, B., 1934. Sur la sphère vide, *Bulletin of Academy of Sciences of the USSR*, 793-800.
- DeMets, C., Gordon, R.G., Argus, D.F. & Stein, S., 1994. Effect of recent revisions to the geomagnetic reversal time scale on estimates of current plate motions, *Geophysical Research Letters*, 21, 2191-2194.
- Denker, S., 2004. Evaluation of SRTM3 and GTOPO30 terrain data in Germany. . *in Association of Geodesy Symposia, Gravity, Geoid and Space Missions*, pp. 218pp., ed al., C. J. e.
- Dentith, M., Bruner, I., Long, A., Middleton, M.F. & Scott, J., 1993. Structure of the eastern margin of the Perth Basin, Western Australia, *Exploration Geophysics*, 24, 455–463.
- Dentith, M.C., Dent, V.F. & Drummond, B.J., 2000. Deep crustal structure in the southwestern Yilgarn Craton, Western Australia, *Tectonophysics*, 325, 227–255.
- DeShon, H.R., Schwartz, S.Y., Bilek, S.L., Dorman, L.M., Gonzalez, V., Protti, J.M., Flueh, E.R. & Dixon, T.H., 2003. Seismogenic zone structure of the southern Middle America Trench, Costa Rica, *J. Geophys. Res.*, 108, 14.
- Ehrismann, W., 1972. Ein rationelles Verfahren zur numerischen Berechnung der Schwerewirkung von grossräumigen digital simulierten Modellkörpern, Technische Universität Clausthal.
- Ehrismann, W. & Lettau, O., 1971. Topographische Reduktion von Schweremessungen in der näheren und weiteren Stationsumgebung mit Digitalrechnern, *Archiv für Meteorologie, Geophysik und Bioklimatologie, Serie A*, 20, 383-396.
- Farr, T.G., Rosen, P.A., Caro, E., Crippen, R., Duren, R., Hensley, S., Kobrick, M., Paller, M., Rodriguez, E., Roth, L., Seal, D., Shaffer, S., Shimada, J., Umland, J., Werner, M., Oskin, M., Burbank, D. & Alsdorf, D., 2007. The Shuttle Radar Topography Mission, *Reviews of Geophysics*, 45, RG2004.
- Fedi, M., Ferranti, L., Florio, G., Giori, I. & Italiano, F., 2005. Understanding the structural setting in the Southern Apennines (Italy): insight from Gravity Gradient Tensor, *Tectonophysics*, 397, 21 - 36.
- Foerste, C., Flechtner, F., Schmidt, R., Stubenvoll, R., Rothacher, M., Kusche, J., Neumayer, K.-H., Biancale, R., Lemoine, J.-M., Barthelmes, F., Bruinsma, J., Koenig, R. & Meyer, U., 2008. A new global combined high-resolution GRACE-based gravity field model of the GFZ-GRGS cooperation. *in General Assembly European Geosciences Union (Vienna, Austria 2008)*Geophysical Research Abstracts.
- Francis, T.J.G. & Raitt, R.W., 1967. Seismic Refraction Measurements in the Southern Indian Ocean, *Journal of Geophysical Research*, 72, 3015–3041.

References

- FrOG Tech, 2005. The OZ SEEBASE™ Project: A new view of Australia's Phanerozoic basins, *PESA News*, August/September, 12–13.
- Fuller, C.W., Willett, S.D. & Brandon, M.T., 2006. Formation of forearc basins and their influence on subduction zone earthquakes, *Geology*, 34, 65-68.
- Geoscience Australia, 2008. GEODATA 9 second DEM and D8: Digital Elevation Model Version 3 and Flow Direction Grid 2008: User Guide, pp. 45 Geoscience Australia, Canberra, Australia.
- Geoscience Australia, 2011. Energy Security Program Achievements—Towards Future Energy Discovery, pp. 101 Geoscience Australia, Canberra, Australia.
- Giese, P., Asch, G., Brasse, H., Götze, H., Haberland, C. & Wigger, P., 1999. Procesos geodinámicos en los andes centrales, representados mediante observaciones geofísicas. in *{Geología del Noroeste Argentino, Relatorio, Tomo I, Salta}*, pp. 15-17, eds. B, G. G., Omarini, R. & Viramonte, J.
- Goltz, G., 1989. Zur Theorie und Anwendung der topographischen Reduktion nach Sideris in der Gravimetrie, Diplomarbeit, Freie Universität, Berlin.
- Götze, H.-J., 1976. Ein numerisches Verfahren zur Berechnung der gravimetrischen und magnetischen Feldgrößen für dreidimensionale Modellkörper, PhD thesis Dissertation, Technische Universität Clausthal, Clausthal-Zellerfeld, Germany.
- Götze, H.-J. & Lahmeyer, B., 1988. Application of three-dimensional interactive modeling in gravity and magnetics, *Geophysics*, 53, 1096–1108.
- Götze, H.-J., Lahmeyer, B., Schmidt, S. & Strunk, S., 1994. {The lithospheric structure of the central Andes (20° - 26°S) as inferred from interpretation of regional gravity} *Tectonics of the Southern Central Andes*, pp. 7-21, eds. Reutter, K. J., Scheuber, E. & Wigger, P. J. Springer-Verlag, New York.
- Götze, H., Schmidt, S., Fichler, C. & Alvers, M.R., 2007. IGMAS+ A New 3D Gravity, FTG and Magnetic Modeling Software, pp. 01.
- Götze, H.J. & Krause, S., 2002. The Central Andean gravity high, a relic of an old subduction complex?, *Journal of South American Earth Sciences*, 14, 799-811.
- Greenroyd, C.J., Peirce, C., Rodger, M., Watts, A.B. & Hobbs, R.W., 2007. Crustal structure of the French Guiana margin, West Equatorial Atlantic, *Geophysical Journal International*, 169, 964–987.
- Grohman, G., Kroenung, G. & Strebeck, J., 2006. Filling SRTM voids: The delta surface fill method, *Photogramm. Eng. Rem. Sens.*, 72, 213-216.

- Grombein, T., Seitz, K. & Heck, B., 2010. Untersuchungen zur effizienten Berechnung topographischer Effekte auf den Gradiententensor am Fallbeispiel der Satellitengradiometriemission GOCE. (KIT Scientific Reports ; 7547).
- Group, A.W., 2003. Seismic imaging of a convergent continental margin and plateau in the central Andes (Andean Continental Research Project 1996 (ANCORP'96)), *J. Geophys. Res.*, 108, 2328.
- Gutscher, M.-A., Spakman, W., Bijwaard, H. & Engdahl, E.R., 2000. "Geodynamics of flat subduction: Seismicity and tomographic constraints from the Andean margin", *Tectonics*, 19, 814-833.
- Hackney, R., Echtler, H., Franz, G., Götze, H.-J., Lucassen, F., Marchenko, D., Melnick, D., Meyer, U., Schmidt, S., Tašárová, Z., Tassara, A. & Wienecke, S., 2006. {The segmented overriding plate and coupling at the south-central Chile margin} The Andes -- active subduction orogeny, pp. 355–374, eds. Oncken, O., Chong, G., Franz, G., Giese, P., Götze, H. J., Ramos, V. A., Strecker, M. R. & Wigger, P. Springer-Verlag, Berlin Heidelberg New York.
- Hackney, R.I., 2012. Combined marine and land potential-field datasets for the southwest margin of Australia, pp. 62 Geoscience Australia.
- Hackney, R.I. & Featherstone, W.E., 2003. Geodetic versus geophysical perspectives of the 'gravity anomaly', *Geophysical Journal International*, 154, 35-43.
- Hall, L., Gibbons, A.D., Bernardel, G., Whittaker, J.M., Nicholson, C., Rollet, N. & Müller, R.D., in press. Structural architecture of Australia's southwest continental margin and implications for Early Cretaceous basin evolution. in *Proceedings, West Australian Basins Symposium 18–21 August 2013*, eds Keep, M. & Moss, S. Petroleum Exploration Society of Australia.
- Hall, O., Falomi, G. & Bras, R.L., 2005. Characterization and Quantification of Data Voids in the Shuttle Radar Topography Mission Data, *IEEE Geoscience and remote sensing letters*, 2.
- Harris, L.B., 1994. Structural and tectonic syntheses for the Perth Basin, Western Australia, *Journal of Petroleum Geology*, 17, 129–156.
- Hayford, J.F. & Bowie, W., 1912. The Effect of Topography and Isostatic Compensation upon the Intensity of Gravity, *U.S. Coast and Geod. Survey, Spec Publ.*, 10.
- Heck, B. & Seitz, K., 2007. A comparison of the tesseroid, prism and point-mass approaches for mass reductions in gravity field modelling, *Journal of Geodesy*, 81, 121-136.
- Helmert, F.R., 1884. Die mathematischen Grundlagen und physikalischen Theorien der höheren Geodäsie, *Teubner Verlag, Leipzig*, Bd. 2.

References

- Heuret, A. & Lallemand, S., 2005. Plate motions, slab dynamics and back-arc deformation, *Physics of the Earth and Planetary Interiors*, 149, 31-51.
- Higgins, K., Hashimoto, T., Hackney, R.I., Petkovic, P. & Milligan, P., 2011. 3D Geological Modelling and Petroleum Prospectivity Assessment in Offshore Frontier Basins using GOCAD™: Capel and Faust Basins, Lord Howe Rise, pp. 72Geoscience Australia.
- Hoffmann, J. & Walter, D., 2006. How complementary are SRTM-X and -C band digital elevation models?, *Photogramm. Eng. Rem. Sens.*, 72, 261-268.
- Holstein, H., Sherratt, E.M. & Reid, A.B., 2007. Gravimagnetic field tensor gradiometry formulas for uniform polyhedra, *SEG Technical Program Expanded Abstracts*, 26, 750-754.
- Husen, S., 1999. Local earthquake tomography of a convergent margin, North Chile., Ph.D., Christian-Albrechts-Universität, Kiel.
- Husen, S., Quintero, R., Kissling, E. & Hacker, B., 2003. Subduction-zone structure and magmatic processes beneath Costa Rica constrained by local earthquake tomography and petrological modelling, *Geophysical Journal International*, 155, 11-32.
- Iasky, R.P. & Mory, A.J., 1993. Structural and tectonic framework of the onshore northern Perth Basin, *Exploration Geophysics*, 24, 585–592.
- Iasky, R.P., Mory, A.J. & Shevchenko, S., 1997. Structural interpretation of a sedimentary basin using high-resolution magnetic and gravity data, *Exploration Geophysics*, 28, 247–251.
- Iasky, R.P., Young, R.A. & Middleton, M.F., 1991. Structural study of the southern Perth Basin by geophysical methods, *Exploration Geophysics*, 22, 199–206.
- Jarvis, A., Reuter, H.I., Nelson, A. & Guevara, E., 2008. Hole-filled SRTM for the globe Version 4, available from the CGIAR-CSI SRTM 90m Database.
- Johnston, S. & Petkovic, P., 2012. Depth to magnetic sources in the offshore northern Perth Basin, *ASEG Extended Abstracts*, 2012, 4pp.
- Johnston, S.W. & Goncharov, A., 2012. Velocity analysis and depth conversion in the offshore Northern Perth Basin, pp. 31Geoscience Australia.
- Jones, A.T., Kennard, J.M., Nicholson, C.J., Bernardel, G., Mantle, D., Grosjean, E., Boreham, C.J., Jorgensen, D.C. & Robertson, D., 2011. New exploration opportunities in the offshore northern Perth Basin, *The APPEA Journal*, 51, 45–78.
- Jordan, T.E., Reynolds III, J.H. & Erikson, J.P., 1997. *Variability in age of initial shortening and uplift in the Central Andes*, edn, Vol., pp. Pages, Plenum Press, New York.

- Kennett, B.L.N., Salmon, M., Saygin, E. & Group, A.W., 2011. AusMoho: the variation of Moho depth in Australia, *Geophysical Journal International*, 187, 946–958.
- Kimbell, G.S., Ritchie, J.D. & Henderson, A.F., 2010. Three-dimensional gravity and magnetic modelling of the Irish sector of the NE Atlantic margin, *Tectonophysics*, 486, 36–54.
- Kirby, S., Engdahl E.R. & Denlinger, R., 1996. *Intermediate-depth intraslab earthquakes and arc volcanism as physical expressions of crustal and uppermost mantle metamorphism in subducting slabs.*, edn, Vol., pp. Pages, American Geophysical Union, Geophysical Monograph 96, Washington, DC.
- Kirchner, A., Götze, H.J. & Schmitz, M., 1996. 3D-density modelling with seismic constraints in the Central Andes, *Physics and Chemistry of The Earth*, 21, 289 - 293.
- Klotz, J., Abolghasem, A., Khazaradze, G., Heinze, B., Vietor, T., Hackney, R., Bataille, K., Maturana, R., Viramonte, J. & Perdomo, R., 2006. 4 Long-Term Signals in the Present-Day Deformation Field of the Central and Southern Andes and Constraints on the Viscosity of the Earth's Upper Mantle. in *The Andes*, pp. 65-89, eds. Oncken, O., Chong, G., Franz, G., Giese, P., Götze, H.-J., Ramos, V., Strecker, M. & Wigger, P. Springer Berlin Heidelberg.
- Klotz, J., Khazaradze, G., Angermann, D., Reigber, C., Perdomo, R. & Cifuentes, O., 2001. Earthquake cycle dominates contemporary crustal deformation in Central and Southern Andes, *Earth and Planetary Science Letters*, 193, 437-446.
- Köther, N., 2009. Joint 3D gravity and magnetic modelling of the Taoudeni basin, Diplomarbeit, Christian-Albrechts-Universität, Kile.
- Köther, N., Götze, H.J., Gutknecht, B.D., Jahr, T., Jentzsch, G., Lücke, O.H., Mahatsente, R., Sharma, R. & Zeumann, S., 2012. The seismically active Andean and Central American margins: Can satellite gravity map lithospheric structures?, *Journal of Geodynamics*, 59–60, 207-218.
- LaFehr, T.R., 1991. Standardization in gravity reduction, *GEOPHYSICS*, 56, 1170-1178.
- LaFehr, T.R., 1998. On Talwani's "Errors in the total Bouguer reduction", *GEOPHYSICS*, 63, 1131-1136.
- Lessel, K., 1997. Die Krustenstruktur der zentralen Anden in Nordchile (21 - 24°S), abgeleitet aus 3D-Modellierungen refraktionsseismischer Daten, Freie Universität Berlin, Berlin.
- Li, X. & Götze, H.J., 2001. Ellipsoid, geoid, gravity, geodesy, and geophysics, *GEOPHYSICS*, 66, 1660-1668.
- Lonsdale, P., 2005. Creation of the Cocos and Nazca plates by fission of the Farallon plate, *Tectonophysics*, 404, 237 - 264.

References

- Lücke, O.H., 2012. 3D Density Model of the Central American Isthmus from Satellite Derived Gravity Data, Ph.D. thesis, Christian-Albrechts-Universität zu Kiel.
- Lücke, O.H., Götze, H.-J. & Alvarado, G.E., 2010. A Constrained 3D Density Model of the Upper Crust from Gravity Data Interpretation for Central Costa Rica, *International Journal of Geophysics*, 2010, 9 pp.
- Lüth, S., Wigger, P., Araneda, M., Asch, G., Bataille, K., Bohm, M., Bruhn, C., Giese, P., Lüth, S., Quezada, J. & Rietbrock, A., 2003. A crustal model along 39°S from a seismic refraction profile--ISSA 2000, *Revista Geológica de Chile*, 30, 83-101.
- Madariaga, R. & Cochard, A., 1996. Dynamic friction and the origin of the complexity of earthquake sources, *Proceedings of the National Academy of Sciences*, 93, 3819-3824.
- Mader, F., 1951. Das newtonsche Raumpotenzial prismatischer Körper und seiner Ableitungen bis zur dritten Ordnung, *Österreichische Zeitung für Vermessungswesen, Sonderheft*, 10.
- Marsan, D., 2006. Can coseismic stress variability suppress seismicity shadows? Insights from a rate-and-state friction model, *Journal of Geophysical Research: Solid Earth*, 111, B06305.
- Mayer-Guerr, T., 2007. ITG-Grace03s: The latest GRACE gravity field solution computed in Bonn.
- Mayer-Gürr, T., 2012. The new combined satellite only model GOCO03s. . in *GGHS2012, Venice (Poster)*.
- Meschede, M., Barckhausen, U. & Worm, H.-U., 1998. Extinct spreading on the Cocos Ridge, *Terra Nova*, 10, 211-216.
- Meurers, B., Ruess, D., 2009. A new Bouguer gravity map of Austria, *Austrian Journal of Earth Sciences*, 102, 62-70.
- Mikuška, J., Pašteka, R. & Marušiak, I., 2006. Estimation of distant relief effect in gravimetry, *GEOPHYSICS*, 71, J59-J69.
- Mory, A.J. & Iasky, R.P., 1996. Stratigraphy and structure of the onshore northern Perth Basin, pp. 101 Geological Survey of Western Australia.
- Müller, A., 1999. Ein EDV-orientiertes Verfahren zur Berechnung der topographischen Reduktion im Hochgebirge mit digitalen Geländemodellen am Beispiel der zentralen Anden, Ph.D., Freie Universität Berlin, Berlin.
- Mundry, E., 1970. *Zur automatischen Herstellung von Isolinenplänen*, edn, Vol., pp. Pages, BGR, Hannover.

- Nagy, D., 1966. The gravitational attraction of a right rectangular prism, *Geophysics*, 31, 263-371.
- Nagy, D., 1973. A chart for the computation of the gravitational attraction of a right rectangular prism, *PAGEOPH*, 102, 5-14.
- Norabuena, E.O., Dixon, T.H., Stein, S. & Harrison, C.G.A., 1999. Decelerating Nazca--South America and Nazca--Pacific Plate motions, *Geophys. Res. Lett.*, 26, 3405-3408.
- Norvick, M.S., 2004. Tectonic and stratigraphic history of the Perth Basin, pp. 30 *Geoscience Australia*
- Oncken, O., Chong, G., Franz, G., Giese, P., Götze, H.-J., Ramos, V., Strecker, M. & Wigger, P., 2006. *The Andes – Active Subduction Orogeny*, edn, Vol. 1, pp. Pages, Springer-Verlag, Berlin Heidelberg New York.
- Pail, R., Goiginger, H., Schuh, W.D., Höck, E., Brockmann, J.M., Fecher, T., Gruber, T., Mayer-Gürr, T., Kusche, J., Jäggi, A. & Rieser, D., 2010. Combined satellite gravity field model GOCO01S derived from GOCE and GRACE, *Geophysical Research Letters*, 37, L20314.
- Parker, R.L., 1995. Improved Fourier terrain correction; Part I, *Geophysics*, 60, 1007-1017.
- Parker, R.L., 1996. Improved Fourier terrain correction; Part II, *Geophysics*, 61, 365-372.
- Parsiegla, N., Stankiewicz, J., Gohl, K., Ryberg, T. & Uenzelmann-Neben, G., 2009. Southern African continental margin: Dynamic processes of a transform margin, *Geochemistry, Geophysics, Geosystems*, 10, Q03007.
- Pavlis, N.K., Factor, J.K. & Holmes, S.A., 2007. Terrain-related gravimetric quantities computed for the next EGM. in *Proceedings of the 1st International Symposium of the International Gravity Field Service (IGFS), Istanbul 2006, Harita Dergisi, Special Issue*, pp. 318-323, Istanbul, Turkey.
- Pavlis, N.K., Holmes, S.A., Kenyon, S.C. & Factor, J.K., 2008. An Earth Gravitational Model to Degree 2160: EGM 2008.
- Pedersen, L.B. & Rasmussen, T.M., 1990. The gradient tensor of potential field anomalies: Some implications on data collection and data processing of maps, *Geophysics*, 55, 1558-1566.
- Petkovic, P., Fitzgerald, D., Brett, J., Morse, M. & Buchanan, C., 2001. Potential Field and Bathymetry Grids of Australia's Margins, *ASEG Extended Abstracts*, 2001, 4pp.
- Prezzi, C.B., Götze, H.-J. & Schmidt, S., 2009. 3D density model of the Central Andes, *Physics of the Earth and Planetary Interiors*, 177, 217 - 234.

References

- Quaife, R., Rosser, J. & Pagnozzi, S., 1994. The structural architecture and stratigraphy of the offshore northern Perth Basin. *in The Sedimentary Basins of Western Australia, Proceedings of the Petroleum Exploration Society of Australia Symposium*, pp. 811–822, eds Purcell, P. G. & Purcell, R. R., Perth.
- Ramos, V.A. & Aleman, A., 2000. Tectonic evolution of the Andes, pp. 635-685.
- Ranero, C.R., Phipps Morgan, J., McIntosh, K. & Reichert, C., 2003. Bending-related faulting and mantle serpentinization at the Middle America trench, *Nature*, 425, 367-373.
- Ranero, C.R. & von Huene, R., 2000. Subduction erosion along the Middle America convergent margin, *Nature*, 404, 748-752.
- Reichert, C. & Schreckenberger, B., 2002. Cruise report SO-161 leg 2 & 3, SPOC (Subduction Processes Off Chile)BGR Hannover.
- Reigber, C., Schmidt, R., Flechtner, F., König, R., Meyer, U., Neumayer, K.-H., Schwintzer, P. & Zhu, S.Y., 2005. An Earth gravity field model complete to degree and order 150 from GRACE: EIGEN-GRACE02S, *Journal of Geodynamics*, 39, 1 - 10.
- Reutter, K.H. & Götze, H.-J., 1994. Comments on the geological and geophysical maps. *in Tectonics of the Southern Central Andes*, pp. 329-333, eds. Reutter, Scheuber & Wigger. Springer, Heidelberg.
- Reynisson, R.F., Ebbing, J., Lundin, E. & Osmundsen, P.T., 2010. Properties and distribution of lower crustal bodies on the mid-Norwegian margin, *Geological Society, London, Petroleum Geology Conference Series*, 7, 843–854.
- Rollet, N., Pfahl, M., Jones, A., Kennard, J.M., Nicholson, C., Grosjean, E., Mantle, D., Jorgensen, D.C., Bernardel, G., Kempton, R., Langhi, L., Zhang, Y., Hall, L., Hackney, R., Johnston, S., Robertson, D., Petkovic, P. & Lech, M., in press. Northern extension of active petroleum systems in the offshore Perth Basin – an integrated stratigraphic, geochemical, geomechanical and seepage study. *in Proceedings, West Australian Basins Symposium 18–21 August 2013*, eds Keep, M. & Moss, S. Petroleum Exploration Society of Australia.
- Sallarès, V., Charvis, P., Flueh, E.R. & Bialas, J., 2003. Seismic structure of Cocos and Malpelo Volcanic Ridges and implications for hot spot-ridge interaction, *J. Geophys. Res.*, 108, 2564.
- Sallarès, V., Danobeitia, J.J. & Flueh, E.R., 2001. Lithospheric structure of the Costa Rican Isthmus: Effects of subduction zone magmatism on an oceanic plateau, *J. Geophys. Res.*, 106, 621-643.
- Santos, D.F., Silva, J.B.C., Barbosa, V.C.F. & Braga, L.F.S., 2012. Deep-pass --- An aeromagnetic data filter to enhance deep features in marginal basins, *Geophysics*, 77, J15-J22.

- Scheuber, E., Bogdanic, T., Jensen, A. & Reutter, K., 1994. Tectonic development of the north Chilean Andes in relation to plate convergence and magmatism since the Jurassic. *in {Tectonics of the southern central Andes}*, pp. 7-22, eds. Reutter, K., Scheuber, E. & Wigger, P. Springer, Berlin Heidelberg New York.
- Schmidt, S. & Götze, H.-J., 2006. *Bouguer and isostatic maps of the Central Andes*, edn, Vol. 15, pp. Pages, Springer-Verlag, Berlin/Heidelberg/New York.
- Schmidt, S., Götze, H.-J., Fichler, C. & Alvers, M., 2010. IGMAS+ a new 3D Gravity, FTG and Magnetic Modeling Software, pp. 57-63.
- Schmidt, S., Götze, H.J., Fichler, C., Ebbing, J. & Alvers, M.R., 2007. 3D Gravity, FTG and Magnetic Modeling: the new IGMAS+ Software. *in EGM 2007 International Workshop, Innovation in EM, Grav and Mag Methods:a new Perspective for Exploration*, Capri, Italy.
- Schmidt, S., Plonka, C., Götze, H.-J. & Lahmeyer, B., 2011. Hybrid modelling of gravity, gravity gradients and magnetic fields, *Geophysical Prospecting*, 59, 1046–1051.
- Schmitz, M., Lessel, K., Giese, P., Wigger, P., Araneda, M., Bribach, J., Graeber, F., Grunewald, S., Haberland, C., Lüth, S., Röwer, P., Ryberg, T. & Schulze, A., 1999. The crustal structure beneath the Central Andean forearc and magmatic arc as derived from seismic studies -- the PISCO 94 experiment in northern Chile (21°-23°S), *Journal of South American Earth Sciences*, 12, 237 - 260.
- Sclater, J.G. & Christie, P.A.F., 1980. Continental stretching: an explanation of the post-Mid-Cretaceous subsidence of the central North Sea Basin, *Journal of Geophysical Research*, 85, 3711–3739.
- Sick, C., 2006. Structural investigations off Chile: Kirchhoff Prestack Depth Migration versus Fresnel Volume Migration, Department of Earth Sciences, Freie Universität Berlin.
- Sideris, M.G., 1984. *Computation of Gravimetric Terrain Corrections Using Fast Fourier Transform Techniques [microform]*, edn, Vol., pp. Pages, Thesis (M.Sc.)--University of Calgary.
- Smallgood, J.R., Towns, M.J. & White, R.S., 2001. The structure of the Faeroe–Shetland Trough from integrated deep seismic and potential field modelling, *Journal of the Geological Society*, 158, 409–412.
- Smith, B. & Sandwell, D., 2003. Accuracy and resolution of Shuttle Radar Topography Mission data., *Geophysical Research Letters*, 30, 1467.
- Sobiesiak, M., Meyer, U., Schmidt, S., Gö, t., H.-J. & Krawczyk, C.M., 2007. Asperity generating upper crustal sources revealed by b value and isostatic residual anomaly grids in the area of Antofagasta, Chile, *J. Geophys. Res.*, 112, B12308.

References

- Sobolev, S., Babeyko, A., Koulakov, I. & Oncken, O., 2006. 25 Mechanism of the Andean Orogeny: Insight from Numerical Modeling. *in The Andes*, pp. 513-535, eds. Oncken, O., Chong, G., Franz, G., Giese, P., Götze, H.-J., Ramos, V., Strecker, M. & Wigger, P. Springer Berlin Heidelberg.
- Song, T.-R.A. & Simons, M., 2003. "Large Trench-Parallel Gravity Variations Predict Seismogenic Behavior in Subduction Zones", *Science*, 301, 630-633.
- Sweetman, S., 1997. The integration of seismic interpretations with gravity and magnetic 2-D modeling — An example from the offshore Faroes area, *The Leading Edge*, 16, 15–20.
- Szwillus, W., Köther, N. & Götze, H.-J., 2012. Calculation of gravitational terrain effects using robust, adaptive and exact algorithms. *in AGU Fall meeting 2012*, San Francisco.
- Talwani, M., 1998. Errors in the total Bouguer reduction, *GEOPHYSICS*, 63, 1125-1130.
- Tašárová, Z., 2004. Gravity Data Analysis and Interdisciplinary 3D Modelling of a Convergent Plate Margin (Chile, 36°–42°S), Ph.D., Freie Universität Berlin.
- Tassara, A., 2010. Control of forearc density structure on megathrust shear strength along the Chilean subduction zone, *Tectonophysics*, 495, 34-47.
- Tassara, A., Götze, H.-J., Schmidt, S. & Hackney, R., 2006. Three-dimensional density model of the Nazca plate and the Andean continental margin, *J. Geophys. Res.*, 111, B09404.
- Tracey, R. & Nakamura, A., 2010. Complete Bouguer anomalies for the Australian National Gravity Database, *ASEG Extended Abstracts*, 2010, 3pp.
- Uieda, L., N. Ussami, and C. F. Braitenberg, 2010. Computation of the gravity gradient tensor due to topographic masses using tesseroids. *in Eos Trans. AGU Meet. Am. Suppl.*,.
- Welford, J.K., Shannon, P.M., O'Reilly, B.M. & Hall, J., 2010. Lithospheric density variations and Moho structure of the Irish Atlantic continental margin from constrained 3-D gravity inversion, *Geophysical Journal International*, 183, 79–95.
- Wells, R.E., Blakely, R.J., Sugiyama, Y., Scholl, D.W. & Dinterman, P.A., 2003. Basin-centered asperities in great subduction zone earthquakes: A link between slip, subsidence, and subduction erosion?, *J. Geophys. Res.*, 108, 30 pp.
- Wessel, P. & Smith, W.H.F., 1991. Free software helps map and display data, *EOS, Transactions, American Geophysical Union*, 72, 441.
- Wessel, P. & Smith, W.H.F., 1998. New, improved version of generic mapping tools released, *Eos, Transactions American Geophysical Union*, 79, 579-579.

Whiteway, T.G., 2009. Australian Bathymetry and Topography Grid, June 2009, pp. 46 Geoscience Australia.

Danksagung

Diese Arbeit entstand im Rahmen des SPP 1257 "Massentransport und Massenverteilung des Systems Erde", in den Teilprojekten "NOGAPSGRAV" und "IMOSAGA", gefördert durch die Deutsche Forschungsgemeinschaft (DFG).

Mein erster Dank richtet sich an meinen Betreuer Herrn Prof. Dr. Götze.

Er hat mir während meiner gesamten Arbeit konstruktiv mit Rat und Tat zur Seite gestanden. Insbesondere danke ich ihm für die ganz besondere Unterstützung, um meinen Forschungsaufenthalt in Australien zu realisieren. Die vielen Jahre als Hiwi, auf Exkursionen (Ellerbek und Meran), die Diplomandenzeit und die gemeinsame Durchführung der SPP-Projekte werden mir immer in Erinnerung bleiben.

Herrn Prof. Dr. Rabbel danke ich für die Anfertigung des Korreferats.

Desweiteren möchte ich mich gerne bei den folgenden Personen und Gruppen bedanken:

- Dr. Desmond FitzGerald, der mit seiner Firma Intrepid Geophysics meinen Australienaufenthalt ermöglicht hat und mir dabei finanziell, inhaltlich und freundschaftlich zur Verfügung stand. Auch Danke für das Fahrrad!
- Dr. Ron Hackney, durch den überhaupt erst eine Zusammenarbeit mit Geoscience Australia zustande kam. Vielen Dank für die herzliche und freundschaftliche Aufnahme (auch an Alli und die Kinder), die tollen inhaltlichen Diskussionen und die fruchtbare Arbeit am "North Perth Basin".
- Stephen Johnston für die Diskussionen über Seismik, Magnetik und Triatlons.
- Auch noch einen Dank ans ganze Intrepid-Team, insbesondere Dominik für die Kletterabende.
- Wolfgang Szwillus für die tolle und fruchtbare Zusammenarbeit im "kleinen Kreis", die (langen) Diskussionen über topographische Korrekturen und natürlich die Abbildung in Kapitel 3.
- Dr. Sabine Schmidt für Ratschläge zu verschiedensten Themen, insbesondere Interpolation, IGMAS+ und analytischer Geometrie.
- Unserer gesamten AG "Geophysik und Geoinformation" für die Diskussionen zu allen möglichen Themen und den Sommerabenden bei Hajo.

- Ben und Oskar danke ich für die gemeinsame Arbeit und Hilfe im Projekt und dem Durchstehen von Begutachtungsrunden.
- Zuzi danke ich auch für die geodätischen Diskussionen und den Beistand in den schwierigen Phasen der Arbeit.

Außerdem danke ich ganz besonders meiner Freundin Thuri, die mich während meiner gesamten Dissertation begleitet und alle Anstrengungen mit mir durchgestanden hat. Vielen Dank für deine Unterstützung und deinen Bunsenbrenner! Du bist mein Halt.

Erklärung

Hiermit versichere ich, dass die vorliegende Arbeit von mir unter Anleitung meiner Betreuer und nur mit den angegebenen Hilfsmitteln verfasst worden ist. Diese Arbeit hat weder in gleicher noch in ähnlicher Form einer anderen oder dieser Stelle im Rahmen eines Prüfungsverfahrens vorgelegen. Hiermit versichere ich, dass die Arbeit unter Einhaltung der Regeln guter wissenschaftlicher Praxis der Deutschen Forschungsgemeinschaft entstanden ist.

Datum, Ort, _____

(Nils Holzrichter)

Curriculum Vitae

Nils Holzrichter

Geburtsname: Köther
Geburtsdatum: 11.05.1984
Geburtsort: Heide (Holstein),
Staatsangehörigkeit: deutsch

Schulbildung

1995-2004 **Besuch des Nordsee-Gymnasiums Büsum**

05/2004 **Allgemeine Hochschulreife**

wissenschaftlicher Werdegang

ab 10/2004 Diplomstudium der Geophysik, Christian-Albrechts-Universität Kiel
Nebenfächer: Ingenieurgeologie, Astrophysik

03/2007 Vordiplom in Geophysik

10/2009 Diplomarbeit:
Joint 3D gravity and magnetic modelling of the Taoudeni Basin
(Preisträger VdFuF der Geophysik: Herausragende Diplomarbeiten 2009)

ab 11/2009 Promotionsstudium am Institut für Geowissenschaften, Abteilung Geophysik,
Christian-Albrechts Universität Kiel

03/2011 Forschungsaufenthalt in Melbourne, Australien bei Intrepid Geophysics und
08/2011 Geoscience Australia, Canberra.

Copyright acknowledgement

Chapter 2 was published in Journal of Geodynamics, Volumes 59-60; Authors: N. Köther, H.-J. Götze, B.D. Gutknecht, T. Jahr, G. Jentzsch, O.H. Lücke, R. Mahatsente, R. Sharma, S. Zeumann, Title: "The seismically active Andean and Central American margins: Can satellite gravity map lithospheric structures?", Pages 207-218, Copyright Elsevier 2012.

The original article can be accessed at:

<http://www.sciencedirect.com/science/article/pii/S0264370711001256>.

<http://dx.doi.org/10.1016/j.jog.2011.11.004>.

Chapter 4 (except for paragraph 4.7.) is published in the Geophysical Journal International, Wiley.

Citation:

Holzrichter, N., Hackney, R.I., Johnston, S., 2013. Crustal structure of the northern Perth Basin, southwest margin of Australia: insights from three-dimensional density models, Geophysical Journal International, doi: 10.1093/gji/ggt347.

This article was published by Oxford University Press, Geophysical Journal International. This is an Open Access article distributed under the terms of the Creative Commons Attribution 3.0 Australia License (<http://creativecommons.org/licenses/by/3.0/au/>), which permits unrestricted reuse, distribution, and reproduction in any medium, provided the original work is properly cited.



© Commonwealth of Australia (Geoscience Australia) 2013.